Energy efficient strategy for designing metal–organic frameworks based bifunctional electrocatalysts and high performing rechargeable zinc-air batteries

Juntao Li

A thesis presented for the degree of

Doctor of Philosophy

Supervised by

Professor Ivan P. Parkin

Professor Zhengxiao Guo

Department of Chemistry

Mathematical and Physical Sciences Faculty

University College London

March 2021

Declaration

I, Juntao Li, confirm that the work completed in this thesis is my own. The information derived from other sources (publications, websites and database) has been acknowledged in the thesis. All the figures from publications (including my own work) have obtained their copyright permission from the journal publisher.

Abstract

To fulfil the increasing demands for efficient and clean energy storage and conversion technologies, including fuel cells, water electrolysis and metal-air batteries are of great importance. These energy technologies are based on various electrochemical catalysis processes, such as hydrogen evolution reaction (HER), hydrogen oxidation reaction (HOR), oxygen reduction reaction (ORR) and oxygen evolution reaction (OER). Huge efforts have been dedicated for designing the efficient electrocatalysts. In spite of the benchmark materials from the precious metal compounds (Pt/C for ORR, IrO_2 for OER), the most common routine for synthesising bifunctional catalysts is carbonising organic, inorganic and polymeric materials at high temperature and then post-synthesis chemical modification. However, production of such materials via pyrolysis poses significant challenges for controlling the composition, functionality, heterogeneity, porosity and nanophase (i.e., aggregation of metal centres) properties, as well as for mass production. Hence, in this thesis work a straightforward and energy efficient routes to produce highly active electrocatalysts are disclosed and discussed.

In the first work, a new strategy to extract the electrocatalytic activity from as-received zeolitic imidazolate frameworks (ZIFs) is developed without the need for routinely performed post-synthesis chemical modification. This represents a step forward in experimental design and yields materials with near best in class performance. Metal-organic framework (MOF)-/ZIF-derivatives nanostructure via post-synthesis thermolysis have opened up phenomenal interest for electrocatalysis applications. Contrary to this, the first work discovers the interesting electrocatalytic activity of as-synthesized bimetallic ZIFs(Co/Zn) directly without carbonisation and establishes OER activity trend with the substitution of cobalt metal centres for zinc. An

enhanced activity and trend with respect to particle size of ZIF-67 is achieved, where identical structural parameters are maintained. Furthermore, a significantly enhanced OER activity, >50%, in ZIF-67/carbon black or ZIF-67/carbon paper conducting supports is obtained. A long term durability of ZIF-67/carbon paper during 24 hours continuous operation shows exceptionally improved activity and stability.

In the second work, based on the comprehensive understanding for the readily synthesized MOF structure, a new composite of cobalt based ZIF and platinum carbon black (Pt/CB) in 1:1 mass ratio (ZIF-67@Pt/CB) is designed via facile solution mixing at room temperature, and without carrying out high temperature carbonization and/or calcination. This hybrid compound shows a promising bifunctional electrocatalytic activity for oxygen (OER and ORR), the key charge and discharge mechanisms in a battery. The as produced ZIF-67@Pt/CB exhibits a significantly enhanced catalytic stability compared to Pt/CB and delivers a high performance with excellent long term stability. Overall, the readily available ZIF-67 can be easily turned into a high performing zinc-air battery cathode material. This thesis work shows commercial feasibility of zinc-air batteries as ZIFs can be reproducibly synthesized in mass scale and applied as produced.

The third work demonstrates a replicate synthetic route to highly active electrocatalyst from ZIF starting materials without the need for carbonisation or other post-synthesis modification. Inspired by the second work, in that the post-electrochemical studies reveal an electrochemically driven in-situ development of OER active cobalt-(oxy)hydroxide nanophase. Therefore, as-synthesized ZIF-67 is being in-situ electrochemically activated on the air cathode directly by coating thin film on the carbon paper gas diffusion layer current collector. The in-situ electrochemical activation has been carried out by performing charge-discharge cycling tests under various applied current densities as well as cyclic duration. In addition to this, ZIF-67 samples with various crystallite

sizes (particle size of polyhedrons between 50 nm and 2000 nm) have also been studied. These electrochemical and physical conditions help to understand the true activation mechanism of the ZIF-67 and further to fine tune the structure-activation-property relationships. The electrocatalyst generated via in-situ electrochemical activation under optimized particle size and activation conditions delivers a remarkable performance in the zinc-air batteries, outperforming the most of the carbon based as well as commercial benchmark standard Pt/CB+IrO2/CB bifunctional catalysts in the literature. The in-situ activated ZIF-67 air cathode catalyst based zinc-air batteries repeatedly deliver outstanding long cycling stability for over 1000 h (6600cycles) and maintaining high power density of ~180 mW cm^{-2}, whereas the reference Pt/Ir-based catalyst air cathode based cell dies after 50 h (200 cycles) with a rapid degradation in the power density.

Therefore, given the urgent and rapidly growing global interest in energy conversion and storage materials, and the key material and conceptual advances presented, this thesis work will guide for further advancements and enable identification of electrocatalysts from as-produced ZIFs alone, without resorting to energy-intensive post-processing methods.

Impact statement

This PhD project focused on developing facile strategies fabricating highly efficient catalysts based on metal organic framework structure. The impact and highlights from this thesis are:

- Identify electrocatalytic activity of as-synthesized ZIF-67(Co) directly without carbonisation and its analogue ZIF-8(Zn), and bimetallic ZIFs(Co/Zn).
- Find exciting OER activity trend with the substitution of cobalt metal centers for zinc.
- Study ZIF-67 polyhedrons size dependent activity, then demonstrate a significantly enhanced OER activity, >50%, in ZIF-67/carbon black composite (ZIF/CB; a simple hand milled physical mixture). This composition exhibits a low-overpotential of ~320 mV at 10 mA cm^{-2} in alkaline electrolyte.
- Moreover, achieved the bifunctional activities, with a small overpotential of 0.87 V, for both OER and ORR from the simple physical mixture of ZIF-67 and commercial Pt/C (ZIF-67@Pt/C(50wt%)).
- Note, ZIF-67 based catalysts exhibit stable OER and ORR activities for several hours. Notably, ZIF-67@Pt/C composite shows enhanced stability for ORR - over 20 h of operation the sample retains 85% of its initial activity compared to ~50% for Pt/C reference. The ZIF-67@Pt/C still maintains ~65% of its ORR performance during a 85 h test.
- Apply ZIF-67@Pt/CB as a bifunctional cathode electrode, the rechargeable zinc-air battery (ZAB) device readily delivers impressive open circuit voltage of 1.42 V, and a large current density of 100 mA cm^{-2} at a voltage of 1.0 V and maximum power density of >150 mW cm^{-2}. These Zinc air batteries are operated at $\leq$ 0.8 V and remain stable in the extended cyclic tests for a measured period of 50 h (for 300 cycles).
- The ZIF-67 derived cobalt-(oxy)hydroxide nanophase structure could deliver a power density of 180 mW cm^{-2} which is nearly 4.5 times enlargement compared with the pristine ZIF-67 and superb long cycling stability for over 1000 h when applying in zinc air batteries.
- In situ development of cobalt-(oxy)hydroxide nanophase from the ZIF-67 is investigated via many characterization methods to contribute to the significantly improved battery performance.

In summary, the pioneering work reported here shows commercial feasibility of zinc-air batteries as MOF-cathode materials can be reproducibly synthesized in mass scale and applied as produced.

Acknowledgements

First and foremost, I would like to express my great gratitude to my supervisors, Prof. Ivan P. Parkin and Prof. Zhengxiao Guo for proving me the opportunity to pursue my PhD in UCL. Without their continued support and advice, I could not have the achievement in research.

Then, I would like to specially thank Dr. Srinivas Gadipelli, who skilled me the experimental technics and helped me to build up my research project, it was an honor to work and study under his guidance.

Next, I would like to thank all my collaborators for their support on my research, including, Dr. Guanjie He, Dr Zhuojun Li, Prof. Dan Brett and Prof. Paul Shearing. Thanks to all the group members from Prof. Parkin's and Prof. Guo's group, especially Dr. Jian Guo, Dr. Zhuangnan Li, Dr. Yuchen Yang, Dr. Tingting Zhao, Dr. Yue Lu, Dr. Jianwei Li, Dr. Xiaoyu Han, Dr. Yudao Qin, Mr. Juhun Shin, Mr. Bowen Guan, Mr. Zhiyong Pan, Miss. Yuting Yao, with all of you I had a delightful and meaningful time here. Also thank Dr. Steve Firth, Mr. Martin Vickers, and Dr Sanjayan Sathasivam for providing me the facility training and technical help.

Finally, I would like to thank my parents and Miss Zhu Meng for their infinite love and continuous support during my PhD life.

Table of contents

List of Figures

Chapter 1. Literature review and background

Chapter 3. Synthesis and optimisation of zeolitic imidazolate frameworks for oxygen evolution reaction

Chapter 4. Direct utilisation of zeolitic imidazolate framework – ZIF-67 as bifunctional oxygen electrocatalyst for zinc-air batteries

Chapter 5. An in-situ electrochemically generated highly active ZIF-67 based cathode catalyst for zinc-air batteries with remarkable performance

List of Tables

Chapter 1. Literature review and background

Chapter 3. Synthesis and optimisation of zeolitic imidazolate frameworks for oxygen evolution reaction

Chapter 4. Direct utilisation of zeolitic imidazolate framework – ZIF-67 as bifunctional oxygen electrocatalyst for zinc-air batteries

Abbreviation

BET	Brunauer–Emmett–Teller
BJH	Barrett-Joyner-Halenda
CNT	Carbon nanotube
CP	Carbon paper
CV	Cyclic voltammetry
EDS	Energy dispersive spectroscopy
EIS	Electrochemical impedance spectroscopy
EZIF-67	electrochemically activated ZIF-67
FTIR	Fourier transform infrared spectroscopy
GCE	Glassy carbon electrode
GO	Graphene-oxide
HER	Hydrogen evolution reaction
HOR	Hydrogen oxidation reaction
LED	light-emitting diode
LSV	Linear sweep voltammograms
MOF	Metal organic framework
ORR	Oxygen reduction reaction
OER	Oxygen evolution reaction
PTFE	Polytetrafluoroethylene
PSD	Pore size distribution
PVA	Polyvinyl alcohol
Pt/CB	Platinum on carbon 20% weight loading
RDE	Rotating disk electrode
SEM	Canning electron microscope
TEM	Transmission electron microscope
RDE	Rotating disk electrode
TGA	Thermogravimetric analysis
XPS	X-ray photoelectron spectroscopy
XRD	X-ray diffraction

ZABs	Zinc air batteries
ZIFs	Zeolitic imidazolate frameworks

Chapter 1. Literature review and background

1.1 Introduction

The pursuit of advanced electrocatalyst for clean energy economy never fails to fascinate the researchers. The multifarious electrochemical energy storage devices with different size and time scales have been intensely investigated and applied in our daily life, including smart phone, electric vehicles and portable electronics.[1,2] However, the electricity generation and transportation by using fossil fuels give rises to a series of issues, particularly, the global warming and environmental pollution. Thus, increasing attention has been paid to develop sustainable and economical energy storage devices. Despite the significant success on commercialization, current lithium-ion batteries suffered from the inadequate energy density (generally < 300 Wh kg^{-1}), safety, charging time, temperature window and high cost (~ $ 150 kW^{-1} h^{-1}).[3] Therefore, great efforts have been dedicated for developing the alternate batteries with high safety, performance/energy density and with reduced cost, for instance, aqueous electrolyte based metal-air battery systems.

Metal-air batteries with their high energy density and abundant resources with low cost have triggered astonishing research interest across the globe.[4] A brief timeline of research progress in metal-air batteries is schematically presented in Figure 1.1. Several metals have been investigated such as Li, Na and K as mono-valent charge carriers often studied in non-aqueous environment and for relatively inactive metals such as Zn, Ca, Al, Fe and Mg are often evaluated in alkaline electrolyte.[4–8] However, Li, Na and K are all sensitive to the air and water environment and react explosively thus strictly hindering alkaline-metal-air batteries development.[9] Mg and Al air batteries have good stability in air and aqueous electrolyte, but are limited by the self-discharge phenomenal due to their lower reduction potentials of E^0 = -1.66 V, -2.38 V than water (E^0= -0.83 V), leading to a severe battery capacity loss.[10]

The zinc-air batteries are one of the most promising next commercial and feasible energy storage systems, due to the high theorical energy densities of 1370 and 1086 Wh kg^{-1}, respectively for

excluding and including the mass of oxygen.[11] Compared to other active metals, metallic zinc has good tolerance to oxygen and can directly use as anodes in aqueous electrolyte. Meanwhile the theoretical energy density is about 5 folds higher than the current lithium-ion battery technology.

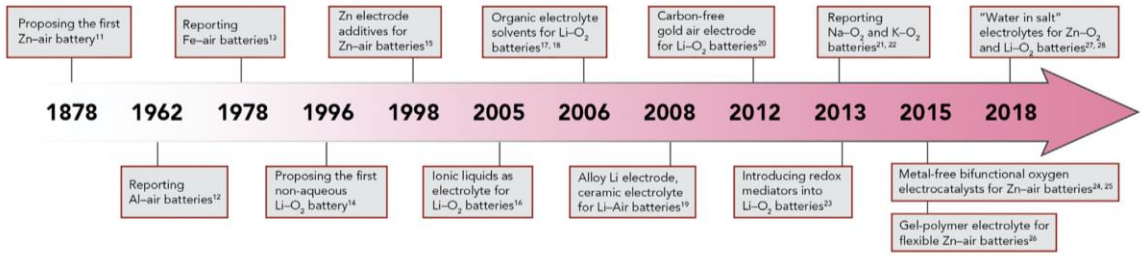

Figure 1.1. A brief timeline of research progress in metal-air batteries.[12] (Copyright Elsevier Inc. Reproduced with permission)

1.2 Zinc-air batteries

The first zinc-air battery invention can be dated back to 1878, since then huge progress has been made in the field of metal-air batteries (Figure 1.1).[12] The high theoretical specific energy density 1084 Wh kg^{-1} and good cell voltage 1.65 V owned by rechargeable zinc-air battery considered as the promising energy storage/conversion medium compared to the traditional lithium-ion battery. There are many advantages such as the rich amount of zinc at a global scale, high safety and low cost (<100 kW^{-1} h^{-1}) compared to other energy storage technologies. One of the major factors that impedes the development of the rechargeable zinc-air batteries is the reaction based on the air electrode. During charge and discharge process the cathode material experience oxygen evolution and oxygen reduction reactions, respectively, often these are associated with sluggish kinetics and active catalysts needed to drive reactions.

Normally, zinc-air batteries contain four components as depicted in Figure 1.2. The catalyst on the air electrode (cathode), zinc electrode (anode), electrolyte and separator. As the reactant oxygen is from the air, the air electrode usually consisted of an electrocatalyst layer to reduce the charge

overpotential and a gas diffusion layer to prevent leaking and enhance the diffusion between the catalyst surface and ambient air. Generally, the zinc electrode suffers from oxidation during discharge that leads to the $Zn(OH)_4^{2-}$ formation, until they are saturated in the electrolyte, following this, the zincate ions then transform to zinc oxide as the final product.[13] Meanwhile, on the air cathode, oxygen molecules accept the electrons and converted to OH^- through the ORR path. The OH- would react with zinc and generate $Zn(OH)_4^{2-}$ on the anode and then, the excess zincate converted to zinc oxide as the final oxide formed on the zinc anode.

The reaction pathways in real zinc-air batteries cell are described below (Equations 1.1-1.4).

Zinc electrode:

$$Zn + 4OH^- \rightarrow Zn(OH)_4^{2-} + 2e^- \quad \text{(Equation 1.1)}$$

$$Zn(OH)_4^{2-} \rightarrow ZnO + H_2O + 2e^- \quad \text{(Equation 1.2)}$$

Air electrode:

$$O_2 + 2H_2O + 4e^- \rightarrow 4OH^- \quad \text{(Equation 1.3)}$$

Overall reaction:

$$2Zn + O_2 \rightarrow 2ZnO \quad \text{(Equation 1.4)}$$

Concentrated KOH solution is most frequently employed in zinc air batteries due to its high ionic conductivity and low viscosity compared with other alkaline electrolytes including NaOH and LiOH.[14] 6M KOH solution with 0.2 M zinc acetate or zinc chloride as the electrolyte has been reported as the most commonly used and for optimized performance. The additional zinc ions added in the KOH solution can enhance the reversibility of the zinc electrode and overall durability of the battery.[15] In some circumstances, for example in a large liquid cells, the separator is not necessary as it is used to separate two different electrolytes or prevent short-circuit situation in coin cells or solid state cells. [12]

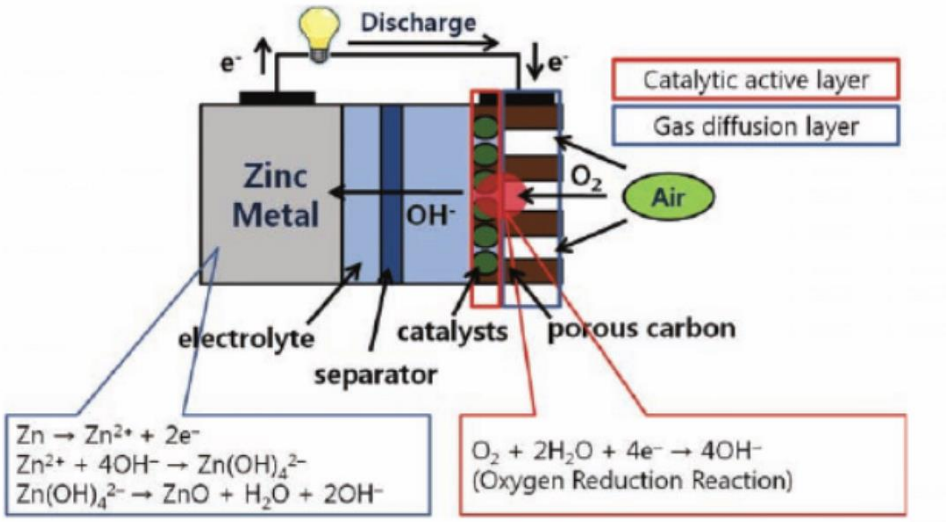

Figure 1.2. Schematic images of a working zinc air battery.[16] (Copyright WILEY-VCH Verlag GmbH & Co. Reproduced with permission)

1.2.1 Evaluation Method and Parameters for zinc-air batteries

To evaluate the performance of zinc-air batteries, several factors need to be addressed. First, the polarization curve, which is a useful tool to show/understand how much the current density can be achieved at a specific discharge voltage. Next, the peak power density, which is based on the calculation on the discharge polarization curve. The power density (P in mW cm^{-2}) is estimated based on the equation: $P = U \times J$, where U is the battery voltages (V), and J is the current density of the discharge polarisation (mA cm^{-2}).

Second, as the oxygen is from air, which is nearly infinite, the practical capacity depends on the consumed zinc during the discharge process. Another critical feature to judge the performance of battery is round-up efficiency and cycling life. Round up efficiency is calculated by dividing the discharge by charge voltage at a constant current density in the cycling process, which reflect the energy utilizing efficiency of a zinc-air battery.

Cycling life relies on the stability of charge and discharge voltage levels. A high voltage during charging will deteriorate the electrode, which is primarily due to the oxidation degradation of the catalyst/support with the reaction from highly reactive oxygen species generated from oxidation of electrolyte. Another factor that impedes the zinc-air batteries is the dendrite formation on the zinc anode during the long-term cycling. Thus, it is desirable to design highly active bifunctional electrocatalyst to lower the overpotentials during the charge-discharge cycling.

1.2.2 Reaction mechanism for ORR and OER

Typically, the cathode reaction of zinc-air batteries involves oxygen reduction and evolution reaction (ORR and OER). The reaction normally occurs in alkaline solution. The sluggish kinetics of ORR and OER limited the development of rechargeable zinc-air batteries due to the low energy conversion efficiency and inferior cycling life. Moreover, the battery power density is decided by the ORR performance of the electrocatalysts. While the OER performance also have a great impact on the energy efficiency and cycling life. Poor OER activity means it requires a high voltage for charging the battery. This ultimately results in side reactions, such as oxidation of the carbon electrode (carbon corrosion), which will -have a detrimental effect on the ORR activity.[17–21] Thus, upon repeated cycling, the reactions will become more sluggish due to the increased resistance and dissolution of oxidized carbon in the air electrode. For these reasons, the highly dual-active OER and ORR electrocatalyst could operate at a smaller voltage window is needed during the cyclic durability test.

ORR mechanism

In general, oxygen reduction reaction occurs on the oxygen adsorption mode and dissociation barrier on the surface of the catalyst.[22] There are two pathways for ORR in aqueous solution: four-electron pathway from O_2 to H_2O and two-electron pathway from O_2 to H_2O_2.[23] Equations 1.5-1.8 describe the ORR pathway in acidic and alkaline electrolytes. The difference between these two pathways is whether O_2 molecule dissociated before reduction.[24] Next, because the ORR

current depends on the rate of the reaction and the electrochemical barriers, it is necessary to discuss the kinetics of the ORR.

In acid aqueous electrolyte

$O_2 + 4H^+ + 4e^- \rightarrow 2H_2O$ $E^0 = 1.229$ V (Equation 1.5)

$O_2 + 2H^+ + 2e^- \rightarrow H_2O_2$ $E^0 = 0.67$ V (Equation 1.6)

In alkaline aqueous systems

$O_2 + 2H_2O + 4e^- \rightarrow 4OH^-$ $E^0 = 0.401$ V (Equation 1.7)

$O_2 + H_2O + 2e^- \rightarrow HO_2^- + OH^-$ $E^0 = -0.065$ V (Equation 1.8)

OER mechanism

The oxygen evolution reaction occurs at the cathode also involves four electron pathway and requires higher energy to overcome the energy barrier. As the half reaction of the water splitting, OER means H_2O or OH^- losing electrons to generate O_2. Moreover, the overpotential of OER is important in practical applications such as zinc-air batteries.[25] High overpotential result in lower round-trip efficiency and accelerated the decomposition of the catalysts. Formulas depict the OER process in acidic and alkaline electrolyte described as below:

In acid aqueous electrolyte

$2H_2O \rightarrow O_2\uparrow + 4H^+ + 4e^-$ $E_0 = 1.229$ V (Equation 1.9)

In alkaline aqueous systems

$4OH^- \rightarrow O_2\uparrow + 2H_2O + 4e-$ $E_0 = 0.401$ V (Equation 1.10)

1.2.3 Evaluation Method and Parameters for Bifunctional Oxygen Electrocatalysis

Linear sweep voltammetry (LSV) curves

Normally, in the lab based tests, a rotating disk electrode (RDE) system is used as a useful tool to discover the activity and reaction pathways of oxygen reduction and evolution reactions. The conventional three electrode setup contains counter electrode, reference electrode and with working electrode loaded with catalysts layer as show in the Figure 1.3. In general, counter electrode is carbon rod or platinum, and reference electrode is Ag/AgCl or Hg/HgO depending on the region, in which whether HgO listed as dangerous chemicals. Catalyst powder is often prepared in a water/ethanol solution with Nafion as the binder. The content of the binder is expected to be as low as possible, so as to get the best performance. Because O_2 has low solubility in aqueous solutions, the rotating electrode can increase the mass transfer rate during the ORR. During OER measurements, the rotating electrode also helps to reduce the O_2 produced on the surface of the glassy carbon electrode.

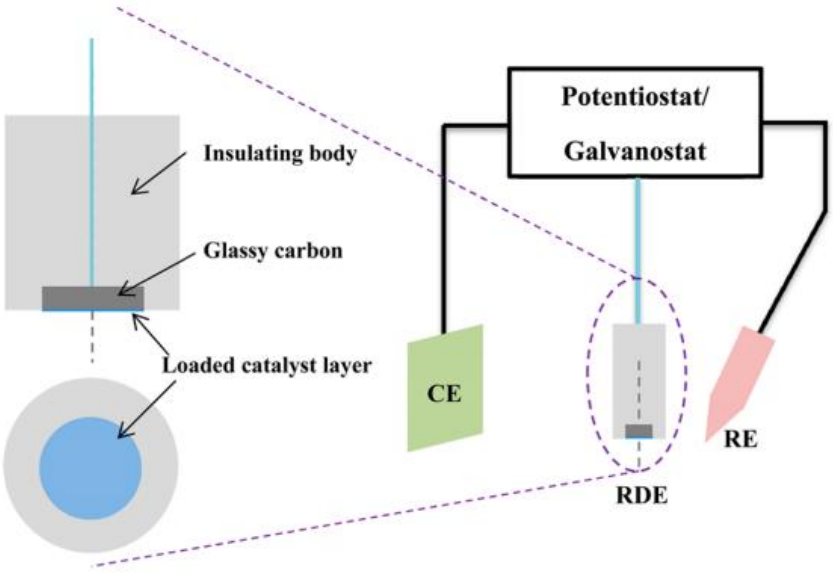

Figure 1.3. Schematic image of RDE setup in 3 electrode configurations.[26] (Copyright American Chemical Society. Reproduced with permission)

Total electrode activity is the most important and apparent factor to evaluate the catalytic performance (j_0: current density denoted in mA $cm_{geometric}^{-2}$). In general, the working electrode performance is judged by comparing the overpotential required at certain current density (e.g. 10 mA cm^{-2} or higher current density of 50 to 200 mA cm^{-2} for OER, depending on the substrate of the working electrode). Onset potential normally denotes the current that arises from the baseline (Figure 1.4). The onset potential can be obtained by the intersection of the tangents between the x axis and the rising current in the voltammogram. There is a relationship between overpotential and current density (j), the linear portion for Tafel equation is: $\eta = a + b \log(j)$ where b is a Tafel slope. The higher number of Tafel slope suggests faster kinetics for ORR and OER. Electrocatalytic active surface area (ECSA) is a key parameter to reflect the total number of active sites on a specific surface.

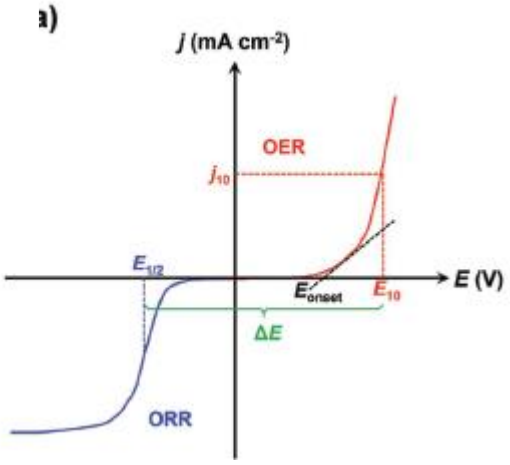

Figure 1.4. polarization curves for ORR and OER.[22] (Copyright WILEY-VCH Verlag GmbH & Co. Reproduced with permission)

1.3 Types of bifunctional electrocatalysts

1.3.1 Precious metal-based materials

Platinum supported carbon black has been considered the benchmark material for ORR catalysts and fuel cell applications due to its perfect reduction selectivity.[2] However, the excessive production cost and limited availability restrict its development. Thus, many other precious metal-based catalysts (Pd, Au, Ru,etc) are studied or combined with Pt or other transition metals to reduce the mass loading of Pt and maintain its catalytic performance. For instance, PdMo bimetallene-based battery exhibited excellent performance running at high current densities of 50 and 75 mA cm^{-2} for 300 h.[27] On the other hand, Pt alloyed with some transition metals, such as Fe, Ni, Co provided another way of enhancing the stability and performance, competed with pure Pt catalyst.[28–31] Ni_3FeN supported by ordered Fe_3Pt alloy serves as a promising bifunctional catalyst in a zinc-air battery for long term cycling test at 10 mA cm^{-2} for 480 h.[28] Another instance, RuO_2 coated nanofiber layer exhibited much improved catalytic performance and excellent rate capability due to the high electrical conductivity and fast ion diffusion.[32] Here, Table 1.1 summarizes several other precious metal based catalyst materials in rechargeable zinc-air batteries.

Table 1.1. Summary of precious metal-based materials and their performance studied at specified conditions when in rechargeable zinc-air battery.

Catalyst	Mass loading (mg cm^{-2})	Peak power density (mW cm^{-2})	Battery performance	Ref.
RuO_2@C	-	-	Potentials remained stable at 1.04 V during discharge and at 2.11 V during charge for over 40 h or 120 cycles	[33]
RuO_2-coated MMCAs	1.5-2	-	Voltage gap is stabilized at 0.8 V during 80 cycles	[32]
CoPt-9/DTM-C	0.83	140	CoPt-9/DTM-C sustained an intriguing stability of 0.82–0.90 V and 60%–58% after galvanostatic charge–discharge test for continuous 8 h	[30]

Pt3.2%@NiNS MOFs	1	108	The discharge and charge voltage at a l current density (100 mA cm^{-2}) is 0.95 and 2.07 V	[34]
PdMo	1	154.2	500 h cycling at 10 mA cm^{-2} without much difference	[27]
Fe_3Pt/Ni_3FeN	10	-	The round-trip overpotentials change from 0.72 V at the 1st cycle to 0.84 V at the 50th cycle and to 0.97 V at the 240th cycle	[28]
CuPt-NC	2	250	OCP of ~ 1.4V	[35]
RuSn73	20	93	80 h cycling at 10 mA cm^{-2}, voltage gap from 0.74 V to 0.83 V	[36]
$PtNi_{1.3}/NC$	1	154.1	Voltage gap increased 0.07 V after 500 cycles	[29]
SA-PtCoF	-	125	After 240 h cycling, voltage gap decreased from 1.03 V to 0.9 V	[31]

1.3.2 Carbon-based materials

Carbon based materials are widely investigated because of the high conductivity, intrinsic activity and tunable structure. Several methods for synthesis of carbon-based materials include heteroatoms doping, surface modification and defect engineering have been applied. These materials are usually synthesized via high temperatures at 800-1100 ℃. As reported in the literature, NDGs-800 obtained by combing C_3N_4 sheets with GO solution under hydrothermal conditions for 12 h and then freeze-dried for 48 h, followed by carbonization at high temperature, such catalyst based cells delivered a peak power density of 115.0 mW cm^{-2} and a voltage gap of 0.76 V at 10 mA cm^{-2} for 78 h.[37] 1100-CNS prepared by mixing the teflon powder with silica sphere precursor followed by high temperature treatment presented a small initial charge/discharge voltage gap of 0.77 V with a round-trip efficiency of 61% and a peak power density of 151 mW

cm^{-2}.[38] Moreover, PD/N-C was made through cutting fullerene (C60) into fragments with a etching strategy in alkaline solution showed a peak power density of 111.4 mW cm^{-2}.[39] As shown in Table 1.2, number of carbon based catalysts via different preparation procedures displays relevant battery performance. Besides, the rational heteroatoms doping into the carbon matrix exhibited improved catalytic activity and cycling stability.

Table 1.2. Summary of Carbon-based catalyst materials and their performance studied at specified conditions when in rechargeable zinc-air battery.

Catalyst	Mass loading (mg cm^{-2})	Peak power density (mW cm^{-2})	Battery performance	Ref.
1100-CNS	2	151	Initial charge/discharge voltage gap of 0.77 V, performance loss with the voltage gap increased by 85 mV after 300 cycles (55 h)	[38]
DN-CP@G	7	135	30 mV voltage gap increased after 250 cycles	[40]
PD/N-C	1	111.4	OCP stabile for 24000 s	[39]
NDGs-800	1	115.2	Voltage gap is 0.76V, remains stable after 78 h	[37]
NCNF-1100	2	144	10 min/cycle for 500 cycles voltage gap increased ~0.13 V	[41]
PS-CNF P-CNF	-	231 160	600 discharge/charge cycles conducted over a 120 h period with the constant current density of 2 mA cm^{-2}	[42]
S-NPC	2	149.9	Cycling stability for 200 min	[43]
PyN-GDY	1	136	Cycling test at 2 mA cm^{-2} for 150 h	[44]

NPS-G-2	1	151	No significant voltage drop at 10 mA cm^{-2} for 20 h	[45]

1.3.3 Transition metal-based materials

Limited by the high cost of noble or platinum group metals (PGMs), the transition metal-based catalysts are promising candidates for bifunctional operation. Due to their inexpensive and raw material rich abundance, these nonprecious transition metal-based catalysts have been broadly studied in recent years, including Mn, Co, Ni, Fe. There have been many reports that show tuning the morphology and phase of transition metals can improve the catalytic performance. Besides, pristine carbon materials such as graphene, carbon nanotubes and carbon black, which lack of active sites for the ORR/OER, are generally introduced with metal precursors to yield highly efficient electrocatalysts. Layer double hydroxide combined with cobalt-coordinated framework (LDH-POF) produced by using CNT as the template mixed with cobalt-porphyrin, then combined with NiFe layered double hydroxides (LDH) exhibited a power density of 185 mW cm^{-2} and superior cycling stability for 400 h at 5 mA cm^{-2}.[46] Another example of Co_3O_4@POF was fabricated by a two-step synthetic route in which the cobalt-coordinated framework (POF) was first synthesized and then hybridized in situ with Co_3O_4 nanoparticles maintained a voltage gap around 1.0 V for 375 h charge-discharge cycling test and a high peak power density of 222.2 mW cm^{-2}.[47] More recently, CoO_x/N-RGO was formed by using Co ions chelated with 1,10-phenanthroline and adsorbed on graphene oxide followed by high-temperature calcination under an inert atmosphere to yield a specific power density of ~ 300 W g_{cat}^{-1}.[48] Overall, the well-designed transition metal-based materials could be promising alternatives for the expensive precious PGM catalysts.

Table 1.3. Summary of transition metal-based catalyst materials and their performance studied at specified conditions when in rechargeable zinc-air battery.

Catalyst	Mass loading (mg cm^{-2})	Peak power density (mW cm^{-2})	Battery performance	Ref.
$Fe_{0.5}Co_{0.5}O_x$/NrGO	-	86	Increased from 0.79 V at the first cycle to 0.89 V at the 60th cycle	[49]
NiCoOS	-	90	Stably cycled over 170 h	[50]
Co/Co_3O_4@PGS	0.9	118.2	Voltage gap from 0.91 V to 0.96 V for over 750 cycles	[51]
Co@NPC-H	-	-	After 220 min test, the initial potential gap increased from 0.77 to 0.90 V	[52]
Co@BNCNTs	3.11	90	Voltage gap of 0.96 V over a duration of 65 h.	[53]
Co–CNT/PC	0.5	-	After 100 cycles (10 min/cycle), as the potential attenuations of the discharge and charge potential are both lower than 10%	[54]
FeNi@N-GR	2	85	120 cycles for 40 h	[55]
P−Co_4N/CNW/CC	-	135	Voltage gap of 0.84 V cycling for 408 cycles (136 h)	[56]
Co_2P@CNF	-	121	Voltage gap of 0.66 V for the 1st cycle and 0.69 V for the 210th cycle	[57]

Co-N-C-CH_3CN	-	88.9	Cycled over 3500 min without visible voltage losses	[58]
Fe-N-C	1	225.1	Voltage gap of 0.71V after 400 cycles at 4 mA cm^{-2}	[59]
Co-N-C nanosheets	-	132	A small charge–discharge voltage gap of 0.82 V at 10 mA cm^{-2} for 1000 cycles	[60]
CoNi-SAs/NC	14	101.4	voltage gap of 0.82 V for 95 cycles	[61]

1.3.4 MOF based materials

Metal-organic frameworks, famously known as MOFs, comprised of metal nodes and organic ligands, are popular porous materials for various energy and environmental related applications.[62–65] Every year a great number of MOFs and their derivative products are explored exponentially. The specific advantages of the materials are the diversity choices of metal centres and organic linker coordination, structure modification to different dimensions, tuneable pore size and high surface area. Several routes can be used to synthesize MOFs. Solvothermal, microwave, sonochemical, mechanochemical and electrochemical synthesis methods have all been developed.[66,67] In general, solvothermal synthesis is the most widely applied and straightforward method. The mixture of the metal salt and organic linker dissolved in a high boiling point solvent (e.g., Dimethylformamide, N,N-Diethylformamide or Dimethyl sulfoxide), then the solution transfer into the autoclave, the container can provide a high pressure and temperature environment, to form crystals. Parameters could affect the topology obtained and the crystal size. The parameters varied include time, temperature, solvent, pH, the ratio between the metal precursor and the linker.

In some circumstances, when the metal-ligand bonds are very strong, a modulator can be used to slow the process of growing crystals. Monotopic linkers like many acids are used to as the modulator (e.g., benzoic acid, citric acid, acetic acid). The use of a modulator in some cases can

cause defects in MOFs. Defects can influence the performance of the MOFs in many ways, such as surface areas, porosities, and catalytic activity. The crystal size and topology can also be affected by using different modulators.[68]

MOF-derived materials are normally defined as materials converted from MOF-based precursors/templated by a series of post-processing, such as direct carbonising, chemical modification and surface decoration.[63] Such materials attracted a great attention, specifically in gas storage/separations as well as electrochemical energy conversion/storage. For example, MOF-derived composites of inherent heteroatom doped carbon, and metal oxide nanostructures or combinations intensively investigated for oxygen and hydrogen catalysis reactions (ORR, OER and HER – oxygen reduction, evolution and hydrogen evolution reactions), the main reactions in fuel-cells, metal-air batteries and water electrolysers. Most of the MOF-derived catalysts are produced by treating MOFs under extreme chemical manipulations, such as either carbonisation of MOF-alone and/or introducing a large amount of extra precursor metal complex as heteroatom (N, S, P, etc) dopants at elevated temperatures. Recent studies also show some promising electrocatalytically active MOFs materials in their 2-dimensional (2D) form, and/or enriched with surface coordinatively unsaturated bi- or tri-metal cation sites. For instance, a drastically enhanced OER activity is reported in the Fe/Ni/Co(Mn)-MOFs from parent MOFs.[69–71] Their OER performance is further enhanced by controlling the morphology and aligned growth on nickel foam supports. A remarkably improved OER activity is attained from specifically designed ultrathin bimetallic Ni–Fe–MOFs nanosheets of a few nanometres in thickness, compared to a similar crystal phase, single metal 2D Ni-MOFs nanosheets or a bulk 3D parent Fe-MOFs particles.[72,73] In another case, HER and OER bifunctional electrocatalytic performance is reported from Co_3S_4/MOFs hybrid grown on conductive carbon cloth.[74] Rationally designed bimetallic MOFs containing Co-based boron imidazolate framework (BIF-91) incorporated with Fe^{3+} resulted in enhanced OER activity compared to the parent BIF.[75] On a similar basis, the OER activity is also attained from zeolitic imidazolate frameworks (ZIFs) based structures. For example, bimetallic layered double hydroxide salts (LDHSs) nanowire arrays with ZIF-67 flower-like structures and cobalt-hydroxides/oxides are also designed to extract OER activity with respect to ZIF-67.[76–78] A negligible OER activity at pH = 7 is reported in ZIF-67.

Besides, MOF-derived materials with atomically dispersed metal sites also presents excellent performance for ZAB. As reported in the literature and summarized in Table 1.4, Co-SAs@NC (SAs refers to single atoms) produced by pyrolysis of bimetallic Co/Zn-ZIFs at 900 °C followed by further acid washing to remove the metal aggregates could show a peak power density of about 105.0 mW cm^{-2}.[30] Co_3O_4@N-CNMAs/CC sample also exhibits the much lower peak power density of around 75 mW cm^{-2} synthesized via multistep-precursor design, such as growing MOF-on-MOF on carbon cloth (CC), i.e., 3D ZIF-67 on 2D ZIF-L at CC followed by two-step process of carbonization and oxidation.[26] $Fe_{0.5}Co_{0.5}O_x$/NrGO formed by growing MOFs on reduced graphene oxide in an extended synthesis process, involving significant salt ($KMnO_4$) and acid (H_2SO_4) consumption and washing followed by heat treatment could yield a peak power density of 86 mW cm^{-2}.[46]

Table 1.4. Summary of MOF-derived catalyst materials and their performance studied at specified conditions when in rechargeable zinc-air battery.

Catalyst	Mass loading (mg cm^{-2})	Peak power density (mW cm^{-2})	Battery performance	Ref.
FeCo-NCNFs-800	1	74	Initial voltage gap from 0.88 V to 0.99 V, elevated relatively by 11% after cycling for 2500 min.	[79]
Co-MOF	10	86.2	Voltage gap ~ 1 V for 70 h at a constant charge discharge current density of 6 mA cm^{-2}	[80]
ZnCo-PVP-900-acid	1	93.4	The peak power density of 93.4 mW cm^{-2} at 0.87 V	[81]
MOF-C2-900	0.5	105	No significant potential drop for 40 h at 5 and 10 mA cm^{-2}	[82]

(Zn, Co)/NSC	5	150	discharged for 22 h at a current density of 5 mA cm^{-2}	[83]
Mn/Fe-HIB-MOFs	0.5	195	10 min/cycle for 5400 cycles	[11]
PcCu-O8-Co	1	94	OCV of 1.37 V, discharge current density of 120 mA cm^{-2} at 0.8 V	[84]
Co-MOF on graphite foam	10	86.2	Charge–discharge stability over a period of 70 h at a current density 6mA cm^{-2}	[85]
CoNi-MOF-rGO	-	97	A stable voltage plateau of about 1.31 V at 5 mA cm^{-2} for 30 h	[86]
PCN-226	0.5	133	No obvious voltage gap decreases observed after 160 h charge-discharge cycles at 2 mA cm^{-2}	[87]

1.4 Challenges and objectives

Compared with the commercialized Li-ion batteries, zinc-air batteries are still facing technical hurdles that need to be overcome. First, the poor energy transfer efficiency of rechargeable zinc-air batteries less than 60%, which is limited by the overpotential at the air electrode. Focusing on the air catalyst and electrode structure is important. Therefore, desirable bifunctional catalyst to improve battery performance to expedite the ORR kinetics and reduce the charge potential would benefit the battery performance and extend its life cycling. Second, dendrite formation on the zinc anode is one of the important issues restricted the cycling life of rechargeable cells. During the recharge process, the reaction to dissociate zinc is reversible and is usually deposited on the surface of the electrode which impedes battery cycling life. So, the study of suitable electrolytes is also of great importance to reduce the discharge product.

In summary, despite the fact that the current performance is not satisfied for the commercial applications, there is no reason to doubt the tremendous potential for zinc-air batteries as the next generation energy storage technologies in future.

1.5 References

[1] Z. Yang, J. Zhang, M. C. W. Kintner-Meyer, X. Lu, D. Choi, J. P. Lemmon, J. Liu, *Chem. Rev.* **2011**, *111*, 3577.

[2] Y. Jiao, Y. Zheng, M. Jaroniec, S. Z. Qiao, *Chem. Soc. Rev.* **2015**, *44*, 2060.

[3] J. Fu, R. Liang, G. Liu, A. Yu, Z. Bai, L. Yang, Z. Chen, *Adv. Mater.* **2019**, *31*, 1805230.

[4] Y. Li, J. Lu, *ACS Energy Lett.* **2017**, *2*, 1370.

[5] H. Yadegari, X. Sun, *Acc. Chem. Res.* **2018**, *51*, 1532.

[6] J. Ryu, M. Park, J. Cho, *Adv. Mater.* **2019**, *31*, 1804784.

[7] P. Reinsberg, C. J. Bondue, H. Baltruschat, *J. Phys. Chem. C* **2016**, *120*, 22179.

[8] C.-S. Li, Y. Sun, F. Gebert, S.-L. Chou, *Adv. Energy Mater.* **2017**, *7*, 1700869.

[9] X. Zhu, C. Hu, R. Amal, L. Dai, X. Lu, *Energy Environ. Sci.* **2020**, *13*, 4536.

[10] M. A. Rahman, X. Wang, C. Wen, *J. Electrochem. Soc.* **2013**, *160*, A1759.

[11] S. S. Shinde, C. H. Lee, J.-Y. Jung, N. K. Wagh, S.-H. Kim, D.-H. Kim, C. Lin, S. U. Lee, J.-H. Lee, *Energy Environ. Sci.* **2019**, *12*, 727.

[12] H. F. Wang, Q. Xu, *Matter* **2019**, *1*, 565.

[13] Y. Li, H. Dai, *Chem. Soc. Rev.* **2014**, *43*, 5257.

[14] J. Fu, Z. P. Cano, M. G. Park, A. Yu, M. Fowler, Z. Chen, *Adv. Mater.* **2017**, *29*, 1604685.

[15] W. Hong, Z. Jia, B. Wang, *J. Appl. Electrochem.* **2016**, *46*, 1085.

[16] J.-S. Lee, S. Tai Kim, R. Cao, N.-S. Choi, M. Liu, K. T. Lee, J. Cho, *Adv. Energy Mater.* **2011**, *1*, 34.

[17] P. Pei, K. Wang, Z. Ma, *Appl. Energy* **2014**, *128*, 315.

[18] Y. Li, M. Gong, Y. Liang, J. Feng, J.-E. Kim, H. Wang, G. Hong, B. Zhang, H. Dai, *Nat. Commun.* **2013**, *4*, 1805.

[19] P. Kanninen, B. Eriksson, F. Davodi, M. E. M. Buan, O. Sorsa, T. Kallio, R. W. Lindström, *Electrochim. Acta* **2020**, *332*, 135384.

[20] H. Tang, Z. Qi, M. Ramani, J. F. Elter, *J. Power Sources* **2006**, *158*, 1306.

[21] W. Wang, J. Luo, S. Chen, *Chem. Commun.* **2017**, *53*, 11556.

[22] Z.-F. Huang, J. Wang, Y. Peng, C.-Y. Jung, A. Fisher, X. Wang, *Adv. Energy Mater.* **2017**, *7*, 1700544.

[23] Z. W. Seh, J. Kibsgaard, C. F. Dickens, I. Chorkendorff, J. K. Nørskov, T. F. Jaramillo, *Science.* **2017**, *355*, eaad4998.

[24] A. Kulkarni, S. Siahrostami, A. Patel, J. K. Nørskov, *Chem. Rev.* **2018**, *118*, 2302.

[25] Q. Zhao, Z. Yan, C. Chen, J. Chen, *Chem. Rev.* **2017**, *117*, 10121.

[26] X. Ge, A. Sumboja, D. Wuu, T. An, B. Li, F. W. T. Goh, T. S. A. Hor, Y. Zong, Z. Liu, *ACS Catal.* **2015**, *5*, 4643.

[27] M. Luo, Z. Zhao, Y. Zhang, Y. Sun, Y. Xing, F. Lv, Y. Yang, X. Zhang, S. Hwang, Y. Qin, J.-Y. Ma, F. Lin, D. Su, G. Lu, S. Guo, *Nature* **2019**, *574*, 81.

[28] Z. Cui, G. Fu, Y. Li, J. B. Goodenough, *Angew. Chem. Int. Ed.* **2017**, *56*, 9901.

[29] H. Ji, M. Wang, S. Liu, H. Sun, J. Liu, T. Qian, C. Yan, *Energy Storage Mater.* **2020**, *27*, 226.

[30] K. Wang, Z. Tang, W. Wu, P. Xi, D. Liu, Z. Ding, X. Chen, X. Wu, S. Chen, *Electrochim. Acta* **2018**, *284*, 119.

[31] Z. Li, W. Niu, Z. Yang, N. Zaman, W. Samarakoon, M. Wang, A. Kara, M. Lucero, M. V. Vyas, H. Cao, H. Zhou, G. E. Sterbinsky, Z. Feng, Y. Du, Y. Yang, *Energy Environ. Sci.* **2020**, *13*, 884.

[32] Z. Guo, C. Li, W. Li, H. Guo, X. Su, P. He, Y. Wang, Y. Xia, *J. Mater. Chem. A* **2016**, *4*, 6282.

[33] H.-S. Park, E. Seo, J. Yang, Y. Lee, B.-S. Kim, H.-K. Song, *Sci. Rep.* **2017**, *7*, 7150.

[34] Z. Xia, J. Fang, X. Zhang, L. Fan, A. J. Barlow, T. Lin, S. Wang, G. G. Wallace, G. Sun, X. Wang, *Appl. Catal. B Environ.* **2019**, *245*, 389.

[35] V. M. Dhavale, S. Kurungot, *ACS Catal.* **2015**, *5*, 1445.

[36] T.-H. You, C.-C. Hu, *ACS Appl. Mater. Interfaces* **2018**, *10*, 10064.

[37] Q. Wang, Y. Ji, Y. Lei, Y. Wang, Y. Wang, Y. Li, S. Wang, *ACS Energy Lett.* **2018**, *3*, 1183.

[38] Z. Pei, H. Li, Y. Huang, Q. Xue, Y. Huang, M. Zhu, Z. Wang, C. Zhi, *Energy Environ. Sci.* **2017**, *10*, 742.

[39] J. Zhu, Y. Huang, W. Mei, C. Zhao, C. Zhang, J. Zhang, I. S. Amiinu, S. Mu, *Angew. Chem. Int. Ed.* **2019**, *58*, 3859.

[40] C. Hang, J. Zhang, J. Zhu, W. Li, Z. Kou, Y. Huang, *Adv. Energy Mater.* **2018**, *8*, 1703539.

[41] Q. Liu, Y. Wang, L. Dai, J. Yao, *Adv. Mater.* **2016**, *28*, 3000.

[42] S. S. Shinde, J. Y. Yu, J. W. Song, Y. H. Nam, D. H. Kim, J. H. Lee, *Nanoscale Horizons* **2017**, *2*, 333.

[43] C. Zhao, G. Liu, N. Sun, X. Zhang, G. Wang, Y. Zhang, H. Zhang, H. Zhao, *Chem. Eng. J.* **2018**, *334*, 1270.

[44] Q. Lv, N. Wang, W. Si, Z. Hou, X. Li, X. Wang, F. Zhao, Z. Yang, Y. Zhang, C. Huang, *Appl. Catal. B Environ.* **2020**, *261*, 118234.

[45] X. Zheng, J. Wu, X. Cao, J. Abbott, C. Jin, H. Wang, P. Strasser, R. Yang, X. Chen, G. Wu, *Appl. Catal. B Environ.* **2019**, *241*, 442.

[46] C. Zhao, J. Liu, B. Li, D. Ren, X. Chen, J. Yu, Q. Zhang, *Adv. Funct. Mater.* **2020**, *30*, 2003619.

[47] B.-Q. Li, S.-Y. Zhang, B. Wang, Z.-J. Xia, C. Tang, Q. Zhang, *Energy Environ. Sci.* **2018**, *11*, 1723.

[48] T. Zhou, W. Xu, N. Zhang, Z. Du, C. Zhong, W. Yan, H. Ju, W. Chu, H. Jiang, C. Wu, Y. Xie, *Adv. Mater.* **2019**, *31*, 1807468.

[49] L. Wei, H. E. Karahan, S. Zhai, H. Liu, X. Chen, Z. Zhou, Y. Lei, Z. Liu, Y. Chen, *Adv. Mater.* **2017**, *29*, 1701410.

[50] Z. Bai, S. Li, J. Fu, Q. Zhang, F. Chang, L. Yang, J. Lu, Z. Chen, *Nano Energy* **2019**, *58*, 680.

[51] Y. Jiang, Y.-P. Deng, J. Fu, D. U. Lee, R. Liang, Z. P. Cano, Y. Liu, Z. Bai, S. Hwang, L. Yang, D. Su, W. Chu, Z. Chen, *Adv. Energy Mater.* **2018**, *8*, 1702900.

[52] Y.-N. Hou, Z. Zhao, H. Zhang, C. Zhao, X. Liu, Y. Tang, Z. Gao, X. Wang, J. Qiu, *Carbon.* **2019**, *144*, 492.

[53] L. Ma, R. Wang, Y.-H. Li, X.-F. Liu, Q.-Q. Zhang, X.-Y. Dong, S.-Q. Zang, *J. Mater. Chem. A* **2018**, *6*, 24071.

[54] S. Dou, X. Li, L. Tao, J. Huo, S. Wang, *Chem. Commun.* **2016**, *52*, 9727.

[55] P. Liu, D. Gao, W. Xiao, L. Ma, K. Sun, P. Xi, D. Xue, J. Wang, *Adv. Funct. Mater.* **2018**, *28*, 1706928.

[56] F. Meng, H. Zhong, D. Bao, J. Yan, X. Zhang, *J. Am. Chem. Soc.* **2016**, *138*, 10226.

[57] J. Gao, J. Wang, L. Zhou, X. Cai, D. Zhan, M. Hou, L. Lai, *ACS Appl. Mater. Interfaces* **2019**, *11*, 10364.

[58] H. Mei, M. Yang, Y. Shen, F. He, Z. Zhou, X. Chen, Y. Yang, S. Liu, Y. Zhang, *Carbon.* **2019**, *144*, 312.

[59] J. Zhang, M. Zhang, Y. Zeng, J. Chen, L. Qiu, H. Zhou, C. Sun, Y. Yu, C. Zhu, Z. Zhu, *Small* **2019**, *15*, 1900307.

[60] P. Yu, L. Wang, F. Sun, Y. Xie, X. Liu, J. Ma, X. Wang, C. Tian, J. Li, H. Fu, *Adv. Mater.* **2019**, *31*, 1901666.

[61] X. Han, X. Ling, D. Yu, D. Xie, L. Li, S. Peng, C. Zhong, N. Zhao, Y. Deng, W. Hu, *Adv. Mater.* **2019**, *31*, 1905622.

[62] Y. Xue, S. Zheng, H. Xue, H. Pang, *J. Mater. Chem. A* **2019**, *7*, 7301.

[63] J. Liu, D. Zhu, C. Guo, A. Vasileff, S. Z. Qiao, *Adv. Energy Mater.* **2017**, *1700518*, 1.

[64] K. Zhang, K. O. Kirlikovali, Q. Van Le, Z. Jin, R. S. Varma, H. W. Jang, O. K. Farha, M. Shokouhimehr, *ACS Appl. Nano Mater.* **2020**, *3*, 3964.

[65] Y. Xu, Q. Li, H. Xue, H. Pang, *Coord. Chem. Rev.* **2018**, *376*, 292.

[66] Z. J. Lin, Z. Yang, T. F. Liu, Y. B. Huang, R. Cao, *Inorg. Chem.* **2012**, *51*, 1813.

[67] M. Rubio-Martinez, C. Avci-Camur, A. W. Thornton, I. Imaz, D. Maspoch, M. R. Hill, *Chem. Soc. Rev.* **2017**, *46*, 3453.

[68] X. Xiao, L. Zou, H. Pang, Q. Xu, *Chem. Soc. Rev.* **2020**, *49*, 301.

[69] F.-L. Li, Q. Shao, X. Huang, J.-P. Lang, *Angew. Chem. Int. Ed.* **2018**, *57*, 1888.

[70] J. Teng, M. Chen, Y. Xie, D. Wang, J. J. Jiang, G. Li, H. P. Wang, Y. Fan, Z. W. Wei, C. Y. Su, *Chem. Mater.* **2018**, *30*, 6458.

[71] Q. Qian, Y. Li, Y. Liu, L. Yu, G. Zhang, *Adv. Mater.* **2019**, *31*, 1901139.

[72] F. L. Li, P. Wang, X. Huang, D. J. Young, H. F. Wang, P. Braunstein, J. P. Lang, *Angew. Chem. Int. Ed.* **2019**, *58*, 7051.

[73] L. Zhuang, L. Ge, H. Liu, Z. Jiang, Y. Jia, Z. Li, D. Yang, R. K. Hocking, M. Li, L. Zhang, X. Wang, X. Yao, Z. Zhu, *Angew. Chem. Int. Ed.* **2019**, *58*, 13565.

[74] T. Liu, P. Li, N. Yao, T. Kong, G. Cheng, S. Chen, W. Luo, *Adv. Mater.* **2019**, *31*, 1806672.

[75] T. Wen, Y. Zheng, J. Zhang, K. Davey, S. Qiao, *Adv. Sci.* **2019**, *6*, 1801920.

[76] W. Chen, Y. Zhang, G. Chen, Y. Zhou, X. Xiang, K. K. Ostrikov, *ACS Sustain. Chem. Eng.* **2019**, *7*, 8255.

[77] Q. Zha, W. Xu, X. Li, Y. Ni, *Dalt. Trans.* **2019**, *48*, 12127.

[78] D. Su, X. Zhang, A. Wu, H. Yan, Z. Liu, L. Wang, C. Tian, H. Fu, *NPG Asia Mater.* **2019**, *11*, 78.

[79] L. Yang, S. Feng, G. Xu, B. Wei, L. Zhang, *ACS Sustain. Chem. Eng.* **2019**, *7*, 5462.

[80] G. Chen, J. Zhang, F. Wang, L. Wang, Z. Liao, E. Zschech, K. Müllen, X. Feng, *Chem. – A Eur. J.* **2018**, *24*, 18413.

[81] C. Deng, K. H. Wu, J. Scott, S. Zhu, X. Zheng, R. Amal, D. W. Wang, *ACS Appl. Mater. Interfaces* **2019**, *11*, 9925.

[82] M. Zhang, Q. Dai, H. Zheng, M. Chen, L. Dai, *Adv. Mater.* **2018**, *30*, 1705431.

[83] D. Liu, B. Wang, H. Li, S. Huang, M. Liu, J. Wang, Q. Wang, J. Zhang, Y. Zhao, *Nano Energy* **2019**, *58*, 277.

[84] H. Zhong, K. H. Ly, M. Wang, Y. Krupskaya, X. Han, J. Zhang, J. Zhang, V. Kataev, B. Büchner, I. M. Weidinger, S. Kaskel, P. Liu, M. Chen, R. Dong, X. Feng, *Angew. Chem. Int. Ed.* **2019**, *58*, 10677.

[85] G. Chen, J. Zhang, F. Wang, L. Wang, Z. Liao, E. Zschech, K. Müllen, X. Feng, *Chem. – A Eur. J.* **2018**, *24*, 18413.

[86] X. Zheng, Y. Cao, D. Liu, M. Cai, J. Ding, X. Liu, J. Wang, W. Hu, C. Zhong, *ACS Appl. Mater. Interfaces* **2019**, *11*, 15662.

[87] M. O. Cichocka, Z. Liang, D. Feng, S. Back, S. Siahrostami, X. Wang, L. Samperisi, Y. Sun, H. Xu, N. Hedin, H. Zheng, X. Zou, H.-C. Zhou, Z. Huang, *J. Am. Chem. Soc.* **2020**, *142*, 15386.

Chapter 2. Characterization methods

Powder X-ray diffraction (PXRD) is a very useful technique can check the atomic and molecular structure of a crystal, because the beam of incident X-rays would be diffracted into many specific directions caused by the crystal atoms. PXRD patterns can be used to confirm the structure of a MOF by comparing the experimental powder pattern to simulated patterns generated from single crystal X-ray data. In this thesis, a thin film Mo mode is using for collecting x-ray powder diffraction pattern, as can be seen in chapter 3, the XRD pattern show asymmetric peak shape which might cause by the assembling technic. As shown in Figure 3.4, bimetallic ZIFs exhibit asymmetric peaks. It's because the diffraction cone diameter reduces to zero, at zero degrees and the smaller the cone, the greater the distortion is at the detector. It's a function of powder diffraction geometry. The lower the peak angle, the higher the asymmetry will be.

Scanning electron microscope (SEM) shows images of a sample and is a powerful tool to check the morphology, crystal size and elemental composition of specimen at particular region of interest with additional piece of kit, EDS (Energy dispersive spectra), attached to the SEM machine. The electrons contact with atoms from the sample, then the signals received from the instrument comprise useful information about the surface topography and composition of samples. For instance, in Chapter 4 EDS is used to confirm the existence of Co, Pt and N element of ZIF-67/Pt composites distribute evenly on the carbon paper.

Transmission electron microscopy (TEM) is another type of imaging microscopy, works on the transmission mode compared to reflecting mode in SEM, in which a beam of electrons is transmitted through a thin specimen to generate an image. TEM can present images with higher resolution than other microscopes because of the smaller de Broglie wavelength of electrons. Therefore, the instrument can capture more details of the sample, for example, estimation of particle size and distribution of the sample below 50 nm to a nm length scale, lattice planes, and determine crystal structures of particular phases within the composite from electron diffraction pattern. In chapter 5, the main phase of the materials is suggested by the average lattice spacing of 0.243 and 0.238 nm from Co_3O_4 and $Co(OH)_2$ observed by TEM.

Adsorption isotherms are widely applied to determine apparent surface areas, pore volumes and pore size distributions for MOFs. The four typical shapes of adsorption/desorption isotherms can also provide details of porosity characteristics of the materials. For the most practical parameter applied is nitrogen (N_2) gas adsorption at 77 K. To get reliable results, the selection of data analysis model is essential. Now BET theory is the best default practice for calculating the apparent surface area because the pore sizes of most MOFs in favor of multilayer gas adsorption. The Langmuir theory is valid only for analyzing monolayer adsorption. And it is known that BET surface area attained from isotherms can match the geometric surface areas generate from the crystal structure.

Raman spectroscopy is applied to observe vibrational, rotational and other low frequency modes in a material. The laser light interacts with molecular vibrations, phonons in the sample. Raman spectroscopy provides an invaluable analytical path for molecular finger printing as well as monitoring changes in molecular bond structure. One of the advantages of using Raman microscope is that it offers the selection of optimal laser excitation wavelength to meet the best resonance with sample under investigation.

FTIR is a technique used to acquire the infrared spectrum of absorption or emission of a solid, liquid or gas. When IR radiation is passed through a sample, part of the radiation is absorbed by the sample and some passes through. The resulting signal detected from the spectrum representing a molecular fingerprint of the sample. Different chemical structures can produce different spectral fingerprints.

XPS is a surface-sensitive quantitative spectroscopic technique that measures the elemental composition at ppt level. XPS can be used to study the surface chemistry of a material in its as-received state. In principle, XPS can detect any elements with its atomic number above 3. Besides, elements and the quantity of those elements are present within the top 1-12 microns of the sample surface can be detected by XPS.

Thermogravimetric analysis (TGA) is commonly used to determine the mass loss or gain of a sample under constant increasing temperature. Due to the mass change as a function of increasing temperature or time, the degradation mechanisms and kinetics of reaction can be studied. Besides, TGA can be a useful tool for testing the sample stability under high temperature. When testing the thermal stability, the carrier gas can affect the decomposition pathway.

Chapter 3. Synthesis and optimisation of zeolitic imidazolate frameworks for oxygen evolution reaction

3.1 Introduction

MOFs and their derived nanostructures have created phenomenal interest for numerous applications, such as gas uptake/separation, and heterogeneous and electrochemical catalysis.[1–10] For example, carbon based materials derived from MOFs have shown great promise for electrocatalytic reactions in ORR, OER and HER. However, carbonization of MOFs poses significant challenges for reproducibility in terms of controlling composition, functionality, heterogeneity, porosity and nanophase (i.e. aggregation of metal centres or loss of structure), as well as for mass production. Thus, the structures often show complex structure-performance relationships.[10–13] Furthermore, the severe decomposition of the organic ligand leads to a very low-level mass yield of catalysts.[4,9] Such process is not environmentally clean as the generation of volatile species can be harmful, as well as acid washing of metal. For instance, approximately (10–20) wt% of porous carbon is formed from MOF-5 or MOF-74 (Zn).[11] Moreover, as each type of precursor MOFs exhibits different strengths of framework thermal stability, metal-ligand coordination, pore structure, and ligand functionality, it is difficult to design and standardize the thermolysis parameters to achieve desirable carbon catalyst on commercial terms.[10–13]

In general, the MOFs with open framework structure comprised of metal nodes and ligand coordination are ideal candidates to exhibit favourable electrocatalytic activities.[7,14–26] This leads to significant advantage, as such MOFs can be synthesized reproducibly. Recent studies show some promising electrocatalytically active MOFs in their 2-dimensional (2D) form, and/or enriched with surface coordinatively unsaturated bi- or tri-metal cation sites.[20–22] Their OER performance is further enhanced by controlling the morphology and growth on conduction substrates such as template nanostructures, nickel foam or carbon supports.[23–25] Rationally designed bimetallic MOFs containing cobalt-based boron imidazolate framework (BIF-91) incorporated with Fe^{3+} resulted in enhanced OER activity compared to the parent BIF.[26] Bimetallic layered double hydroxide salts nanowire arrays with ZIF-67 flower-like structures and cobalt-hydroxides/oxides are also designed to extract OER activity with respect to ZIF-67.[15–17]

Therefore, focusing on pristine MOF itself instead of modifying its structure, extensively at elevated temperatures, is highly desirable. However, there is a clear lack of reproducible, commercially available or easy and scalable synthesis of such MOFs systems. Some of the MOFs structures such as ZIF-8 or its isostructural analogue ZIF-67 are best suitable candidates if examined accordingly as they can be readily synthesized in large scale, under mild conditions or at room temperature and ambient pressure using commonly used laboratory washing solvents (e.g. methanol), by stirring, microwave, continuous flow or solid-state routes, and are also commercially available.[6] The prototype ZIF-8 exhibits high accessible surface area for many gaseous and liquid molecules.[12,27,28] Furthermore, these structures show exceptional stability under extreme chemical conditions.[28] This makes them one of the popular candidates for numerous applications, particularly in catalysis. ZIF-8/ZIF-67 formed by imidazolate linkers and a single-metal-atom (Zn or Co)–N_4 tetrahedron, is reminiscent to the proposed active M-N_4 (M = Mn, Fe, Co, etc.) sites in carbonaceous electrocatalysts.[1–10]

In this chapter, a novel strategy to extract the electrocatalytic activity from as-received ZIFs is developed. The electrochemical tests show that OER activity of ZIF-8(Zn) is gradually enhanced towards ZIF-67(Co) with the substitution of cobalt metal centres for zinc. Further to this, ZIF-67 crystallites of varied sizes, between 50 nm to 2000 nm, are studied to attain the best catalytic performance. A well-correlated performance relationship with respect to the particle-size is evidenced, in which the increased particle size leads to reduced activity. Building upon this understanding, a highly enhanced OER activity is obtained from the ZIF/carbon black composite (ZIF-67/CB). This performance is equivalent or even superior to many literature reports of carbonaceous nanostructures. The ZIF-67/CB samples also show growing evidence for oxygen reduction reaction (ORR) activity to function as dual activity for both OER and ORR. These optimized ZIF-67 samples also exhibit stable OER activity durability for several hours under repeated accelerated cyclic voltammetry (CV) and linear sweep voltammetry (LSV) scans. Interestingly, the ZIF-67 nanoparticles coated on the carbon paper showed highly increased activity stability over 24 h operation in 1 M KOH electrolyte.

3.2 Experimental Section

3.2.1 Synthesis

ZIF-8, ZIF-67 and mixed metal Co/Zn-ZIF-8 samples were synthesized in a similar method according to the reported procedure.[29] Briefly, ZIF-8 (or ZIF-67), 7.344 g of zinc nitrate hexahydrate (or cobalt nitrate hexahydrate) was dissolved in 500 ml methanol. Then, 8.106 g of 2-methyl imidazole was mixed in another 500 ml of methanol with ~4 ml 1-methylimidazole. Then the solution was stirred and slowly added to the former solution. After a few minutes, the solution changed from the clear to milky white, which was then left for a day to settle. A clear solution was poured out and the precipitate sample was extracted after several washings with methanol. All the samples were dried at 80 °C oven. The mixed metal Co/Zn-ZIF-8 samples were synthesized in a similar method but by replacing the portion of the zinc-nitrate precursor with cobalt-nitrate. For example, the sample made with 10%, 20% and 50% by mass of the cobalt-nitrate replacing the zinc-nitrate (more precisely, for 10%: 0.7344 g of cobalt-nitrate + 6.6096 g of zinc -nitrate; for 20%: 1.479 g of cobalt-nitrate + 5.875 g of zinc-nitrate; for 50%: 3.672 g of cobalt-nitrate + 3.672 g of zinc-nitrate) are named as $Co_{10}Zn_{90}$-ZIF-8, $Co_{20}Zn_{80}$-ZIF-8 and $Co_{50}Zn_{50}$-ZIF-8, respectively. was prepared by adding 8 ml 1-methylimidazole.

Synthesis of controlled particle size ZIF-67 samples: ZIF-67 with particle size of 2000 nm is synthesised similar to above described method except adding 8 ml 1-methylimidazole. ZIF-67 *with particle size of 50 nm and 200 nm are synthesised as following:* 5.9 g cobalt nitrate hexahydrate and 0.5 g polyvinylpyrrolidone (PVP) were dissolved in a 500 ml methanol. Then 6.65 g of 2-methyl imidazole was mixed in another 500 ml methanol. Then the solution was stirring and slowly added to the former solution. After a few minutes the solution changed from the clear to milky white, which was then left for a day to settle. Clear solution was poured out and the precipitate sample was extracted after several washings by methanol. All the samples were dried at 80 °C oven. The 50 nm ZIF-67 and 200 nm ZIF-67 were prepared with different amounts of TEA (triethylamine) (60 μL and 22.5 μL, respectively). Composites of ZIF-67/CB were obtained by mixing of CB and ZIF-67 powders in different mass ratios (of CB in 25 wt%, 50 wt%, and 75

wt %) using mortar and pestle hand milling method. The as-synthesized sample were then used for electrochemical test.

3.2.2 Structure and porosity characterizations

Powder X-ray diffraction patterns (PXRD) were collected by Stoe Stadi-P, Mo–K-alpha. Fourier-transform infrared (FTIR) data was obtained by Bruker ALPHA FTIR Spectrometer (Platinum-ATR) with background correction. X-ray photoemission spectroscopy (XPS, on Al–K-alpha, Thermo Scientific) data and scanning electron microscopy (SEM, on JSM6700, Jeol) measurements were carried out on the samples supported on a carbon tape. The porosity by N_2, and CO_2 adsorption-desorption isotherms were measured at 77 K and 298 K, respectively, on a Quantachrome Autosorb-iQC. All the samples were degassed at 180 ℃ overnight under a dynamic vacuum prior to the actual gas adsorption measurements. The specific surface area was measured from the 77 K N_2 isotherm in a relative pressure range between 0.01 and 0.2, according to the Brunauer–Emmett–Teller (BET) method. The pore volume was obtained from the adsorption volume at relative pressure of 0.95.

3.2.3 Electrochemical tests

All the electrochemical catalytic activity of the samples were reported using a potentiostation (Autolab, Metrohm PGSTAT302N) with a rotating-disk three-electrode (RDE) cell configuration composed of a glassy carbon rotating disk with active material as working electrode, and (1 × 1) cm^2 Pt and Ag/AgCl/saturated KCl as counter and reference electrode, respectively. All the measurements were carried out in O_2-saturated alkaline (0.1 M KOH and 1.0 M KOH) electrolyte at room temperature. The catalyst loading was fixed at ~0.28 mg cm^{-2} on a 3 mm diameter (or area of 0.0707 cm^2) glassy carbon electrode (GCE). The catalyst was prepared as follows; 2 mg of sample was dispersed in a total 500 µl solution consisting 482 µl of deionized water plus 18 µl of Nafion (5% solution) under sonication. The sonication was carried out for up to an hour to get uniform catalyst dispersion of ink. Of this 5 µl was micropipetted and dropped on to a GCE followed by drying at <60 ℃ in an oven prior to the electrochemical tests. The cyclic voltammetry (CV) and linear sweep voltammetry (LSV) curves were recorded with voltage sweeping at 10 mV s^{-1} in the potential range of +0.2 V to +1.0 V in case of OER and in the range of +0.2 V to −0.8 V

in case of ORR. OER durability tests by chronoamperometric (*I vs t*) were carried out at a fixed potential of +1.65 V (vs RHE), and the response current was recorded against time. In chronopotentiometry (*V vs t*), the response potential was recorded against time at a fixed current density of 10 mA cm^{-2}. All of the OER LSV curves were recorded at constant rpm of 1600. ORR LSV curves were recorded at discrete rotation rates between 400 rpm and 2000 rpm. All the reported current densities were estimated by normalizing the actual current response to the electrode area of GCE. The following relation is used for potential representation V (vs RHE) = $E_{Ag/AgCl}$ + 0.197 + 0.059 × pH. The overpotential is reported according to the relation; V = V_{RHE} − 1.23 V.

3.3 Results and Discussion

3.3.1 Structure characterization

Figure 3.1 shows the synthesis protocol and crystal structure of ZIF-8 and ZIF-67 samples. Characterization shows a well-developed framework structure in the samples (Figure 3.2). The as-formed ZIFs are then thoroughly characterized and used for catalytic studies without high-temperature outgassing or activation. All the sample handling is carried out under ambient atmosphere. PXRD shows the crystalline nature of samples (Figure 3.2a).[12,29] SEM micrograph shows a well-defined crystallite facets of rhombic dodecahedral nanocrystals of uniform sizes (Figure 3.2b). N_2 adsorption estimates the BET specific surface area of ~1700 m^2 g^{-1} and porosity of 0.7 cm^3 g^{-1}, which is in good agreement with the idealised structure proposed in the literature (Figure 3.2c and Table 3.1. The cobalt based ZIF-67 shows a uniform pore cavity ~1.17 nm. ZIF-8/ZIF-67 are the most illustrative ZIF materials with a sodalite zeolite-type topology, in which ZnN4(CoN4) tetrahedra are linked through imidazolate ligands forming cages which are accessible through a narrow six-ring pore of 0.34 nm. This porosity informs the quality of the ZIF structures (Figure 3.3).[29]

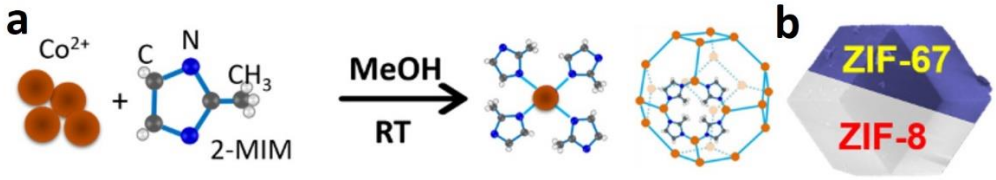

Figure 3.1. (a-b) Illustration of formation of ZIF-67 structure with a Co–N_4 coordination and a SEM image of ZIF-67 crystal. The purple and white colour crystal represent the isostructural ZIF-67 and ZIF-8, respectively.

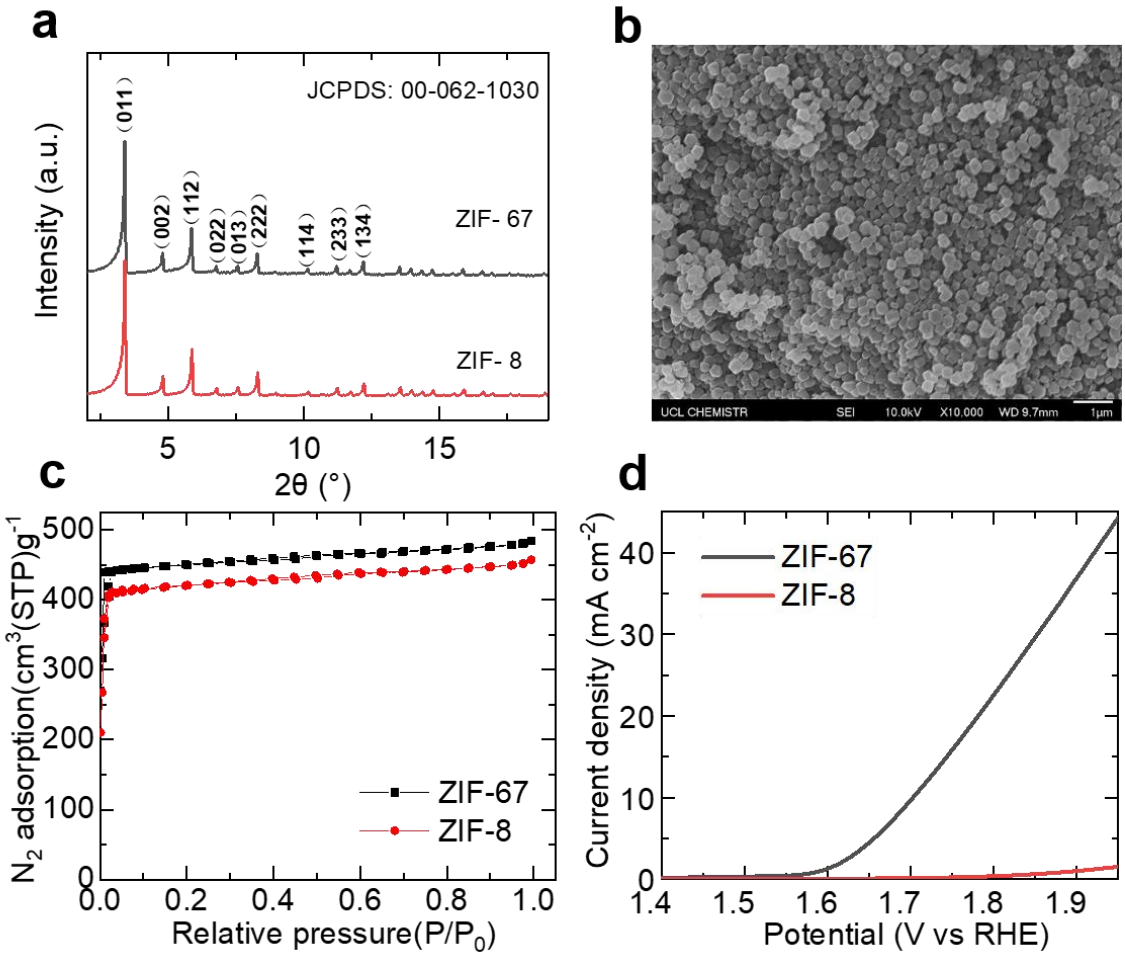

Figure 3.2. Structural and OER characteristics of ZIF-8 and ZIF-67: (a) PXRD patterns. **(b)** SEM image of ZIF-67 with average particle size of 200 nm. **(c)** Nitrogen adsorption-desorption isotherms. **(d)** OER LSV curves.

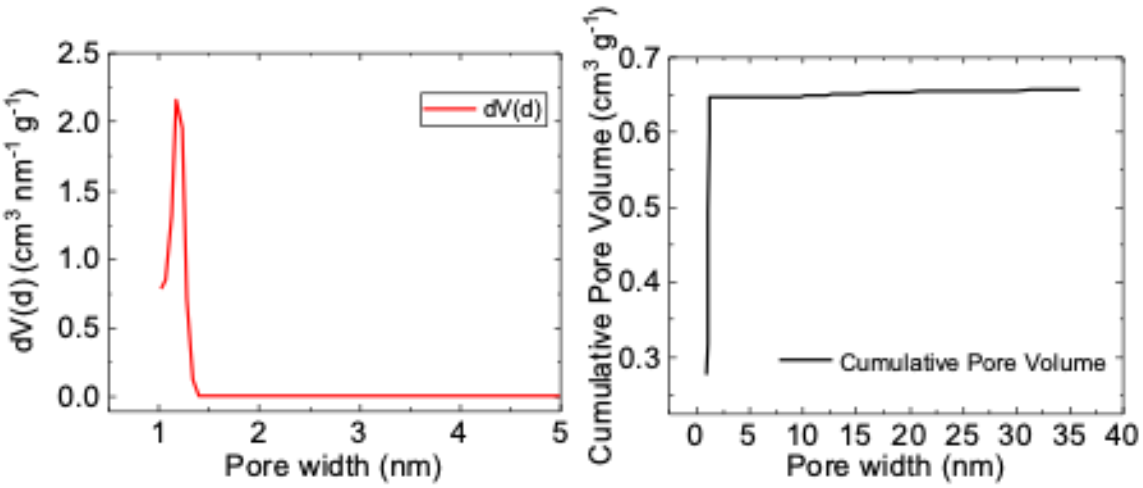

Figure 3.3. Pore size distribution and cumulative pore volume plots of ZIF-67. The QSDFT (quenched solid density functional theory) method with slit/cylindrical pores was applied to the desorption isotherm (10^{-2} to 0.99, P P_o^{-1}) to obtain the pore size distribution and cumulative pore volume.

Table 3.1. The specific surface area and porosity in the $Zn_{100-x}Co_x$-ZIF-8. The specific surface area was measured from the 77 K N_2 isotherm in a relative pressure range between 0.01 and 0.2, according to the Brunauer–Emmett–Teller (BET) method.

Sample	SSA [m^2 g^{-1}]	V_{micro} [cm^3 g^{-1}]
ZIF-67	1729.1	0.740
$Co_{70}Zn_{30}$-ZIF-8	1712.2	0.808
$Co_{50}Zn_{50}$-ZIF-8	1714.1	0.752
$Co_{30}Zn_{70}$-ZIF-8	1861.4	0.758

$Co_{10}Zn_{90}$-ZIF-8	1692.6	0.711
ZIF-8	1632.6	0.707
ZIF-67 (50 nm)	1780.5	2.015
ZIF-67 (200 nm)	1644.4	1.027
ZIF-67 (2000 nm)	1632.0	0.701

3.3.2 Electrochemical catalytic performance

As shown in Figure 3.2d, the initial assessment of samples shows surprising OER activity difference between ZIF-8 and ZIF-67. The ZIF-8 exhibits a negligible OER activity compared to a high current response from ZIF-67. A potential of ~1.72 V (vs RHE with onset potential being close to 1.6 V) to reach an impressive benchmark current density of 10 mA cm^{-2} is comparable to many of the carbon-based nanostructures.[19,27,29,30] In order to explore the OER activity evolution from ZIF-8 to ZIF-67, a series of bimetallic $Zn_{100-x}Co_x$-ZIF-8 samples of controlled particle size, is rationally designed with gradual replacement of zinc metal centres by cobalt (Figure 3.4a-b). All the samples are isostructural in nature with high crystallinity, framework and porosity as the parent ZIF-8 structure (Figure 3.4c-e, and Table 3.1). All of the bimetallic samples exhibit same type I nitrogen isotherm which indicate microporous structure and the surface area is also similar. Pore volume between the bimetallic samples are in the range of 0.7 - 0.8 cm^3 g^{-1}. It is interesting to note that the LSV curves reveal a continuously enhanced OER activity when going from a zinc-based ZIF-8 to a cobalt-based ZIF-67 (Figure 3.4f). The samples colour and XPS further confirms the coexistence of Zn^{2+} and Co^{2+} in the bimetallic ZIFs (Figure 3.5).[29] Thermogravimetry curves demonstrate a clear change in their thermal stability and residual mass with an increase of the cobalt-metal substitution for the zinc (Figure 3.6). Though the combination of metal centres or bimetallic ZIFs does not offer any synergistic effect for improved OER activity, it confirms that most of their activity can be attributed directly to the cobalt metal centres.[31]

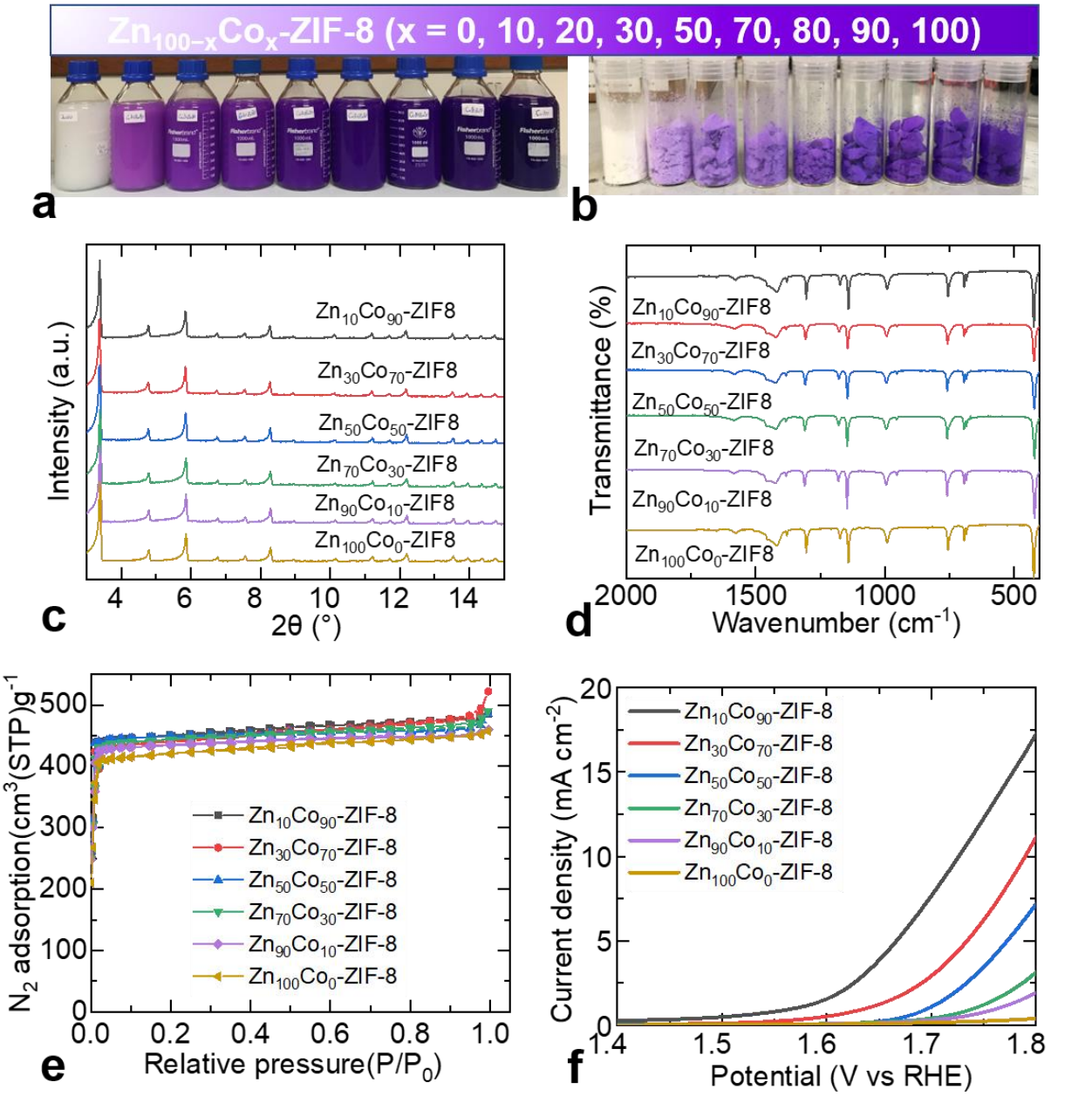

Figure 3.4. Structural characteristics and OER activities of bimetallic ZIFs, $Zn_{100-x}Co_x$-ZIF-8: (a-b) Photographs of respective reaction solvents in glass jars and powdery samples in vials – a total methanol precursors solvent of 1 litre volume in each case is used to obtain a sample of over a gram quantity. **(c)** PXRD patterns. **(d)** FTIR spectra. **(e)** Nitrogen adsorption-desorption isotherms. **(f)** LSV curves, obtained in 0.1 M KOH electrolyte.

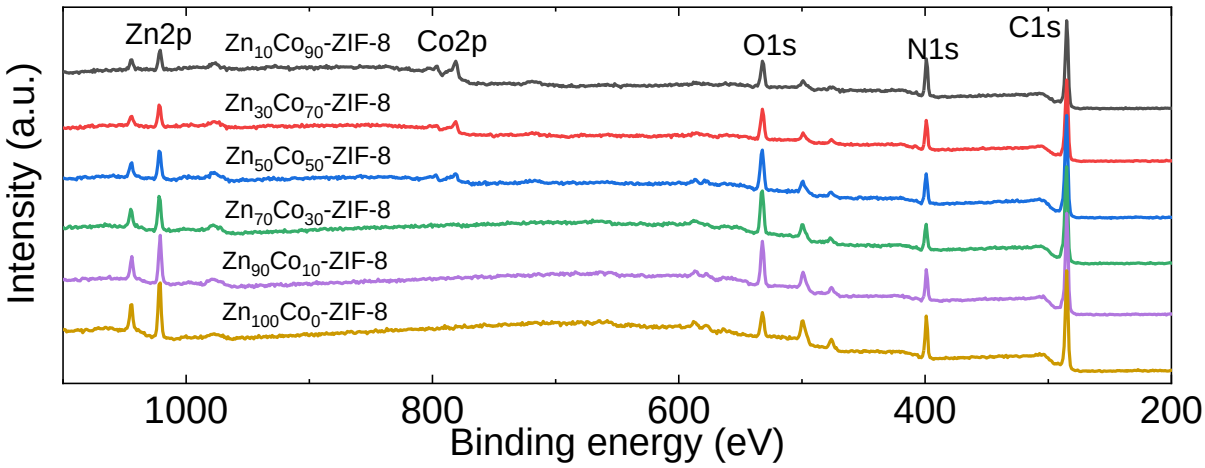

Figure 3.5. XPS survey of bimetallic ZIFs, $Zn_{100-x}Co_x$-ZIF-8.

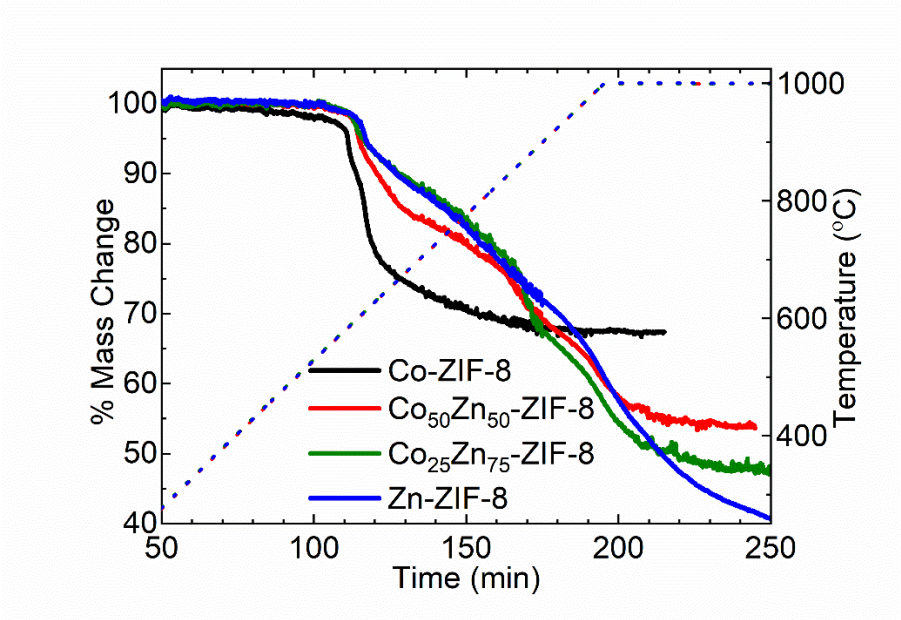

Figure 3.6. TGA curves of bimetallic $Zn_{100-x}Co_x$-ZIF-8.

Next, ZIF-67 samples of different particle sizes between 50 nm to 2000 nm are synthesized to achieve best catalytic activity performance (Figure 3.7a-b, 3.8 and 3.9). Interestingly, a well-correlated performance relationship with respect to the particle-size of ZIFs is evidenced (Figure 3.7c). A further improved OER activity is observed in the sample with particle size of ~50 nm. The overpotential required to reach a current density of 10 mA cm^{-2} is now 480 mV about 20 mV and 50 mV lower than the samples with particle sizes of 200 nm and 2000 nm respectively. As this catalytic reaction process involves solid-liquid surface-interface associated adsorption, dissociation, intermediates, migration and charge transport to the electrode collector, the smaller crystals with more active surface area are expected to show a favourable performance.[10] The above results further suggests that the catalytic activity of ZIF-67 nanoparticles can be enhanced by increasing the electrical conductivity. Hence, a set of ZIF-67/CB samples with varying amounts of CB (at 25 wt%, 50 wt% and 75 wt%) are prepared by simple physical mixing. A further noteworthy improvement in the OER performance is seen for ZIF-67/CB (50 wt%) (Figure 3.7d). Specifically, both the onset and potential at 10 mA cm^{-2} is reduced. The CB alone does not show any OER activity. Here, it is worth noting that this OER activity is comparable or better than the many carbon based nanostructures include MOF and ZIF-derived metal-incorporated carbons produced by extensive chemical treatment and concomitant energy penalty (Figure 3.7e).[19,27,29–32] For example, the OER performance of the ZIF-67 and other carbon nanostructures produced at elevated temperatures, between 700-1100 °C from the inorganic, MOF, polymeric, graphene-oxide precursors and templates, and in their heteroatom doping and metal-/metal-oxide grafting states as summarized in Table 3.2. The OER activity is also higher than the commercial Pt/C, and approaching the benchmark material, IrO_2/C (Figure 3.7e). [31] An enhanced OER activity of these ZIF-67/CB samples is also observed in the 1.0 M KOH electrolyte (inset Figure 3.7d). Now the overpotential is reduced to about 320 mV to deliver 10 mA cm^{-2}. Here, it is worth noting that all the samples are in isostructural nature and exhibit identical frameworks structure and porosity, thus the activity difference is directly attributed to their particle-size (Figure 3.8). The smallest size of ZIF-67(50 nm) also exhibit small Tafel slopes 84.4 mV dec^{-1} (Figure 3.9) The improved OER activity in the nanosized ZIF-67 can also be attributed to its excess mesoporosity formed by external surfaces from the nanoparticle assembly (Figure 3.8).

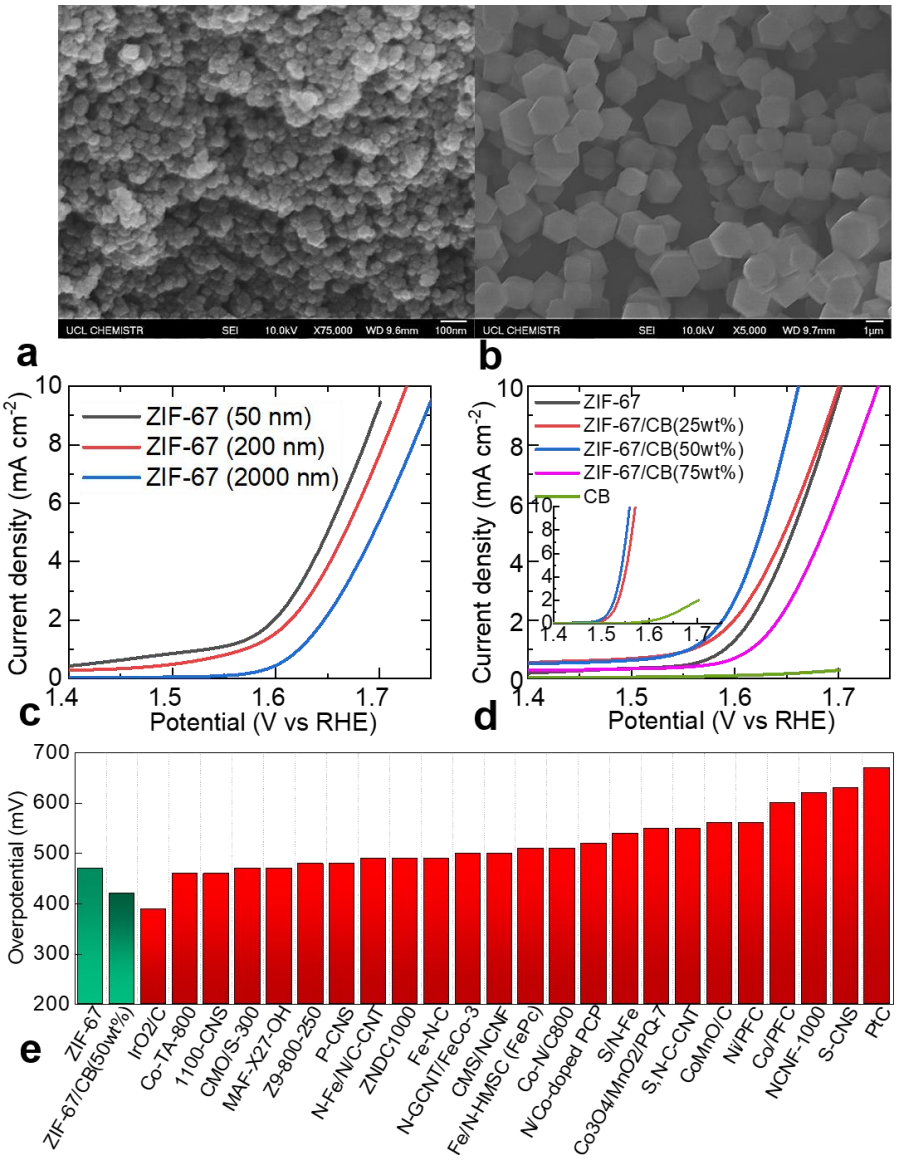

Figure 3.7. Optimised ZIF-67 and OER activity: a-b) SEM images of samples with controlled particle sizes of 50 nm and 2000 nm. **c)** LSV curves of ZIF-67 samples with different particle sizes, measured in 0.1 M KOH. **d)** LSV curves of ZIF-67/CB samples with varied amount of CB, measured in 0.1 M KOH and 1.0 M KOH (inset). **e)** Overpotential values, estimated at the current density of 10 mA cm^{-2} in a 0.1 KOH electrolyte, for the ZIF-67 (50 nm), ZIF-67/CB (50 wt%) and carbon-based catalysts from the published literature. Smaller overpotential value is an indicator for best OER catalyst. Detailed activity values and sample identities are summarised in Table 3.2.

Table 3.2. Comparison of ZIF-derived and cobalt based electrocatalysts (synthesized via carbonization, annealing or acid leaching) for OER.

No.	Samples	Loading [mg cm^{-2}]	Potential@ 10 [mA cm^{-2}]	Electrolyte	Reference
1	Co/PFC	0.13	1.84	0.1 M KOH	[33]
2	Ni/PFC	0.13	1.79	0.1 M KOH	[33]
3	Co_3O_4/MnO_2/PQ-7	0.2	1.78	0.1 M KOH	[34]
4	N-Fe/N/C-CNT	0.6	1.72	0.1 M KOH	[35]
5	S, N-C-CNT	0.6	1.78	0.1 M KOH	[35]
6	Fe-N-C	0.2	1.72	0.1 M KOH	[36]
7	N/Co-doped PCP (ZIF-derived Carbon)	0.36	1.75	0.1 M KOH	[37]
8	CMS/NCNF	0.3	1.73	0.1 M KOH	[38]
9	S/N-Fe	0.8	1.77	0.1 M KOH	[39]
10	ZNDC1000(ZIF-derived Carbon)	0.28	1.72	0.1 M KOH	[27]

11	P-CNS	0.15	1.71	0.1 M KOH	[40]
12	S-CNS	0.15	1.86	0.1 M KOH	[40]
13	Z9-800-250	0.25	1.71	0.1 M KOH	[41]
14	Fe/N-HMSC (FePc)	N/A	1.74	0.1 M KOH	[36]
15	Co-TA-800	0.3	1.69	0.1 M KOH	[42]
16	NCNF-1000	0.1	1.85	0.1 M KOH	[43]
17	CoMnO/C	0.054	1.79	0.1 M KOH	[44]
18	Crumpled graphene/CoO	0.36	1.65	1 M KOH	[45]
19	MAF-X27-OH	0.18	1.69	0.1 M KOH	[19]
20	Co_3O_4	N/A	1.66	1 M KOH	[46]
21	CoO_x-ZIF	N/A	1.54	1 M KOH	[32]
22	Co–N/C 800	0.24	1.74	0.1 M KOH	[47]
23	Co@Co_3O_4/NC-1 (ZIF-derived Carbon)	0.21	1.65	0.1 M KOH	[48]
24	Co_xO_y/C	N/A	1.66	0.1 M KOH	[49]
25	1100-CNS	0.42	1.69	0.1 M KOH	[50]
26	N-GCNT/FeCo-3	0.40	1.73	0.1 M KOH	[51]
27	CMO/S-300	0.3	1.7	0.1 M KOH	[52]
28	Pt/C	N/A	1.9	0.1 M KOH	[32]

29	IrO_2/C	N/A	1.62	0.1 M KOH	[31]
29	ZIF-67	0.28	1.7	0.1 M KOH	This thesis work
30	ZIF-67/CB (50wt%)	0.28	1.66	0.1 M KOH	This thesis work
31	ZIF-67/CB (50wt%)	0.28	1.55	1 M KOH	This thesis work

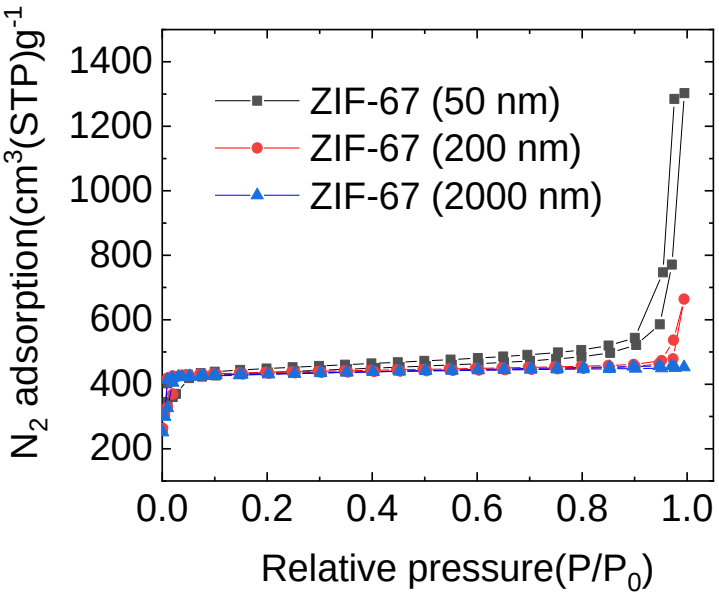

Figure 3.8. Nitrogen adsorption-desorption isotherms of ZIF-67 samples with particle size of 50 nm, 200 nm and 2000 nm. The deduced values for BET specific surface area and pore volume in noted in Table 3.1. The high N_2 adsorption towards high relative pressures are due to the condensation effect in the externally formed macropores between nanoparticles.

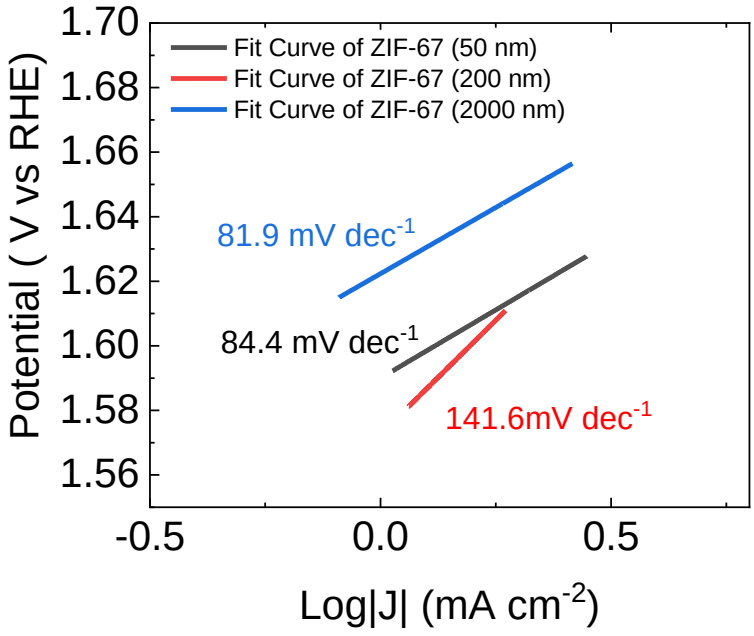

Figure 3.9. Tafel plots (applied potential (RHE) vs log (current density)) of different size of ZIF-67

In addition, it is very interesting to see an emerging oxygen reduction reaction (ORR) activity in the ZIF-67/CB samples (Figure 3.10). Though no ORR activity is observed for both ZIF-67 and CB alone, a continuously improved activity, with prominent current response at further reduced potentials, can be seen for ZIF-67/CB samples with respect to the increased amount of CB. Such activity is also evidenced in CV curves with a characteristic cathodic current peak. There is a continuous decrease in the Tafel slope with increasing the amount of carbon black in ZIF-67/CB sample. These observations clearly suggest that the dual activity for both OER and ORR can be extracted from ZIF-67 sample.

.

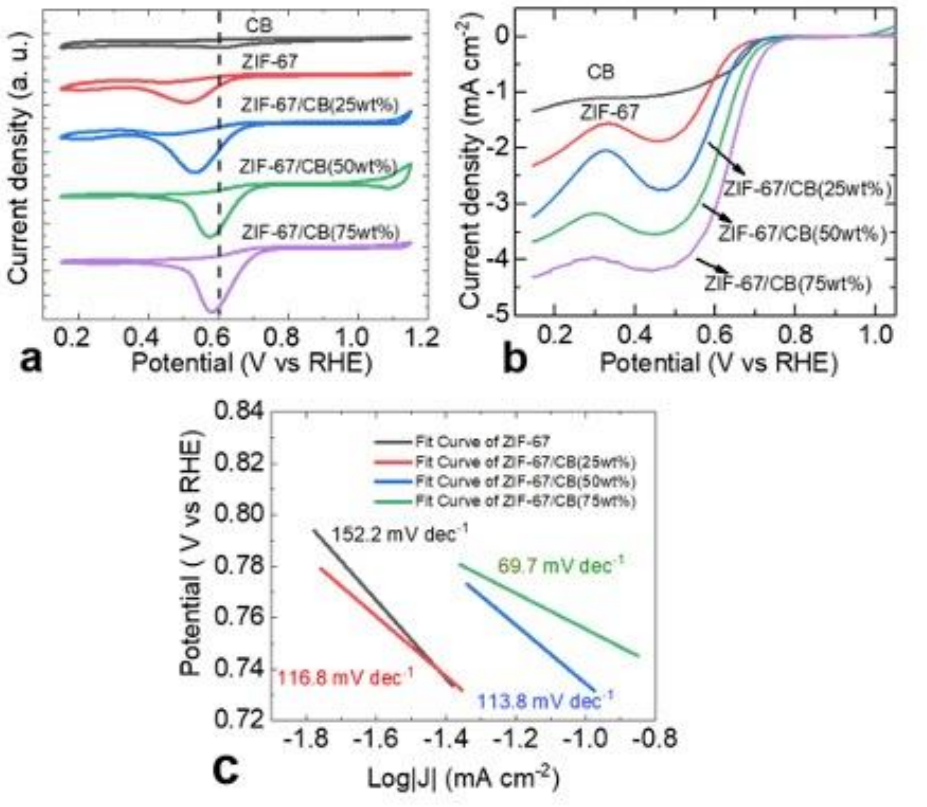

Figure 3.10. Emerging ORR activity in ZIF-67/CB samples: CV curves, LSV curves and Tafel plots (applied potential (RHE) vs log (current density)) for ORR of ZIF-67/CB samples.

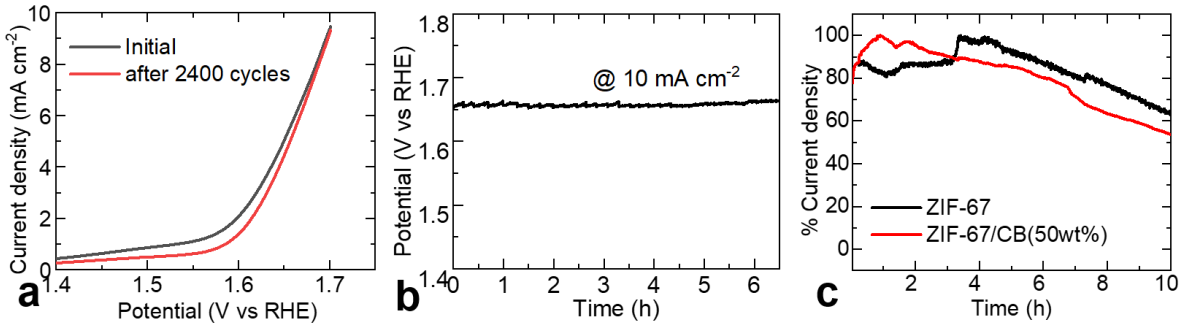

Figure 3.11. OER activity durability of optimised ZIF-67 sample: a) Comparative LSV curves of ZIF-67 deposited on GCE before and after 2400 CV tests, measured for 6 h in a RDE system with 0.1 M KOH. **b)** Chronopotentiometry of ZIF-67 deposited on GCE, measured for 6 h at a current density of 10 mA cm^{-2} in a RDE system at 1600 rpm and with 0.1 M KOH.

The other important parameter, OER durability/stability of the ZIF-67 is investigated by three different methods: chronoamperometry, chronopotentiometry and accelerated CV scans at 100 mV s^{-1} (Figure 3.11). The samples show impressively durable activities over several hours of continuous operation. Here, it is worth noting that the OER stability of ZIF-67 is superior to the many carbonaceous structures. For instance, after 2400 CV cycles, of continuous operation over ~6 hours, the ZIF-67 sample shows negligible drop in the activity (Figure 3.11a). The *V vs t* and *i vs t* data also shows a similar durability (Figure 3.11b-c). Here, it is worth noting that these data is recorded for the samples directly coated onto the GCE and under constant rotation at 1600 rpm. Thus, the partial activity decay in the stability tests may be attributed to the gradual loss of the catalyst on the electrode under rotation.[27,29,30] The catalysts detachment from the GCE surface is often observed. Therefore, further to alleviate this problem and to understand the true activity durability performance, the sample is deposited on to the carbon paper with gas diffusion layer (with a high mass loading of 2 mg cm^{-2}), which has relatively high surface roughness for better surface fixation than on the polished surface of GCE. Figure 3.12 shows the photographs of deposited sample/carbon paper and 3-electrode test cell, as well as SEM micrographs. The LSV data recorded in the 1 M KOH electrolyte while stirring the solution with bar magnet shows a similar performance to their RDE data obtained for ZIF-67/CB(50wt%) (Figure 3.13a). Importantly, sample now not only shows impressively durable OER activity but also exhibit

further improved performance over the time, which increases exponentially for few hours and then stabilize during the 24 h continuous operation (Figure 3.13b). This can be attributed to the increased electrolyte accessibility to the hydrophobic ZIF-67 structure over the time.

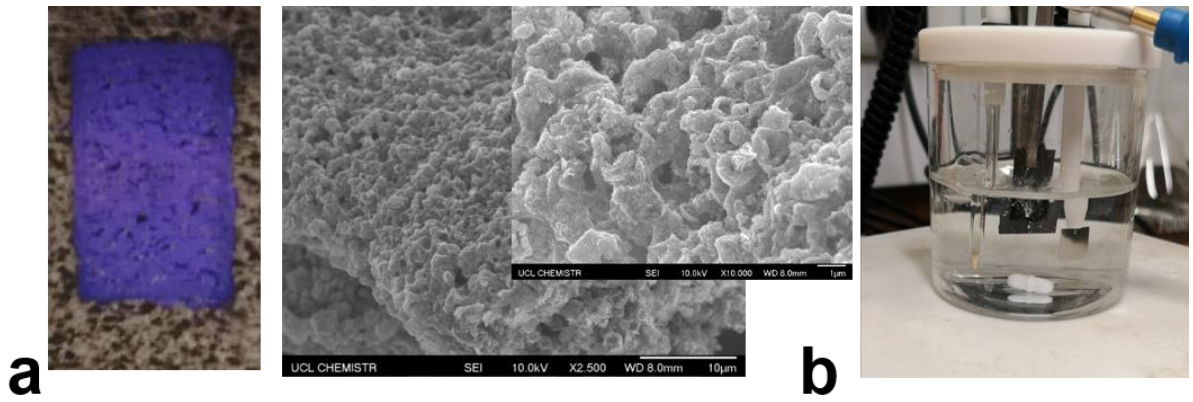

Figure 3.12. (a-b) Photograph, SEM micrographs and 3-electrode test cell for ZIF-67 sample deposited on carbon paper with a loading of 2 mg cm^{-2}.

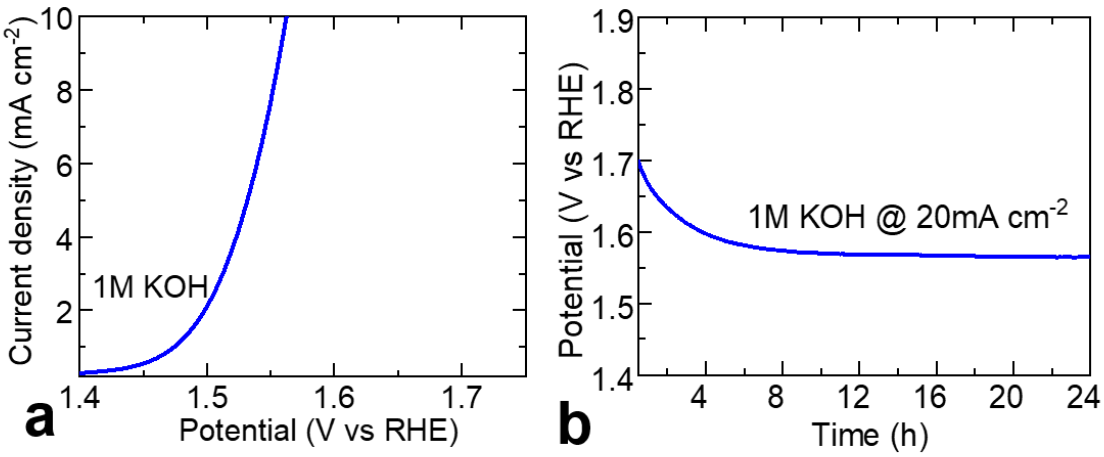

Figure 3.13. (a) LSV curve ZIF-67 sample deposited on carbon paper, measured in 1 M KOH. **(b)** Chronopotentiometry of ZIF-67 sample deposited on carbon paper, measured for 24 h in 1 M KOH, at a current density of 20 mA cm^{-2}.

This trend is also observed in the $Zn_{100-x}Co_x$-ZIF-8 samples (Figure 3.14a). This can be attributed to the increased electrolyte accessibility to the hydrophobic ZIF-67 structure over the time. The FTIR, SEM, XPS and PXRD characterizations of $Zn_{100-x}Co_x$ZIF-8 samples after OER durability tests reveal transformation of ZIFs to active cobalt based oxide/oxyhydroxide nanophase, in a good agreement with the literature reports.[16,53–57] As shown in Figure 3.14b, the FTIR spectra show development of new Co-O vibrational mode (at 530 cm^{-1}) at the expense of Zn/Co-N coordination (at 420 cm^{-1}) in $Zn_{100-x}Co_x$ZIF-8 samples. Similarly, XPS spectra of Co 2p in a parent ZIF-67 sample with two peaks at around 782 eV and 797.7 eV shift to lower binding energy without satellite peaks in the sample used for OER test for 24 h, supporting the formation of cobalt oxide/hydroxide phase (Figure 3.14c).[57–59] XRD profiles and SEM images further indicates the transformation of crystalline ZIF-67 to amorphous phase (Figure 3.14d), in a good agreement with earlier reports of MOFs/ZIFs based OER catalysts (Figure 3.15).[57,60]

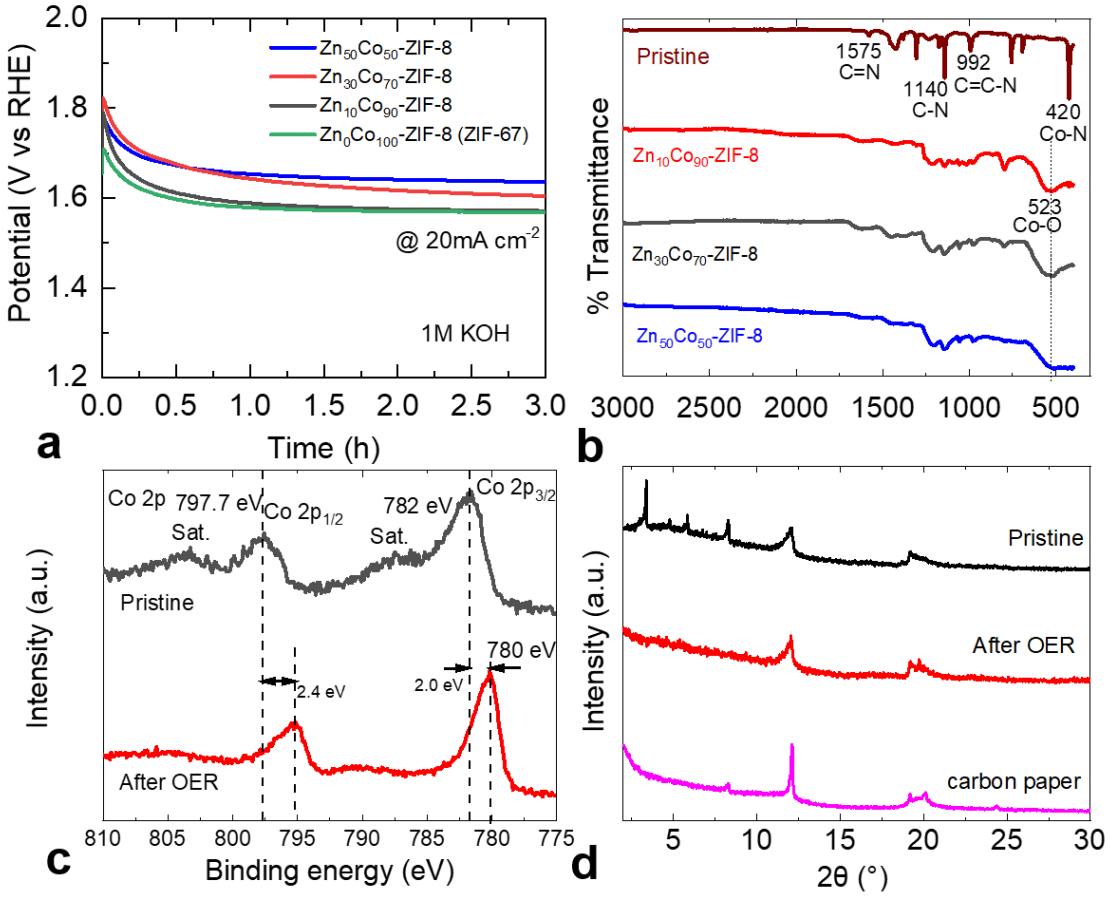

Figure 3.14. (a) Chronopotentiometry of $Zn_{100-x}Co_xZIF-8$ samples deposited on carbon paper, measured for 3 h in 1 M KOH, at a current density of 20 mA cm^{-2}. **(b)** FTIR spectra of $Zn_{100-x}Co_xZIF-8$ after OER test for 3 h on carbon paper. **(c)** XPS Co 2p core level spectra of ZIF-67 before and after OER test for 24 h on carbon paper. **(d)** XRD patterns of ZIF-67 before and after OER test for 24 h on carbon paper.

Overall, such results suggest that ZIF-67 is a promising and inexpensive catalyst, and its activity for OER or ORR or both can be further improved by tailoring framework structure by the strategic design of MOFs/ZIFs. For instance, by introducing macro-microporosity to facilitate rapid migration of reactants and products, sulfone-groups to enhance the wettability, and core-shell and dimensional structures to enhance the surface activity.[54,61]

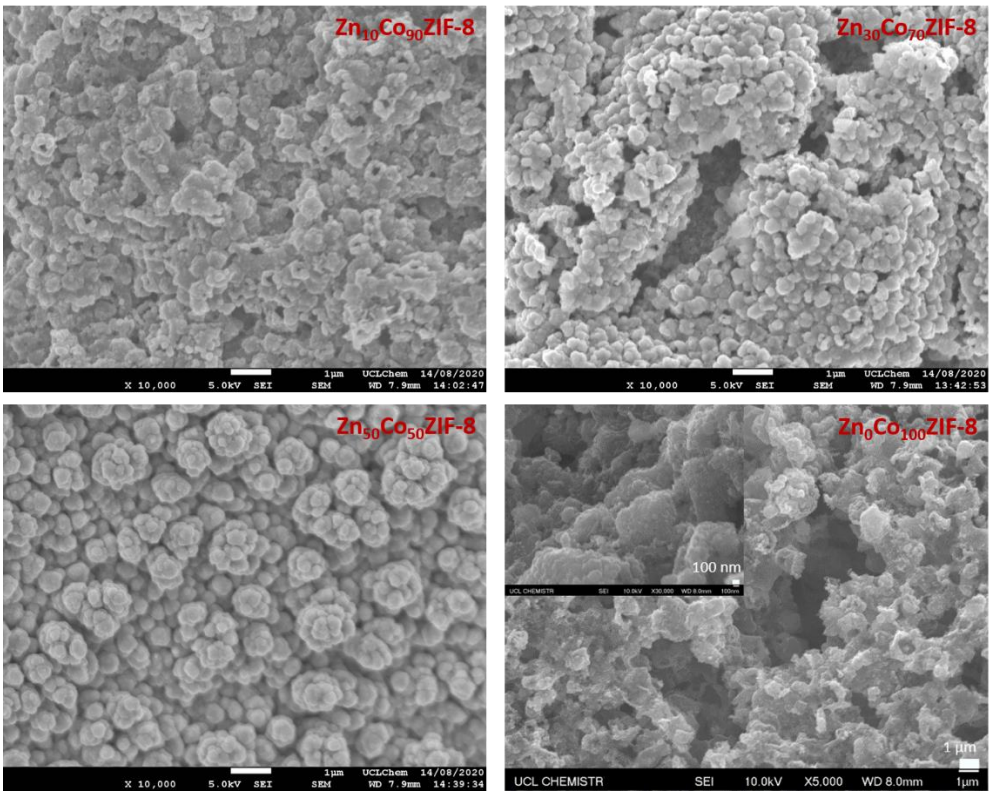

Figure 3.15. SEM images of $Zn_{100-x}Co_xZIF-8$ after OER stability test for 3 h and ZIF-67 after 24 h on carbon paper.

3.4. Conclusion

I have disclosed a highly active and durable OER performance, for the first time, in one of the widely studied MOF structures, ZIF-67 – a cobalt-based prototype of ZIF-8 directly, without carrying any further post-synthesis chemical modification such as oxidation or carbonization at high temperature. Co–N, rather than Zn–N, coordination is responsible for the oxygen catalysis reactions, which is identified by screening a series of bimetallic ZIF samples from ZIF-8 to ZIF-67 with a progressive cobalt substitution for zinc-metal centres. Such activity is enhanced in the optimized ZIF-67 with control over particle size as well as with conducting support. Interesting correlation is observed between OER and particle size of ZIF-67, where the samples of particle size 50 nm and 2000 nm exhibit an overpotential difference of about 50 mV at 10 mA cm^{-2} with a decreased activity trend against increased particle size. Such activities are further improved by the addition of conducting carbon black or depositing on the carbon paper, with a low overpotential of ≈320 mV to achieve a current density of 10 mA cm^{-2} in 1.0 M KOH electrolyte. The samples also exhibit highly durable OER activity over several hours of continuous tests. The OER activity in the optimized ZIF-67 nanoparticles is comparable to the carbonaceous nanostructures, include MOFs/ZIFs derived carbons. The present study provides a straightforward and energy-efficient strategy for designing electrocatalysts, and suggests further improved activities in the tailoring framework structures in terms of dimensionality, pore geometry, and accessible surface with combined macro-micropore channels and hydrophilicity.

3.5 References

[1] S. Dang, Q.-L. Zhu, Q. Xu, *Nat. Rev. Mater.* **2017**, *3*, 17075.

[2] Z. Cai, Z. Wang, J. Kim, Y. Yamauchi, *Adv. Mater.* **2019**, *31*, 1804903.

[3] B. N. Bhadra, A. Vinu, C. Serre, S. H. Jhung, *Mater. Today* **2018**, *25*, 88.

[4] W. Yang, X. Li, Y. Li, R. Zhu, H. Pang, *Adv. Mater.* **2018**, *31*, 1804740.

[5] K. Shen, L. Zhang, X. Chen, L. Liu, D. Zhang, Y. Han, J. Chen, J. Long, R. Luque, Y. Li, B. Chen, *Science.* **2018**, *359*, 206.

[6] M. Rubio-Martinez, C. Avci-Camur, A. W. Thornton, I. Imaz, D. Maspoch, M. R. Hill, *Chem. Soc. Rev.* **2017**, *46*, 3453.

[7] X. Xiao, L. Zou, H. Pang, Q. Xu, *Chem. Soc. Rev.* **2020**, *49*, 301.

[8] W. Liu, R. Yin, X. Xu, L. Zhang, W. Shi, X. Cao, *Adv. Sci.* **2019**, *6*, 1802373.

[9] Z. Xue, Y. Li, Y. Zhang, W. Geng, B. Jia, J. Tang, S. Bao, H.-P. Wang, Y. Fan, Z. Wei, Z. Zhang, Z. Ke, G. Li, C.-Y. Su, *Adv. Energy Mater.* **2018**, *8*, 1801564.

[10] S. Gadipelli, Z. Li, Y. Lu, J. Li, J. Guo, N. T. Skipper, P. R. Shearing, D. J. L. Brett, *Adv. Sci.* **2019**, *6*, 1901517.

[11] G. Srinivas, V. Krungleviciute, Z. X. Guo, T. Yildirim, *Energy Environ. Sci.* **2014**, *7*, 335.

[12] S. Gadipelli, W. Travis, W. Zhou, Z. Guo, *Energy Environ. Sci.* **2014**, *7*, 2232.

[13] Y. Xue, S. Zheng, H. Xue, H. Pang, *J. Mater. Chem. A* **2019**, *7*, 7301.

[14] Z. Wan, D. Yang, J. Chen, J. Tian, T. T. Isimjan, X. Yang, *ACS Appl. Nano Mater.* **2019**, *2*, 6334.

[15] W. Chen, Y. Zhang, G. Chen, Y. Zhou, X. Xiang, K. K. Ostrikov, *ACS Sustain. Chem. Eng.* **2019**, *7*, 8255.

[16] Q. Zha, W. Xu, X. Li, Y. Ni, *Dalt. Trans.* **2019**, *48*, 12127.

[17] D. Su, X. Zhang, A. Wu, H. Yan, Z. Liu, L. Wang, C. Tian, H. Fu, *NPG Asia Mater.* **2019**, *11*, 78.

[18] N. Y. Huang, J. Q. Shen, Z. M. Ye, W. X. Zhang, P. Q. Liao, X. M. Chen, *Chem. Sci.* **2019**, *10*, 9859.

[19] X.-F. Lu, P.-Q. Liao, J.-W. Wang, J.-X. Wu, X.-W. Chen, C.-T. He, J.-P. Zhang, G.-R. Li, X.-M. Chen, *J. Am. Chem. Soc.* **2016**, *138*, 8336.

[20] F.-L. Li, Q. Shao, X. Huang, J.-P. Lang, *Angew. Chem. Int. Ed.* **2018**, *57*, 1888.

[21] J. Teng, M. Chen, Y. Xie, D. Wang, J. J. Jiang, G. Li, H. P. Wang, Y. Fan, Z. W. Wei, C. Y. Su, *Chem. Mater.* **2018**, *30*, 6458.

[22] Q. Qian, Y. Li, Y. Liu, L. Yu, G. Zhang, *Adv. Mater.* **2019**, *31*, 1901139.

[23] F. L. Li, P. Wang, X. Huang, D. J. Young, H. F. Wang, P. Braunstein, J. P. Lang, *Angew. Chem. Int. Ed.* **2019**, *58*, 7051.

[24] L. Zhuang, L. Ge, H. Liu, Z. Jiang, Y. Jia, Z. Li, D. Yang, R. K. Hocking, M. Li, L. Zhang, X. Wang, X. Yao, Z. Zhu, *Angew. Chem. Int. Ed.* **2019**, *58*, 13565.

[25] T. Liu, P. Li, N. Yao, T. Kong, G. Cheng, S. Chen, W. Luo, *Adv. Mater.* **2019**, *31*,

1806672.

[26] T. Wen, Y. Zheng, J. Zhang, K. Davey, S. Qiao, *Adv. Sci.* **2019**, *6*, 1801920.

[27] S. Gadipelli, Z. Li, T. Zhao, Y. Yang, T. Yildirim, Z. Guo, *J. Mater. Chem. A* **2017**, *5*, 24686.

[28] K. S. Park, Z. Ni, A. P. Cote, J. Y. Choi, R. Huang, F. J. Uribe-Romo, H. K. Chae, M. O'Keeffe, O. M. Yaghi, *Proc. Natl. Acad. Sci.* **2006**, *103*, 10186.

[29] S. Gadipelli, T. Zhao, S. A. Shevlin, Z. Guo, *Energy Environ. Sci.* **2016**, *9*, 1661.

[30] T. Zhao, S. Gadipelli, G. He, M. J. Ward, D. Do, P. Zhang, Z. Guo, *ChemSusChem* **2018**, *11*, 1295.

[31] X. L. Wang, L. Z. Dong, M. Qiao, Y. J. Tang, J. Liu, Y. Li, S. L. Li, J. X. Su, Y. Q. Lan, *Angew. Chem. Int. Ed.* **2018**, *57*, 9660.

[32] S. Dou, C.-L. Dong, Z. Hu, Y.-C. Huang, J. Chen, L. Tao, D. Yan, D. Chen, S. Shen, S. Chou, S. Wang, *Adv. Funct. Mater.* **2017**, *27*, 1702546.

[33] G. Fu, Y. Chen, Z. Cui, Y. Li, W. Zhou, S. Xin, Y. Tang, J. B. Goodenough, *Nano Lett.* **2016**, *16*, 6516.

[34] D. Micheroni, G. Lan, W. Lin, *J. Am. Chem. Soc.* **2018**, *140*, 15591.

[35] P. Chen, T. Zhou, L. Xing, K. Xu, Y. Tong, H. Xie, L. Zhang, W. Yan, W. Chu, C. Wu, Y. Xie, *Angew. Chem. Int. Ed.* **2017**, *56*, 610.

[36] S. Dresp, F. Luo, R. Schmack, S. Kühl, M. Gliech, P. Strasser, *Energy Environ. Sci.* **2016**, *9*, 2020.

[37] Y. Hou, Z. Wen, S. Cui, S. Ci, S. Mao, J. Chen, *Adv. Funct. Mater.* **2015**, *25*, 872.

[38] Y. Wang, J. Fu, Y. Zhang, M. Li, F. M. Hassan, G. Li, Z. Chen, *Nanoscale* **2017**, *9*, 15865.

[39] N. Ranjbar Sahraie, J. P. Paraknowitsch, C. Göbel, A. Thomas, P. Strasser, *J. Am. Chem. Soc.* **2014**, *136*, 14486.

[40] J. Lee, A. Sami, S. S. Shinde, S.-U. Lee, D.-H. Kim, C.-H. Lee, *ACS Nano* **2016**, *11*, 347.

[41] W. Chaikittisilp, N. L. Torad, C. Li, M. Imura, N. Suzuki, S. Ishihara, K. Ariga, Y. Yamauchi, *Chem. - A Eur. J.* **2014**, *20*, 4217.

[42] J. Wei, Y. Liang, Y. Hu, B. Kong, J. Zhang, Q. Gu, Y. Tong, X. Wang, S. P. Jiang, H. Wang, *Angew. Chem. Int. Ed.* **2016**, *55*, 12470.

[43] Q. Liu, Y. Wang, L. Dai, J. Yao, *Adv. Mater.* **2016**, *28*, 3000.

[44] C. Li, X. Han, F. Cheng, Y. Hu, C. Chen, J. Chen, *Nat. Commun.* **2015**, *6*, 7345.

[45] S. Mao, Z. Wen, T. Huang, Y. Hou, J. Chen, *Energy Environ. Sci.* **2014**, *7*, 609.

[46] T. Grewe, X. Deng, C. Weidenthaler, F. Schüth, H. Tüysüz, *Chem. Mater.* **2013**, *25*, 4926.

[47] W. Hu, Q. Wang, S. Wu, Y. Huang, *J. Mater. Chem. A* **2016**, *4*, 16920.

[48] A. Aijaz, J. Masa, C. Rösler, W. Xia, P. Weide, A. J. R. Botz, R. A. Fischer, W. Schuhmann, M. Muhler, *Angew. Chem. Int. Ed.* **2016**, *55*, 4087.

[49] J. Masa, W. Xia, I. Sinev, A. Zhao, Z. Sun, S. Grützke, P. Weide, M. Muhler, W. Schuhmann, *Angew. Chem. Int. Ed.* **2014**, *53*, 8508.

[50] Z. Pei, H. Li, Y. Huang, Q. Xue, Y. Huang, M. Zhu, Z. Wang, C. Zhi, *Energy Environ. Sci.* **2017**, *10*, 742.

[51] C.-Y. Su, H. Cheng, W. Li, Z.-Q. Liu, N. Li, Z. Hou, F.-Q. Bai, H.-X. Zhang, T.-Y. Ma, *Adv. Energy Mater.* **2017**, *7*, 1602420.

[52] S. Peng, X. Han, L. Li, S. Chou, D. Ji, H. Huang, Y. Du, J. Liu, S. Ramakrishna, *Adv. Energy Mater.* **2018**, *8*, 1800612.

[53] J. Cao, K. Wang, J. Chen, C. Lei, B. Yang, Z. Li, L. Lei, Y. Hou, K. Ostrikov, *Nano-Micro Lett.* **2019**, *11*, 1.

[54] J. Cao, C. Lei, J. Yang, X. Cheng, Z. Li, B. Yang, X. Zhang, L. Lei, Y. Hou, K. Ostrikov, *J. Mater. Chem. A* **2018**, *6*, 18877.

[55] J. Cao, C. Lei, B. Yang, Z. Li, L. Lei, Y. Hou, X. Feng, *Batter. Supercaps* **2019**, *2*, 348.

[56] P. M. Usov, C. Mcdonnell-worth, F. Zhou, D. R. Macfarlane, D. M. D. Alessandro, *Electrochim. Acta* **2015**, *153*, 433.

[57] W. Zheng, M. Liu, L. Y. S. Lee, *ACS Catal.* **2020**, *10*, 81.

[58] Y. Liang, J. Wei, Y. X. Hu, X. F. Chen, J. Zhang, X. Y. Zhang, S. P. Jiang, S. W. Tao, H. T. Wang, *Nanoscale* **2017**, *9*, 5323.

[59] J. Xu, P. Gao, T. S. Zhao, *Energy Environ. Sci.* **2012**, *5*, 5333.

[60] G. Chen, J. Zhang, F. Wang, L. Wang, Z. Liao, E. Zschech, K. Müllen, X. Feng, *Chem. – A Eur. J.* **2018**, *24*, 18413.

[61] X. Li, C. Wang, H. Xue, H. Pang, Q. Xu, *Coord. Chem. Rev.* **2020**, *422*, 213468.

Chapter 4. Direct utilisation of zeolitic imidazolate framework – ZIF-67 as bifunctional oxygen electrocatalyst for zinc-air batteries

4.1 Introduction

In this chapter, a new strategy to extract the catalytic activity directly from as-received ZIFs is developed. It is worth noting that no further chemical manipulation of ZIFs is carried out as many approaches reported in the literature perform processes such as plasma treatment,[1] metal cations (bi- and tri-metal) surface decoration,[2] and calcination or carbonization at elevated temperatures.[2,3,12,4–11] In previous chapter, we have demonstrated ZIF-67 derived catalyst exhibited very good OER catalytic but not good on ORR side. The electrochemical tests for the initial evaluation of OER and ORR activities are conducted using a rotating disk three-electrode (RDE) in alkaline electrolyte. The OER activity of ZIF-8(Zn) is gradually enhanced towards ZIF-67(Co) with the substitution of cobalt metal centres for zinc. Further to this, ZIF-67 crystallites of varied sizes, between 50 nm to 2000 nm, are designed and explored to achieve the best catalytic performance (discussed in chapter 3). Building upon this understanding, a highly enhanced OER activity is obtained from the ZIF/carbon black composite (ZIF-67/CB). In this regard, a new strategy that only take one step to extract the electrocatalytic activity from as-received ZIFs is developed. We are not sacrificing the pristine MOF/ZIF structures, instead the directly utilizing of two readily materials could avoid extensive chemical process and thus accelerate large scale commercial implementation for zinc air battery. The bifunctional catalyst, with a small overpotential of 0.87 V, for both OER and ORR is designed by utilising ZIF-67 and commercial Pt/CB (ZIF-67@Pt/CB). Moreover, ZIF-67 based catalysts exhibit stable OER and ORR activities for several hours. More interesting is that this ZIF-67@Pt/CB composite shows enhanced stability for ORR - in a 20 h continuous operation the sample retains ≈85% of its initial activity compared to ≈50% for Pt/CB reference. These OER and ORR activities of the ZIF-67@Pt/CB are further supported by demonstration in a zinc-air battery (ZAB) functional device. It readily delivers a high open circuit voltage of 1.42 V, maintained for 20 h, and a peak power density of ≥150 mW cm^{-2}. Interestingly, ZAB also shows stable long-life cyclic performance for over 50 h. This performance is superior to many reports of carbonaceous nanostructures with metal-/metal-oxide and non-metallic dopants and Pt/CB.

4.2 Experimental Section

4.2.1 Synthesis

ZIF-67@Pt/CB: samples were prepared with 1:1 and 2:1 mass ratio of ZIF-67 and Pt/CB, respectively for **ZIF-67@Pt/CB and ZIF-67@Pt/CB-2** in a solution with Nafion binder via sonication to obtain a homogeneous ink. The as-synthesized samples were then used for electrochemical test directly after drop casting on to the electrode supports either glassy carbon disc or gas diffusion layer carbon paper. The **ZIF-8@Pt/CB** in 1:1 mass ratio of ZIF-8 and Pt/CB was also prepared under similar procedure.

4.2.2 Structure and porosity characterizations

Powder X-ray diffraction patterns (PXRD) were collected by Stoe Stadi-P, Mo–K-alpha. Fourier-transform infrared (FTIR) data was obtained by Bruker ALPHA FTIR Spectrometer (Platinum-ATR) with background correction. X-ray photoemission spectroscopy (XPS, on Al–K-alpha, Thermo Scientific) data and scanning electron microscopy (SEM, on JSM6700, Jeol) measurements were carried out on the samples supported on a carbon tape. The porosity by N_2, and CO_2 adsorption-desorption isotherms were measured at 77 K and 298 K, respectively, on a Quantachrome Autosorb-iQC. All the samples were degassed at 180 ℃ overnight under a dynamic vacuum prior to the actual gas adsorption measurements. The specific surface area was measured from the 77 K N_2 isotherm in a relative pressure range between 0.01 and 0.2, according to the Brunauer–Emmett–Teller (BET) method. The pore volume was obtained from the adsorption volume at relative pressure of 0.95.

4.2.3 Electrochemical tests

All the electrochemical catalytic activity of the samples were reported using a potentiostation (Autolab, Metrohm PGSTAT302N) with a rotating-disk three-electrode (RDE) cell configuration

composed of a glassy carbon rotating disk with active material as working electrode, and (1 × 1) cm^2 Pt and Ag/AgCl/saturated KCl as counter and reference electrode, respectively. All the measurements were carried out in O_2-saturated alkaline (0.1 M KOH and 1.0 M KOH) electrolyte at room temperature. The catalyst loading was fixed at ~0.28 mg cm^{-2} on a 3 mm diameter (or area of 0.0707 cm^2) glassy carbon electrode (GCE). The catalyst was prepared as follows; 2 mg of sample was dispersed in a total 500 µl solution consisting 482 µl of deionized water plus 18 µl of Nafion (5% solution) under sonication. The sonication was carried out for up to an hour to get uniform catalyst dispersion of ink. Of this 5 µl was micropipetted and dropped on to a GCE followed by drying at <60 ℃ in an oven prior to the electrochemical tests. The cyclic voltammetry (CV) and linear sweep voltammetry (LSV) curves were recorded with voltage sweeping at 10 mV s^{-1} in the potential range of +0.2 V to +1.0 V in case of OER and in the range of +0.2 V to −0.8 V in case of ORR. OER durability tests by chronoamperometric (*I vs t*) were carried out at a fixed potential of +1.65 V (vs RHE), and the response current was recorded against time. In chronopotentiometry (*V vs t*), the response potential was recorded against time at a fixed current density of 10 mA cm^{-2}. All of the OER LSV curves were recorded at constant rpm of 1600. ORR LSV curves were recorded at discrete rotation rates between 400 rpm and 2000 rpm. All the reported current densities were estimated by normalizing the actual current response to the electrode area of GCE. The following relation is used for potential representation V (vs RHE) = $E_{Ag/AgCl}$ + 0.197 + 0.059 × pH. The overpotential is reported according to the relation; V = V_{RHE} − 1.23 V.

4.2.4 Fabrication of Zn-air batteries

Two-electrode zinc-air battery liquid cells were fabricated within the commercial battery cell cases. Briefly, air-cathodes were prepared by loading catalysts on carbon paper *via* a drop-casting method, the material active area is maintained around 0.25 cm^{-2}. As-synthesized catalysts were mixed with the Nafion solution (0.1 % w/w in ethanol) to form the ink with a concentration of 4 mg mL^{-1}. For comparison, Pt/CB and Pt/CB+IrO_2 catalysts were also prepared by mixing commercial Pt/CB (mass loading of 0.5 mg cm^{-2}). Zinc plate with 3 mm thickness, polished by 10% hydrochloric acid and DI water in an ultrasonicator for 3 min each, and used as the anode. 6.0 M KOH with 0.2 M $Zn(CH_3COO)_2.2H_2O$ was prepared as the electrolyte to ensure the reversible redox reaction at

the anode. The galvanostatic discharge-charge tests were performed for 300 cycles with 10 min for each cycle (5 min for each discharge/charge) at the current density of 5 mA cm^{-2}.

The power density (P in mW cm^{-2}) is estimated based on the equation: $P = U \times J$, where U is a battery voltage (V), and J is a current density (mA cm^{-2}).

4.3 Results and discussion

As shown in Figure 4.1, it is very interesting to see an emerging ORR activity in the ZIF-67/CB samples. ZIF-67 shows a promising OER activity and reflects in an encouraging level of open circuit voltage (OCV) value and low voltage value for charge step during the cycling process (Figure 4.2). With the additional conducting carbon black, the OER activity can be improved for the battery performance. However, no ORR activity is observed for both ZIF-67 and CB alone compared with the reference Pt/CB catalyst.

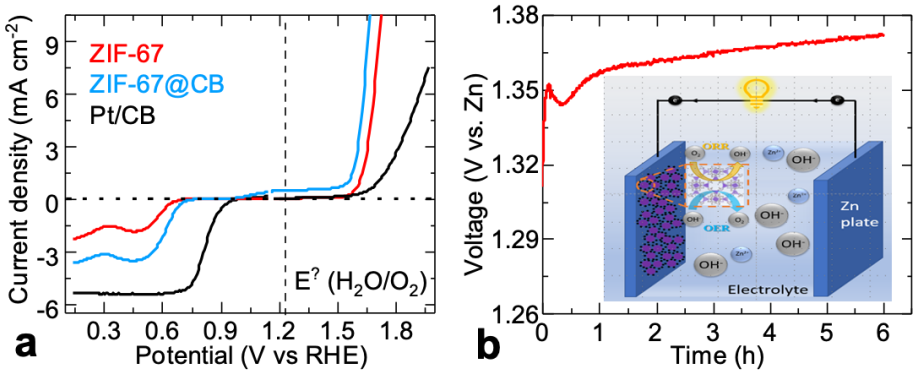

Figure 4.1. (a) Combined ORR and OER LSV curves of ZIF-67, ZIF-67@CB and Pt/CB. All the measurements were carried out in a 0.1 M KOH electrolyte in three electrode configurations with rotating disk electrode method at 1600 rpm. b) OCV of a zinc-air battery with ZIF-67 catalyst deposited on GDLCP as cathode, with inset for schematic representation of a zinc-air battery cell.

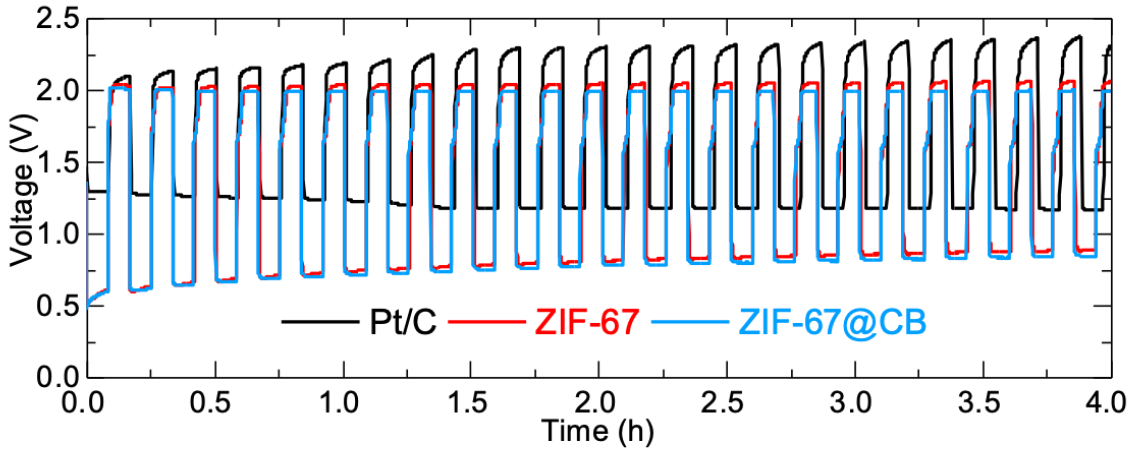

Figure 4.2. Charge-discharge cyclic tests of batteries made with different catalysts deposited on GDLCP as cathode and operated at a fixed current density of 5 mA cm^{-2}.

These observations clearly suggest that the bifunctional activity for both OER and ORR can be extracted from ZIF-67 if combined with the CB and ORR activity component; for example, Pt(20%)/CB (Pt/CB, a commercial ORR standard reference material). Thus, a highly efficient bifunctional catalyst is prepared by simply mixing in solution and then casting on the carbon paper at room temperature (Figure 4.3a). Then ZIF-67@Pt/CB and ZIF-67@Pt/CB-2 are denoted for the different mass ratios 1:1 and 2:1 of ZIF-67 and Pt/CB. In all cases, the catalysts are first uniformly loaded onto a hydrophobic carbon fibre paper electrode at a loading equivalent to 0.5 mg cm^{-2}. The devices are then tested in a static ambient atmosphere, without oxygen/air purging, to simulate the real working conditions of the battery. Before this, rotating disc electrode method is used to examine all the activity performance for the catalyst materials. It is anticipated that the addition of Pt/CB can boost both the ORR and OER performance of ZIF-67 by combining its high ORR activity as well as good electron transfer ability of CB (Figure 4.3b). It should be noted that although Pt/CB exhibits poor activity for OER, the composite, ZIF-67@Pt/CB(50 wt%) sample retains its OER activity. Samples of given composition (50 wt% of Pt/CB loading) with the highest OER activity also show promising ORR performance, thus exhibiting bifunctional activity (Figure 4.3b). For comparison, the activity of ZIF-8@Pt/CB(50wt%) is also studied. The ZIF-8 based sample is less active for both ORR and OER. The reaction pathway electron transfer number (*n*) in ZIF-67@Pt/CB is analysed by the Koutecky–Levich (K–L) plots and Tafel plots yields same 4 electron pathway ORR activity as Pt/C for direct conversion of O^2 to OH^- (Figure 4.3c, 4.4 and

4.5).[13] However, this *n* is about 2.6 in the ZIF-8@Pt/CB sample indicating the intermediates formation. The best ORR activity and durability of ZIF-67@Pt/CB, with respect to the ZIF-8@Pt/CB, further suggesting the interfacial coupling between Pt and Co metal centres in the ZIF-67 system. As expected, the ORR activity of ZIF-67@Pt/CB samples is enhanced with respect to the amount of the Pt/CB in the composite. The half-wave potential and the onset potential of the ZIF-67@Pt/CB(50 wt%) are now ≈0.79 V and ≈0.93 V (vs RHE). These values are comparable to the ≈0.82 V and ≈0.96 V in Pt/CB (Figure 4.3e).

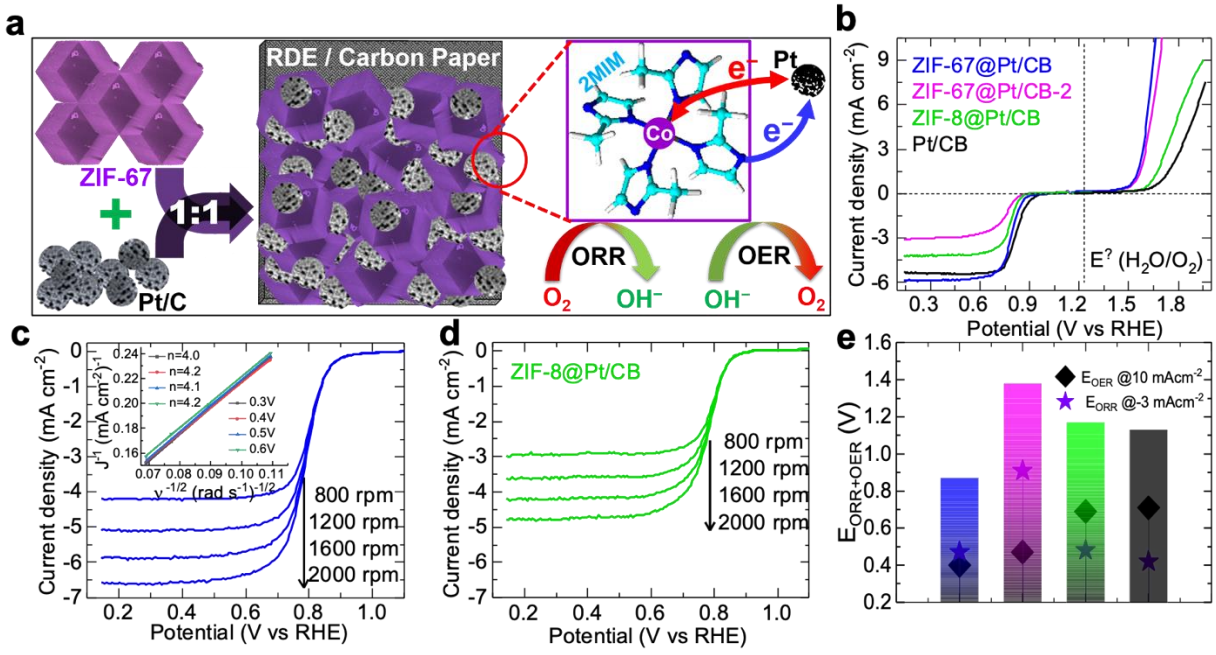

Figure 4.3. (a) Preparation of catalysts via facile solution method at room temperature with insights for local framework structure/surface platinum interaction. **(b)** Combined ORR and OER LSV curves. **(c-d)** ORR LSV curves at different rotating speeds, with inset for Koutechy-Levich plot linear fittings. **(e)** Bar graph showing the potential difference for bifunctional activity with respective ORR and OER overpotential values recorded at -3 and 10 mA cm^{-2}, respectively. Same colour code applies for the samples in all subpanel graphs.

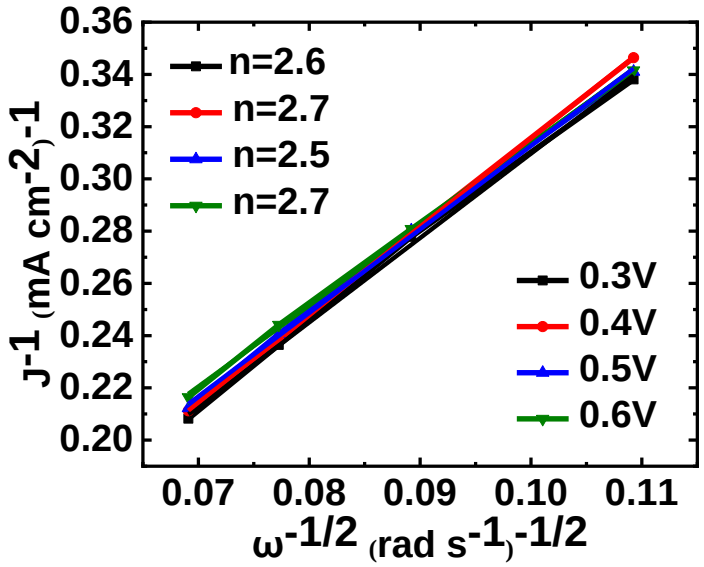

Figure 4.4. Koutechy-Levich plot linear fittings for ZIF-8@Pt/CB.

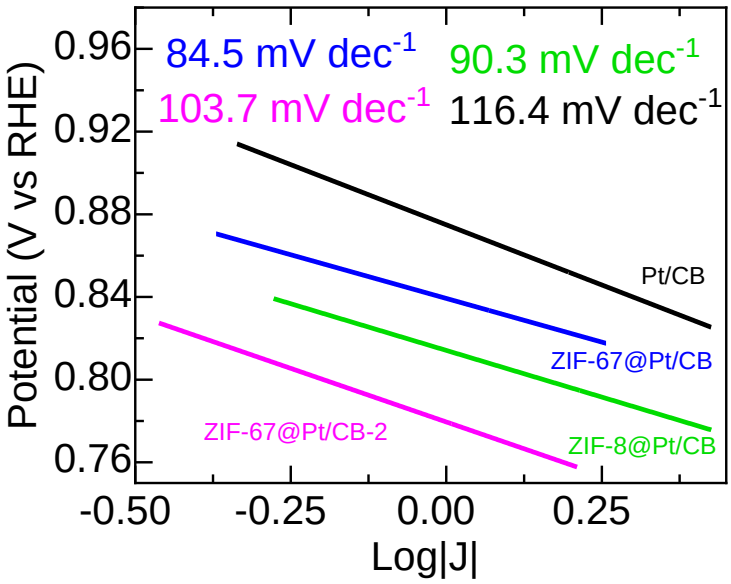

Figure 4.5. ORR Tafel plots (applied potential (RHE) vs log (current density)) of ZIF-67@Pt/CB, ZIF-67@Pt/CB-2, ZIF-8@Pt/CB, and Pt/CB samples.

The double layer capacitance (Cdl) of ZIF-67@Pt/CB is comparable to that of Pt/CB, whereas ZIF-67@Pt/CB-2 and ZIF-8@Pt/CB samples show reduced values (Figure 4.6). Electrochemical impedance spectroscopy indicates an efficient electrolyte diffusion within the ZIF-67@ Pt/CB-based electrode structure (Figure 4.7).

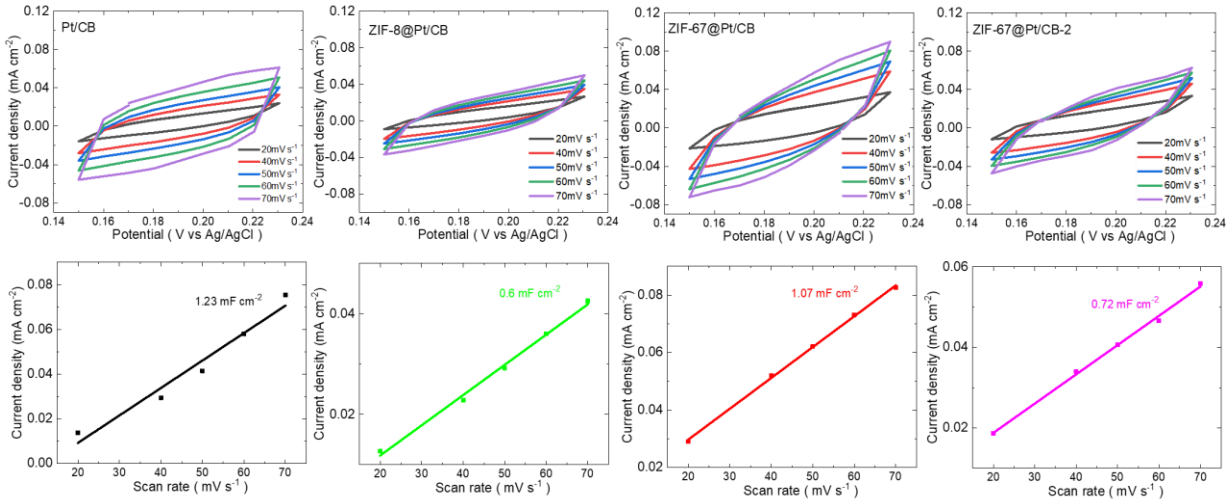

Figure 4.6. CV cycles of Pt/CB, ZIF-8@Pt/CB, ZIF-67@Pt/CB and ZIF-67@Pt/CB-2 samples at different scan rates of 20, 40, 50, 60 and 70 mV s^{-1} and corresponded double-layer capacitance (Cdl) calculation, obtained from the slope of linear plot of maximum current density against scan rate.

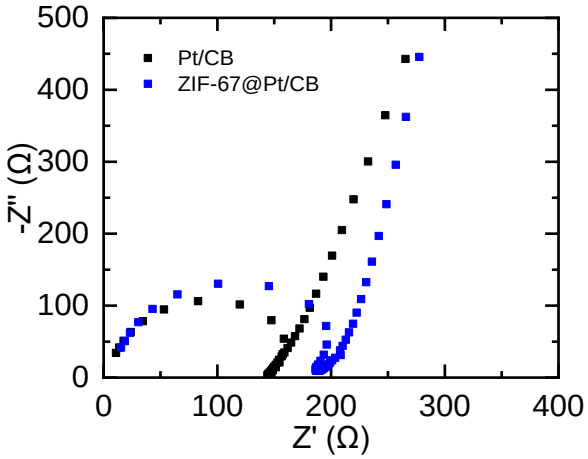

Figure 4.7. Electrochemical impedance spectroscopy (EIS) of Pt/CB and ZIF-67@Pt/CB.

Overall, the best bifunctional activity is exhibited by ZIF-67@Pt/CB(50wt%). For this, the overpotentials are calculated from the current density responses; − 3 mA cm^{-2} and 10 mA cm^{-2} for ORR and OER respectively and are summarised in (Figure 4.8 and Table 4.1). Smaller overpotential is indicative of efficient bifunctional activity. Accordingly, the ZIF-67@Pt/CB(50wt%) sample exhibits an overpotential of ≈0.87 V. This value is comparably smaller than ≈1.13 V associated with Pt/CB, and ZIF-8@Pt/CB(50wt%) with ≈1.17 V, and to the many other carbonaceous or metal-/metal-oxide based bifunctional catalysts reported in the literature (Table 4.1). In many cases, the post-synthesis modification of ZIFs and MOFs involve annealing, anchoring metal/metal oxide on the MOFs or etching the surface to create more active sites. This requires high-temperature, making it energy intensive to produce carbon nanostructures containing metal/metal-oxide nanoparticles.[3–6,9,10,14–16]

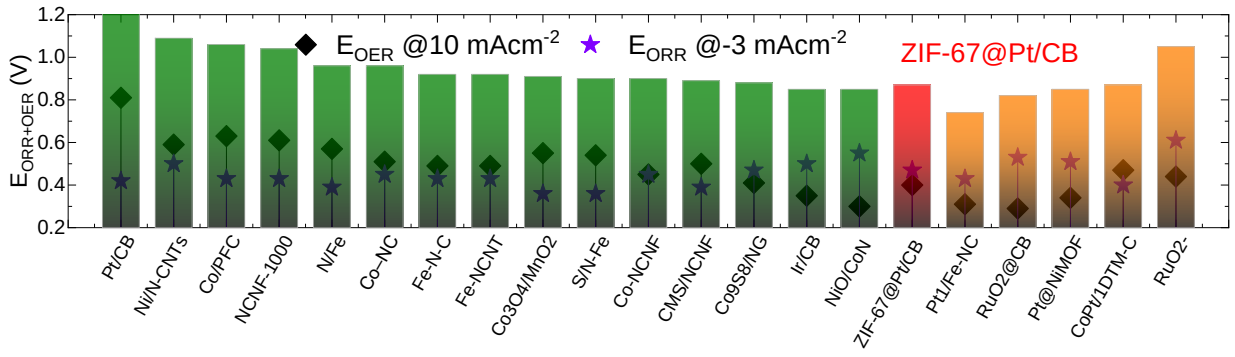

Figure 4.8. Bar graph showing the comparative potential difference values for the bifunctional activity (i.e., potential difference between -3 and 10 mA cm^{-2} for ORR and OER, respectively) of the samples in this study and carbon based samples from the literature. (orange color bar data represents noble metal contained data reported from literature). Note that smaller potential difference value is an indicator for efficient bifunctional activity. Full details related to the activity values are summarized in Table 4.1.

Table 4.1. ORR/OER activity comparison of electrocatalysts (synthesized via carbonization, annealing or acid leaching) for bifunctional oxygen electrocatalysts. The overpotentials are calculated from the current density responses; −3 mA cm^{-2} (E^{-3}) and 10 mA cm^{-2} (E^{10}) for ORR and OER respectively. Overpotential ($\Delta E = E^{10} - E^{-3}$) is indicative of efficient bifunctional activity. Note that smaller the overpotential value is best for bifunctional activity.

Sample	ORR (E^{-3})	OER (E^{10})	ΔE	Reference
Co_3O_4/MnO_2/PQ-7	0.87	1.78	0.91	[17]
CoNC-CNF-1000	0.78	1.68	0.9	[18]
S/N-Fe	0.87	1.77	0.9	[19]
N/Fe	0.84	1.8	0.96	[19]
Fe-N-C	0.80	1.72	0.92	[20]
NCNF-1000	0.80	1.84	1.04	[21]
Co_3O_4-NP/N-rGO	0.75	1.61(1 M KOH)	0.86	[22]
B,N-carbon	0.80	1.57	0.77	[23]
N-carbon	0.74	1.65	0.91	[23]
Co–N/C 800	0.78	1.74	0.96	[24]
NiO/CoN PINWs	0.68	1.53	0.85	[25]
CMS/NCNF	0.84	1.73	0.89	[26]
N-Fe/N/C-CNT	0.80	1.72	0.92	[27]
Ir/C (20 wt%)	0.73	1.58	0.85	[20]
Ni/N-CNTs	0.73	1.82	1.09	[28]
Co/PFC	0.8	1.86	1.06	[29]
N-Co_9S_8/G	0.76	1.64	0.88	[30]
Pt/CB (20 wt%)	0.82	1.94	1.13	My thesis work
ZIF-8@Pt/CB(50wt%)	0.75	1.92	1.17	My thesis work
ZIF-67@Pt/CB(50wt%)	0.79	1.66	0.87	My thesis work

It is interesting to note that the structure of ZIF-67@Pt/CB still retains relatively high porous structure with a specific surface area of 1200 m^2 g^{-1}. The Fourier transform infrared (FTIR) spectra, CO_2 uptake and scanning electron microscopy (SEM) images indicated well crystalline structure of ZIF-67 (Figure 4.9 and Table 4.2). The transmission electron microscopy (TEM) images further shows homogeneous distribution of ZIF-67 and Pt/CB which is evidenced by energy-dispersive X-ray spectroscopy (EDX) mapping images of ZIF-67@Pt/CB (Figure 4.10 and 4.11). XPS analysis also show clear chemical interaction between Pt/CB and ZIF-67, which is also reported in the literature. [12,13,31] Particularly, the Lewis basic N- (nitrogen) groups of framework imidazolate in the ZIFs or other related frameworks act as electron donors and thus facilitate strong surface interaction and fine dispersion of nanoparticles. For example, as shown below in Figure 4.12, Pt 4f as well as Co 2p3/2 and N 1s peaks shift to higher binding energy compared to the initial Pt/CB and ZIF-67. This indicates the very clear interfacial interactions between ZIF-67 and Pt/CB. This indicates the Pt nanoparticles at ZIF-67 leads to definite change in the chemical nature of Pt and ZIF-67 with the modified Co-N, Co-Pt and Pt-N interactions.

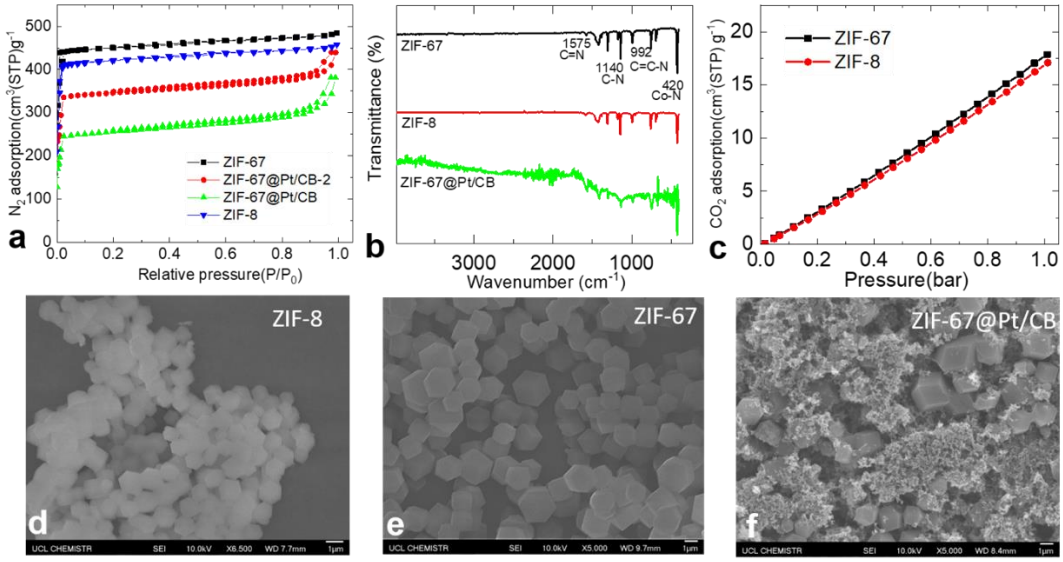

Figure 4.9. (a) Nitrogen adsorption-desorption isotherms. (**b)** FTIR spectra. (**c)** CO_2 adsorption isotherms. (**d-f)** SEM images of as synthesized ZIF-8, ZIF-67 and physically mixed ZIF-67@Pt/CB composites.

Table 4.2. BET specific surface area (SSA) and pore volume (V_p) of as synthesized ZIF-8, ZIF-67 and physically mixed ZIF-67@Pt/CB composites.

Sample	SSA ($m^2\ g^{-1}$)	V_p ($cm^3\ g^{-1}$)
ZIF-8	1633	0.707
ZIF-67	1730	0.740
ZIF-67@Pt/CB-2	1660	0.679
ZIF-67@Pt/CB	1200	0.589

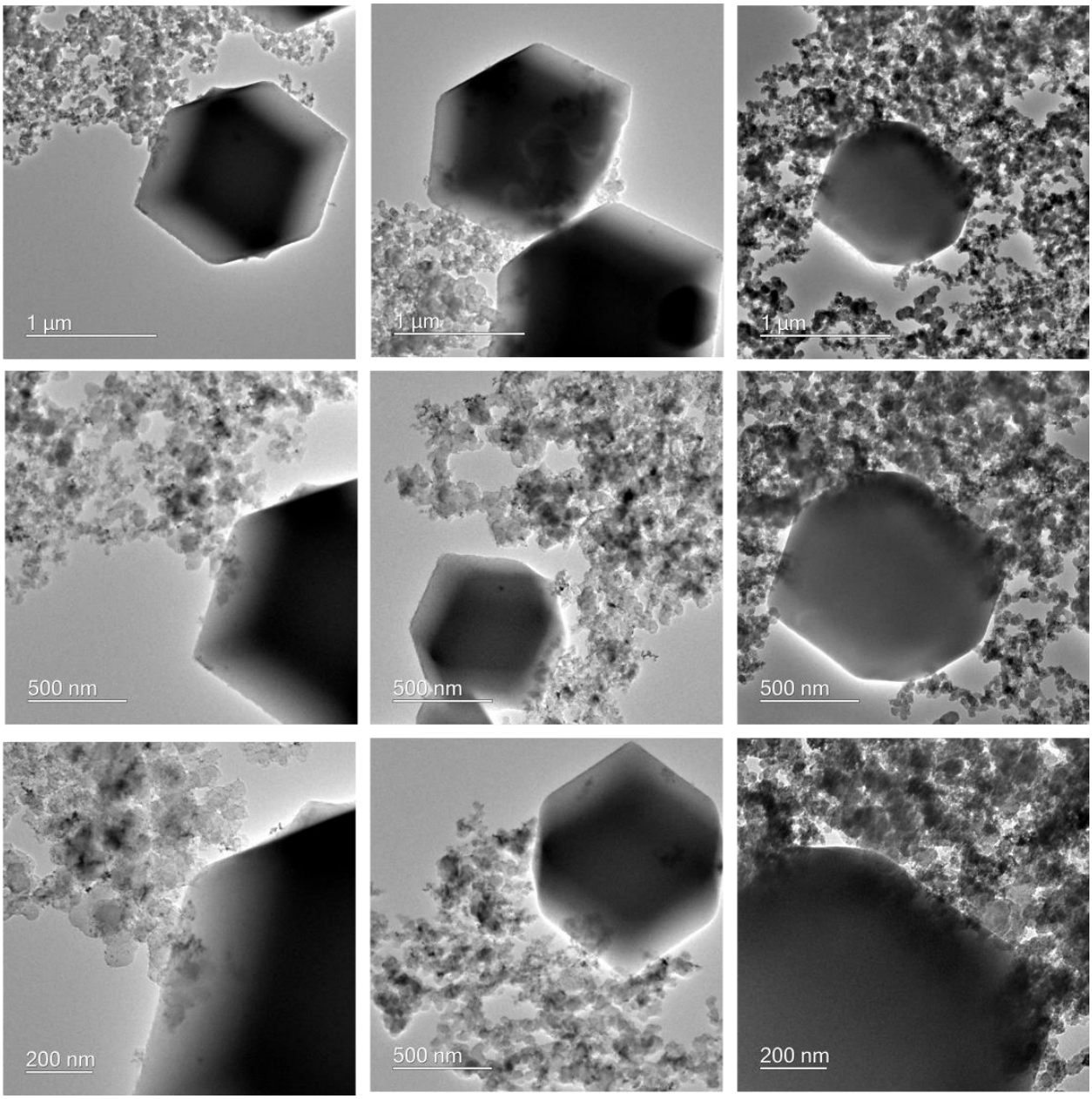

Figure 4.10. TEM images of physically mixed ZIF-67@Pt/CB composites.

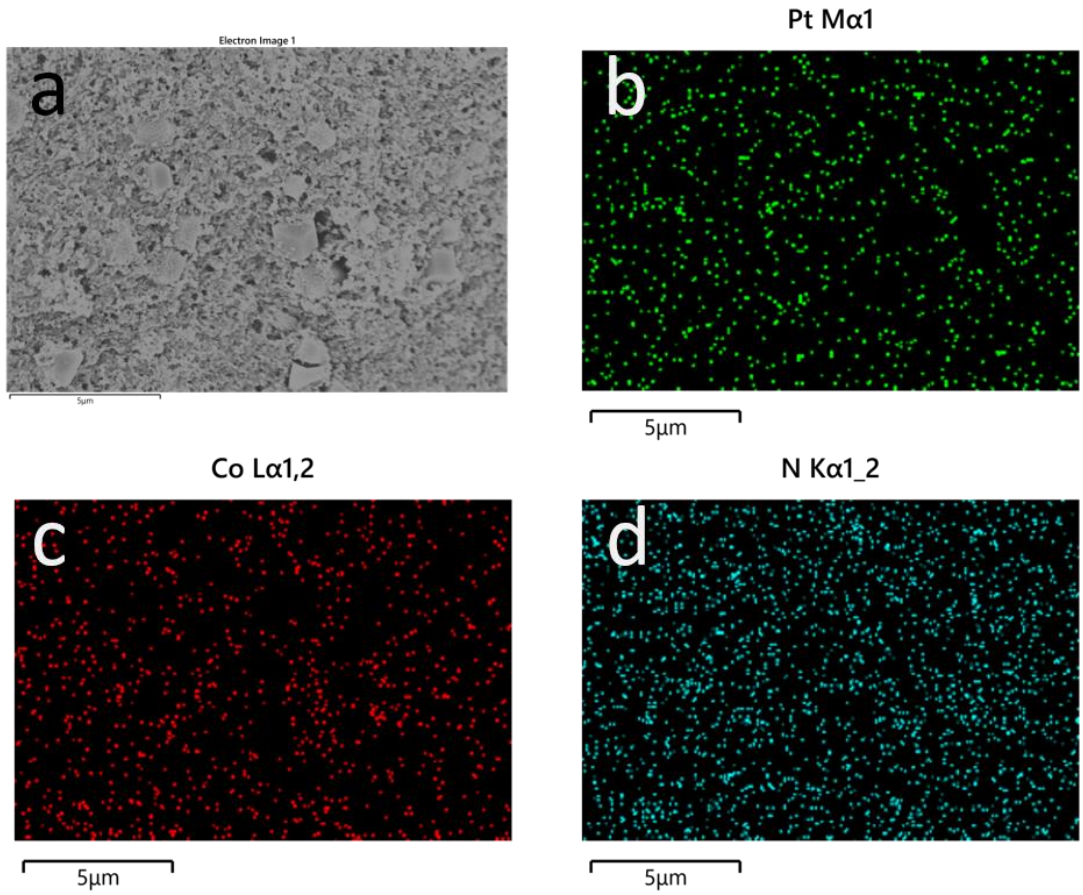

Figure 4.11. EDX mapping images of ZIF-67@Pt/CB.

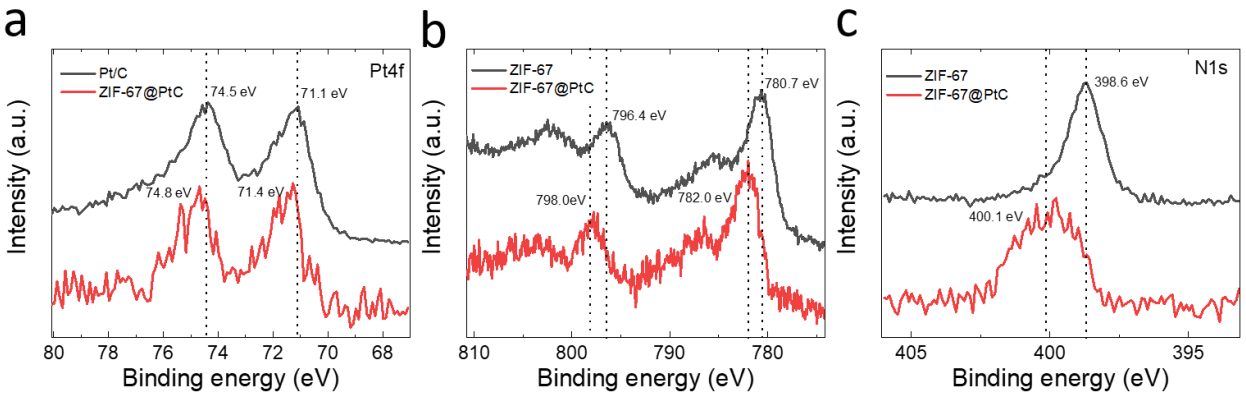

Figure 4.12. Comparative XPS profiles of Pt/CB, ZIF-67 and ZIF-67@Pt/CB **(a)** Pt 4f spectra of ZIF-67@Pt/CB(50wt%) and Pt/CB. **(b)** Co 2p spectra of ZIF-67@Pt/CB(50wt%) and ZIF-67. **(c)** N 1s spectra of ZIF-67@Pt/CB(50wt%) and ZIF-67.

Based on the impressive bifunctional activity performance for oxygen catalysis and stability of the ZIF-67@Pt/CB, as a proof-of-concept, a rechargeable zinc-air battery (ZAB) is made by using ZIF-67@Pt/CB loaded on carbon paper as an air cathode, and polished zinc foil as an anode, in 0.2 M zinc acetate containing 6 M KOH electrolyte. For comparison, the reference ZABs are also assembled using a commercial Pt/CB and a mixture of Pt/CB and IrO_2 catalysts in a 1:1 mass ratio (Pt/CB+IrO_2). In all cases, the catalyst are first uniformly loaded onto a hydrophobic carbon fibre paper electrode at a loading equivalent to 0.5 mg cm^{-2} (see Experimental details). The devices are then tested in a static ambient atmosphere, without oxygen/air purging, to simulate the real working conditions of the battery. As shown in Figure 4.13a, the ZIF based ZAB delivers an impressive open circuit voltage of 1.42 V, approaching the theoretical value (1.65 V) of the Zn–air system, and is maintained for a measured period of 20 h.[31] The galvanodynamic charge/discharge polarization and corresponding discharge power density curves of ZIF and Pt/CB based ZABs are comparatively showed in Figure 4.13b. A large current density of 100 mA cm^{-2} at a voltage of 1.0 V and maximum power density of >150 mW cm^{-2} at 250 mA cm^{-2} is delivered in the ZIF-based battery. These values are comparatively higher with respect to the Pt/CB based catalyst, which exhibits around 50 mA cm^{-2} and 90 mW cm^{-2}, respectively. Considering the charge-discharge curves of the ZIF based battery, a light emitting diode (LED) is illuminated by connecting two batteries in series (Figure 4.13c). The device durability under galvanostatic charge-discharge cyclic tests is assessed by operating at a constant current density of 5 mA cm^{-2}. As shown in Figure 4.13d, the ZAB can operate with a small voltage window (i.e., the sum of discharge and charge voltage) of ≤0.8 V, initially. This gives a round-trip efficiency of 64.7%, indicating a more efficient rechargeability (Figure 4.13e). It is interesting to note that the ZIF based battery can cycle with stable discharge and charge platforms at 1.18 V and 1.98 V, respectively, and remains stable in the extended cyclic tests. For a measured period of 50 h (for 300 cycles), the device shows a slight increase of roundtrip voltage window to 0.9 V after 45 h operation. Whereas, the Pt/CB electrode quickly deteriorates and the voltage window increases from 0.92 V to 1.24 V after just 25 cycles, indicating the poor rechargeable properties. The Pt/CB+IrO_2 catalyst also shows an increased roundtrip voltage to 1.01 V within 150 cycles. Note that the OER is a more difficult reaction, with a higher reaction barrier.[44] As shown in Figure 4.3b, the ZIF-67@Pt/CB(50wt%) is one of the best performing bifunctional catalysts with substantially improved stability. It is worth noting here that the ZAB is operated at ambient air rather than pure

O_2. The slight voltage loss/marginal decay of discharge overpotential can also be attributed to the degradation of the zinc anode or by passivation from undesirable side reactions (e.g., $Zn + 2H_2O \rightarrow Zn(OH)_2 + H_2\uparrow$) and oxidation-induced degradation of the electrode. The superior performance of the ZIF-based catalyst may be facilitated by enhanced mass transport from the high porosity and macroporous structure, formed in the external surface of the ZIF-67 nanoparticle assembly, especially at large discharge currents where O_2 consumption is high. The ZIF-catalyst also performs comparatively well compared to many precious-metal-free carbon-based catalysts (Table 4.3).

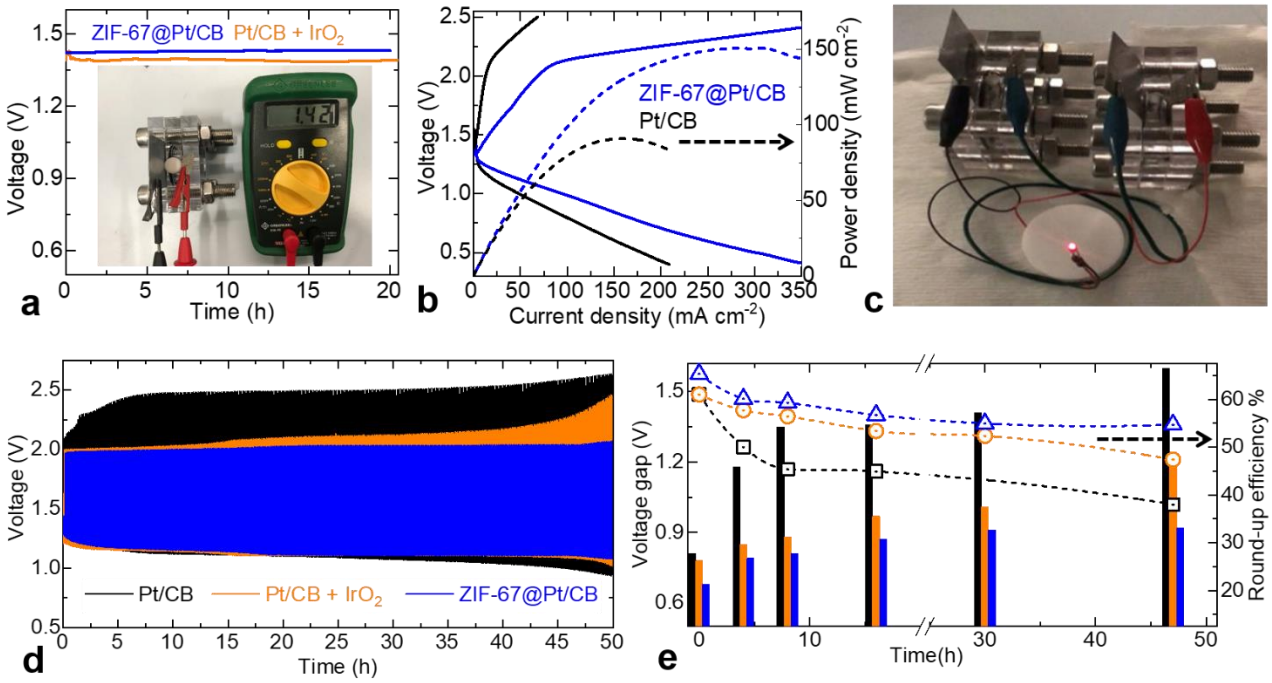

Figure 4.13. (a) OCV, recorded for 20 h, with inset photograph of assembled battery test cell. (**b)** Charge-discharge polarization curves and corresponding discharge power density curves. (**c)** Photograph showing the illuminating LED from two ZIF based batteries connected in a series. (**d)** Long-life charge-discharge cyclic tests of the batteries with different catalysts, operated at a fixed current density of 5 mA cm^{-2} (10 min for each cycle). (**e)** Same color code applies for the samples in all subpanel graphs.

Figure 4.14 compares the power density with ZIF-67@Pt/CB(50wt%) and other carbonaceous catalysts, reported in recent years.[2,10–12,31–33] ZIF combined with platinum-carbon black exhibit competitive power density among the carbon-based catalysts. Clearly**,** ZIF-67@Pt/CB(50wt%) in this study surpasses the activity reported from most of the MOF-derived and other carbon-based materials.[10,33–40] As reported in the literature, Co-SAs@NC (SAs refers to single atoms) produced by pyrolysis of bimetallic Co/Zn-ZIFs at 900 °C followed by further acid washing to remove the metal aggregates could show a peak power density of about 105.0 mW cm^{-2}.[41] Co_3O_4@N-CNMAs/CC sample also exhibits the much lower peak power density of around 75 mW cm^{-2} synthesized via multistep-precursor design, such as growing MOF-on-MOF on carbon cloth (CC), i.e., 3D ZIF-67 on 2D ZIF-L at CC followed by two-step process of carbonization and oxidation.[12] $Fe_{0.5}Co_{0.5}O_x$/NrGO formed by growing MOFs on reduced graphene oxide in an extended synthesis process, involving significant salt ($KMnO_4$) and acid (H_2SO_4) consumption and washing followed by heat treatment could yield a peak power density of 86 mW cm^{-2}.[42] Moreover, Co@BNCNTs produced by pyrolysis at high temperature (700-1000) °C and then washing by H_2SO_4 and KOH, showed a peak power density of 90 mW cm^{-2}.[43] In another instance, NDGs-800 obtained by combing C_3N_4 sheets with GO solution under hydrothermal condition for 12 h and then freeze-dried for 48 h, followed by carbonization at high temperature again only delivered a peak power density of 115.0 mW cm^{-2}.[34] Thus, overall the results suggest that ZIF-67 is a promising and inexpensive catalyst for the dual ORR and OER and applicable in rechargeable metal-air batteries. Such an impressive performance difference is attributed to a better OER activity for the ZIF-based catalyst relative to Pt/CB, as demonstrated in Figures 4.3b and 4.3c. Note that the OER is a more difficult reaction, with a higher reaction barrier.[44] the very poor OER activity of Pt/CB means it needs a high voltage for charging during battery cycling. This ultimately results in side reactions, such as oxidation of the carbon electrode (carbon corrosion), which will have a detrimental effect on the ORR activity.[45–50] Thus, upon repeated cycling reactions will become more sluggish due to the increased resistance and dissolution of oxidized carbon in the Pt/CB air electrode. For these reasons, the highly dual-active OER and ORR catalyst, ZIF-67@Pt/CB based ZAB operated at a smaller voltage window shows long cyclic durability at higher current densities of 10 and 20 mA cm^{-2} for 100 and 70 h, respectively (Figure 4.15 and 4.16). It further shows excellent discharge profiles at various current densities from 2 mA cm^{-2} to 20 $mAcm^{-2}$ (Figure 4.17). The ZIF-catalyst

also performs comparatively well compared to many precious-metal-free carbon-based catalysts (Table 4.3 and 4.4).

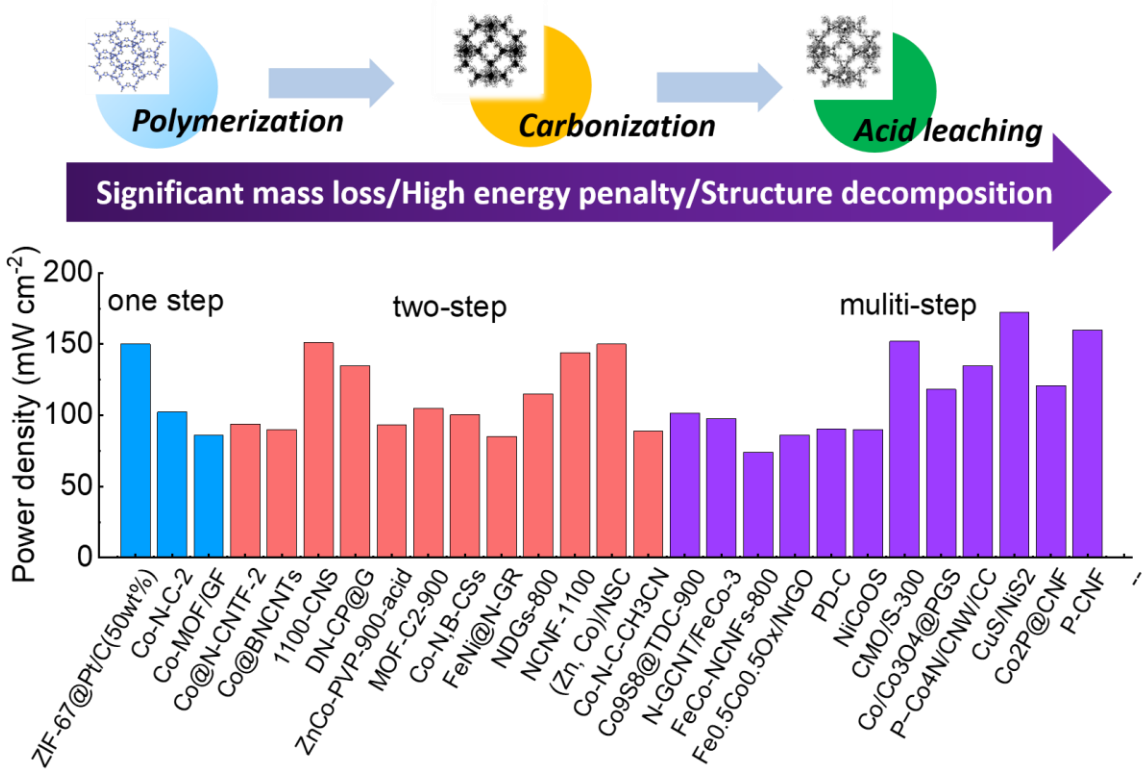

Figure 4.14. Bar graph showing the comparative power density values of the samples in this study and the representative samples from the literature. Full details related to the samples and activity values are summarized in the Table 4.3 and 4.4. Here, it is worth noting that ZIF-67@Pt/CB sample reported in this study show comparative or even better performance in terms of peak power delivery among the other carbonaceous samples prepared under extensive chemical treatment reported in the literature. The one-step, two-step and multi-step in the graph indicates the subsequent post-synthesis chemical modification/treatment, e.g. calcination/carbonization (two-step), and followed by acid etching of template/metal aggregates and reheat treatment or activation or vapor phase doping etc. (multi-step) of as produced precursor structure (one-step). For instance ZIF-67 directly used in this study without further chemical treatment falls in the one-step category. Then it's or other MOF or coordinated polymer based structure carbonized samples falls under two-step category. A further extended chemical treatment over carbonized products falls under multi-step category of the samples.

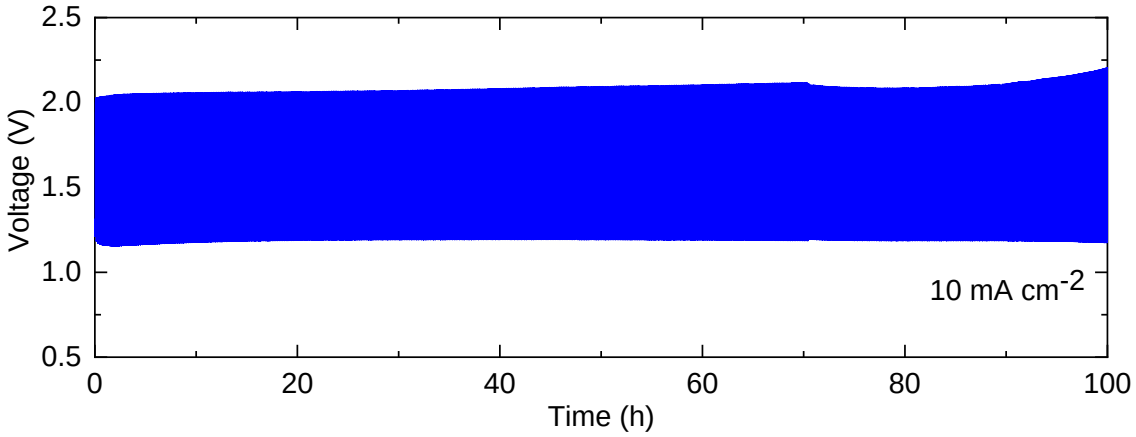

Figure 4.15. Long-life charge-discharge cyclic test ZIF-67@Pt/CB based battery for 100 h at 10 mA cm^{-2}.

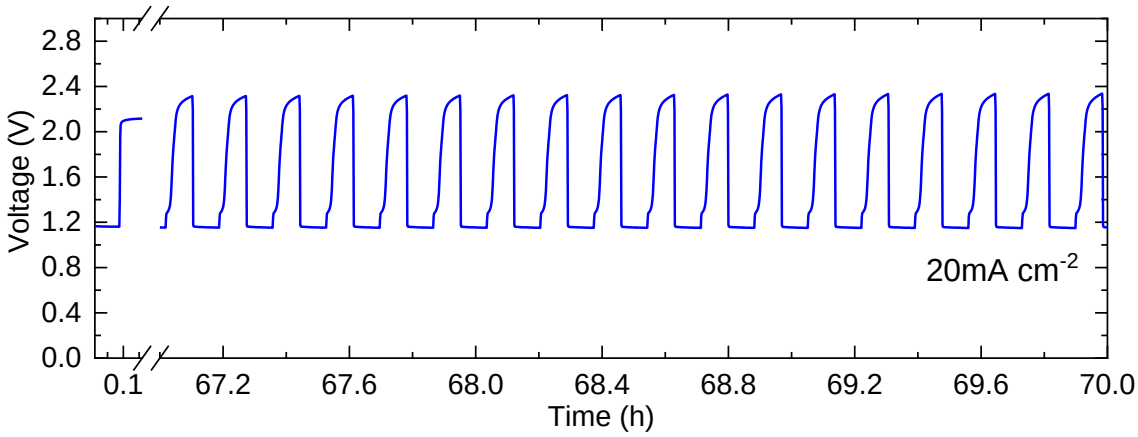

Figure 4.16. Long-life charge-discharge cyclic test ZIF-67@Pt/CB based battery for 70 h at 20 mA cm^{-2}.

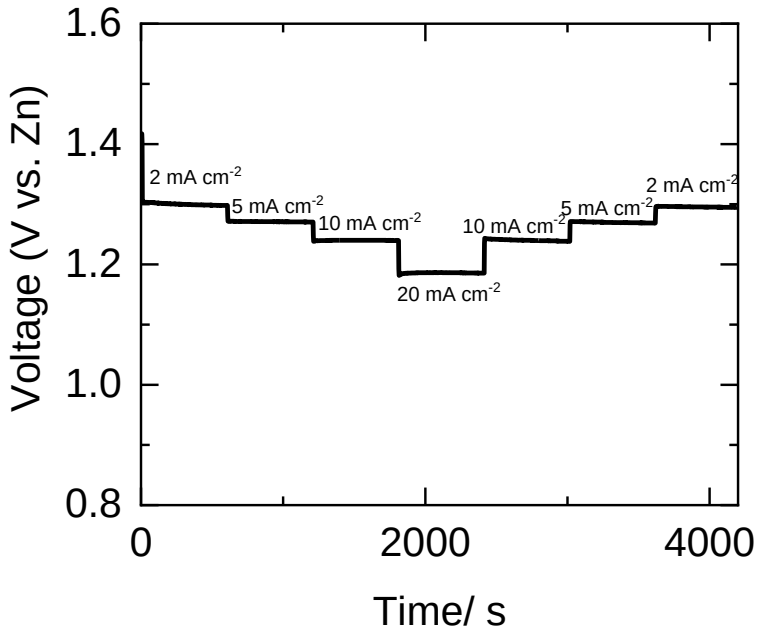

Figure 4.17. Discharge curve of ZIF-67@Pt/CB at different rate current density between 2 mA cm^{-2} and 20 mA cm^{-2} shows a negligible change in the performance.

Table 4.3. Summary of various families of catalyst materials and their performance studied at specified conditions when in rechargeable zinc-air battery.

No.	Sample	Mass loading (mg cm^{-2})	Peak power density (mW cm^{-2})	Battery performance	Reference
1	Co@N-CNTF-2	1	94	Voltage gap is 0.86 V, and it remains at 0.93 V after 100 cycles of continuous operation	[51]
2	Co-N-C-2	5	102.3	After 12 h testing, voltage gap has increased 24%	[52]

3	N-GCNT/FeCo-3	2	97.8	After 9 h testing, slight increase of 10%	[53]
4	FeCo-NCNFs-800	1	74	Initial voltage gap from 0.88 V to 0.99 V, elevated relatively by 11% after cycling for 2500 min.	[54]
5	Co@NPC-H	-	-	After 220 min test, the initial potential gap increased from 0.77 V to 0.90 V	[55]
6	Co@BNCNTs	3.11	90	Voltage gap of 0.96 V over a duration of 65 h.	[56]
7	Co–CNT/PC	0.5	-	After 100 cycles (10min/cycle), as the potential attenuations of the discharge and charge potential are both lower than 10%	[57]
8	1100-CNS	2	151	Initial charge/discharge voltage gap of 0.77 V, performance loss with the voltage gap increased by 85 mV after 300 cycles (55 h)	[58]
9	Co-MOF	10	86.2	Voltage gap ~ 1 V for 70 h at a constant	[59]

				charge discharge current density of 6 mA cm^{-2}	
10	DN-CP@G	7	135	30 mV voltage gap increased after 250 cycles	[60]
11	$Fe_{0.5}Co_{0.5}O_x$/NrGO	-	86	Increased from 0.79 V at the first cycle to 0.89 V at the 60th cycle	[42]
12	PD-C	1	90.6	OCP stabile for 24000 s	[35]
13	NiCoOS	-	90	Stably cycled over 170 h	[61]
14	ZnCo-PVP-900-acid	1	93.4	The peak power density of 93.4 mW cm^{-2} at 0.87 V	[62]
15	MOF-C2-900	0.5	105	No significant potential drop for 40 h at 5 and 10 mA cm^{-2}	[63]
16	Co-N,B-CSs	0.5	100.4	After 128 cycles test (14 h) loss voltage gap of 0.2 V	[64]
17	FeNi@N-GR	2	85	120 cycles for 40 h	[65]
18	NDGs-800	1	115.2	Voltage gap is 0.76 V, remains stable after 78h	[43]
19	CMO/S-300	-	152	After 120 cycles voltage gap of 0.67 V loss with a small	[66]

				increase in the voltage gap by 0.13 V	
20	Co/Co_3O_4@PGS	0.9	118.2	Voltage gap from 0.91 V to 0.96 V for over 750 cycles	[67]
21	CuS/NiS_2	2	172.4	voltage gap of 0.57 V after 500 continuous cycles (about 83 h)	[68]
22	P−Co_4N/CNW/CC	-	135	voltage gap of 0.84 V cycling for 408 cycles (136 h)	[69]
23	NCNF-1100	2	144	10 min/cycle for 500 cycles voltage gap increased ~0.13 V	[21]
24	(Zn, Co)/NSC	5	150	discharged for 22 h at a current density of 5 mA cm^{-2}	[70]
25	Mn/Fe-HIB-MOFs	0.5	195	10 min/cycle for 5400 cycles	[71]
26	PS-CNF P-CNF	-	231 160	600 discharge/charge cycles conducted over a 120 h period with the constant current density of 2 mA cm^{-2}	[72]
27	Co_2P@CNF	-	121	0.66 V for the 1st cycle and 0.69 V for the 210th cycle	[36]

28	Co-N-C-CH_3CN	-	88.9	cycled over 3500 min without visible voltage losses	[73]
29	ZIF-67@Pt/CB	0.5	150	Voltage gap < 0.7 V	This thesis work

Table 4.4. Summary of ZIF-derived materials and their performance studied at specified conditions when in rechargeable zinc-air battery.

No.	Sample	Mass loading (mg cm^{-2})	Peak power density (mW cm^{-2})	Battery performance	Reference
1	ZIF-L-D-Co3O4/CC	-	75	voltage gap between charge and discharge about 0.83 V	[12]
2	GNCNTs-4	1	253	remains a voltage gap from 0.76 V at first cycle	[74]
3	Co- SAs@NC	1.75	105.3	Voltage gap about 0.81V at the beginning	[11]
4	FeNiCo@NC-P	-	112	voltage gap of ≈0.84 V in the first 70 h	[75]
5	Co-N-C-2	5	102.3	Voltage gap increased 24% after 12h	[52]
6	Cu@Fe-N-C	1	92	-	[76]
7	Co-NC@LDH	3	107.8	potential gap from 0.89 V to 0.99 V for over 100 h	[77]

8	ZIF-67@Pt/CB	0.5	150	Voltage gap <0.7 V	This thesis work

In addition, the superior ORR and OER durability of catalysts also contribute to the cyclic stability of the zinc air battery as shown in Figure 4.18a. In order to understand such impressive activity and durability in performance, the ZIF-67@Pt/CB sample used for ORR durability test is further examined by SEM, TEM, XRD, FTIR and XPS (Figure 4.18, 4.19, 4.20 and 4.21). The SEM images before and after ORR durability test, for 20 h, show a partial decomposition of the ZIF-67 structure (Figure 4.18c-d and 4.21). TEM micrographs evidence development of a sheet-like morphology at the expense of ZIF-67 polyhedron structure (Figure 4.18e-f). XRD profiles show the transformation of crystalline ZIF-67 to an amorphous phase (Figure 4.19). FTIR spectra further confirm the ZIF-67 framework collapse and cobalt-related oxide/hydroxide phase formation (Figure 4.20). Earlier studies on the Co-MOFs and ZIF-67 report the amorphization and conversion to Co-oxide/hydroxide.[59,78–82] XPS spectra closely reveal the new structure development and interaction between the cobalt-related nanophase and Pt nanoparticles (Figure 4.19h-j). For instance, a large shift in the Co 2p peak to lower binding energy is seen in the sample after ORR durability testing compared to the initial ZIF-67@Pt/CB. The diminished intensity of the satellite peaks at about 786 eV and 803 eV, which are attributed to the Co^{2+} oxidation state in ZIF-67, indicates the increased concentration of Co^{3+} by formation of amorphous cobalt-oxide/hydroxide phase at the expense of Co-N coordination.[83–86] The deconvolution of Co $2p_{1/2}$ and Co $2p_{3/2}$ peaks confirms the existence of Co^{2+} (peaks at ≈798 and 781.2 eV) and Co^{3+} (corresponding peaks at ≈795.5 and ≈779.9 eV) (Figure 4.19h). In addition to this, the relative peak shifts in Pt 4f XPS spectra indicate the interfacial interaction of Pt nanoparticles with cobalt-related oxide/hydroxide nanophase (Figure 4.19i). This is also evidenced in the O 1s spectra, which show three peaks at 532.3, 531.3 and 530.0 eV, corresponding to the adsorbed water (H_2O), hydroxy oxygen (O_H) and metal-O, respectively (Figure 4.19j).[83–86]This combination leads to improved ORR durability, as shown in Figure 4.19a. Such activity durability has been reported in the Pt- or Pt-relate alloy coupled MOFs or hydroxide nanophase structures.[87,88] For instance, the enhanced ORR durability

is reported in PtCo/$Co(OH)_2$@N-doped carbon with respect to Pt/CB.[88] In another case, the Pt nanoparticles embedded metal-organic framework nanosheets also showed improved ORR durability compared to Pt/CB.[87] It was reported that the higher electronegativity of the Co helps to slow down the oxidation of Pt nanoparticles as well as preventing them from aggregation and dissolution when the Pt/CB is coupled with $Co(OH)_2/Co_3O_4$.[89] Indium oxide supported Pt-In alloy nanocluster catalysts also evidenced enhanced performance for ORR.[90] Furthermore, Pt_1 single atoms on Co_3O_4 through strong electronic metal–support interactions exhibit excellent stability in sharp contrast to the rapid deactivation of Pt nanoparticles used for the dehydrogenation of ammonia borane for room-temperature hydrogen generation.[91] Overall, the ex-situ characterization indicates that the ORR activity can be correlated with the formation of the Co^{3+} related active phase coupled with Pt nanoparticles.

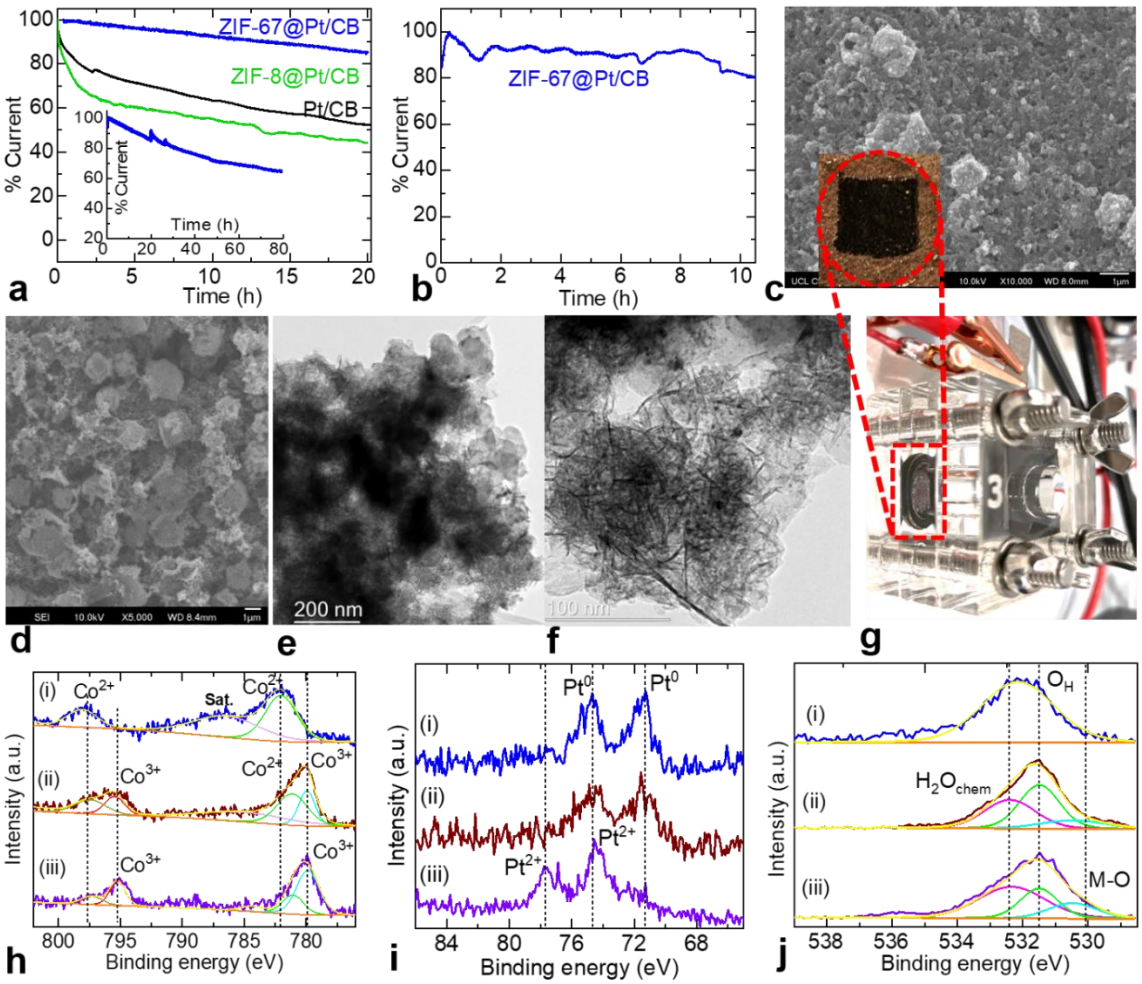

Figure 4.18. (a) ORR chronoamperometric stability curves, recorded at 0.65 V (vs RHE) for 20 h, with inset for extended ORR durability data up to 85 h. **(b)** OER chronopotentiometry curve, recorded at 10 mA cm^{-2} after conditioning for 15 min. **(c, d)** SEM micrographs of samples after battery cycling and ORR durability tests conducted for 50 and 20 h, respectively. **(e, f)** TEM micrographs after ORR durability test for 20 h. **(g)** Photograph of battery cell. **(h-j)** Comparative XPS core level spectra of Co 2p, Pt 4f and O 1s obtained on the samples before test (i), and after ORR durability for 20 h (ii) and battery cycling for 50 h (iii) tests.

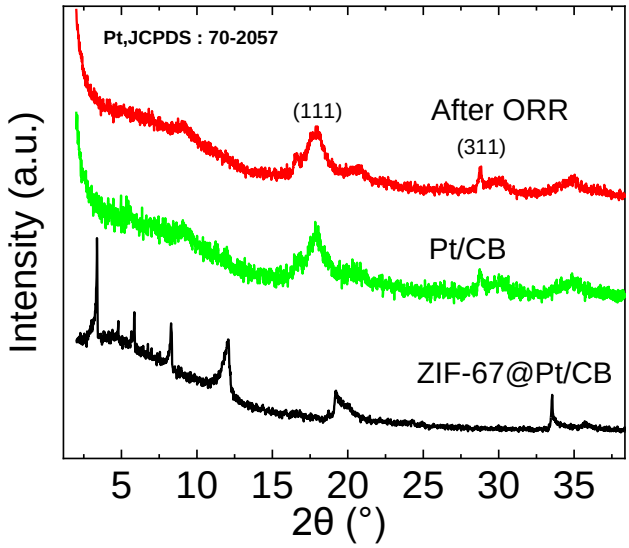

Figure 4.19. XRD patterns of ZIF-67@Pt/CB before and after ORR durability test for 20 h. Pt/CB reference XRD data is also collected for comparison purpose. The disappearance of XRD peaks in sample after 20 h ORR durability test informs the ZIF-67 degradation to amorphous phase.

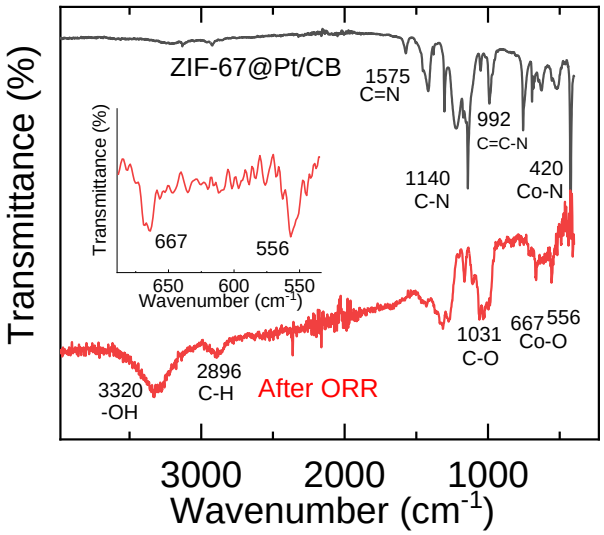

Figure 4.20. FTIR spectra of ZIF-67@Pt/CB before and after ORR durability test for 20 h. The absence of peak at 420 cm^{-1} corresponded to Co-N indicated that the decomposed ZIF structure. Besides peaks at 992 cm^{-1}, 1140 cm^{-1}, 1575 cm^{-1} also suggested the broken imidazole linker. The new peaks appeared at 556 and 667 cm^{-1} are attributed to the Co-O stretching vibrations.[86],[92] The new peak at 1031 cm^{-1} belong to C-O stretching vibration. The peak at around 3320 cm^{-1} corresponds to the OH bending vibration of water molecules. The band at 2896 cm^{-1} indicates C-H group.

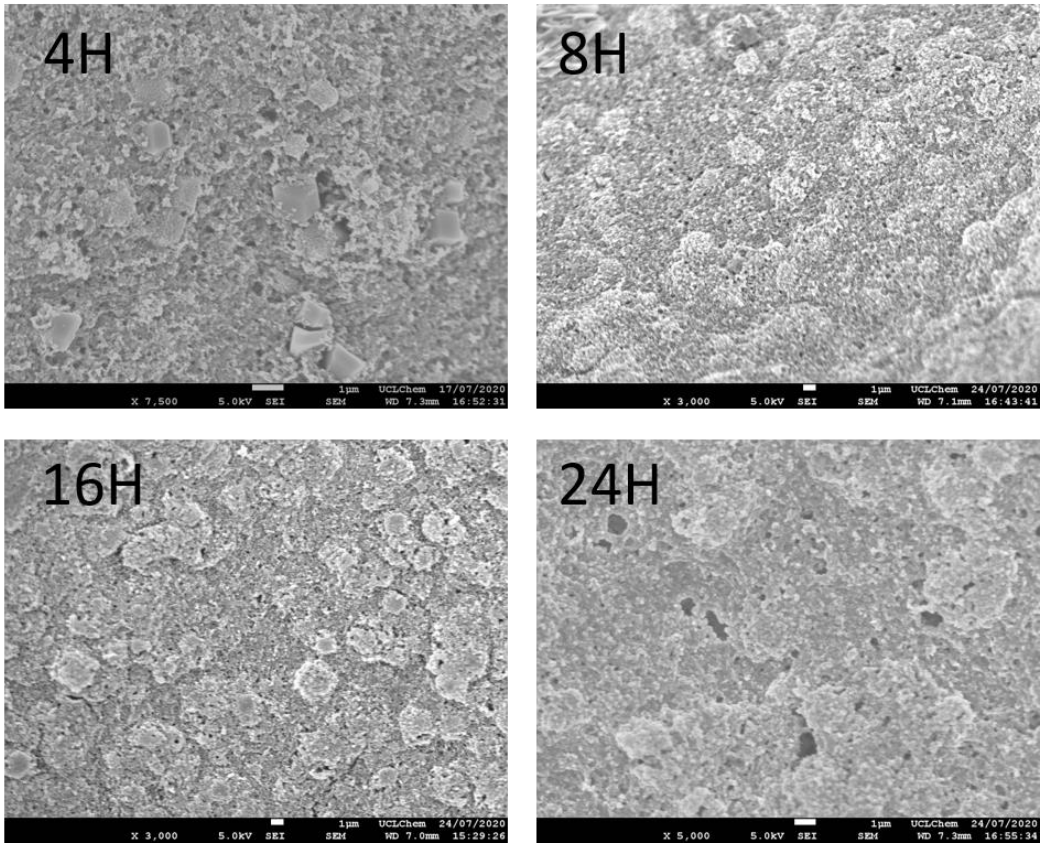

Figure 4.21. SEM images of ZIF-67@Pt/CB catalyst, taken at different cycling period after tested in a zinc-air battery cell.

4.4 Conclusion

A bifunctional and durable electrocatalytic activity for both OER and ORR is unveiled for the first time in one of the widely studied MOF structures, ZIF-67 – a cobalt-based prototype of ZIF-8 directly. Here, worth noting that no further post-synthesis chemical modification such as oxidation or carbonization at high temperature is performed. Motivated by this, the bifunctional activity of ZIF-67 for OER and ORR is demonstrated by physically combining the ZIF-67 with platinum-carbon black (ZIF-67@Pt/CB). The best bifunctional activity, with a small overpotential of ≈0.87 V, is observed for the sample with 1:1 mass ratio of ZIF-67 and Pt/CB. Interestingly, ZIF-67@Pt/CB(50wt%) enhances the ORR durability of Pt/CB, where the sample shows activity

retention of ≈85% over 20 h operation compared to the ≈52% for Pt/CB. Such activities are attributed to the synergistic coupling between Pt nanoparticles and Co-metal centres in ZIF-67. Here, the comparative ZIF-8@Pt/CB(50wt%) system shows poor activities. Remarkably, a rechargeable Zn-air battery based on ZIF-67@Pt/CB(50wt%) demonstrates excellent stability during cycling for 50 h. It also delivers an open circuit voltage of 1.42 V, maintained for measured 20 h, and a peak power density of over 150 mW cm^{-2}. Such characteristics are also comparable to many of the carbonaceous catalyst systems studied for Zn-air batteries. The present study provides a straightforward and energy-efficient strategy for designing bifunctional electrocatalysts. Focusing on economically viable strategies that do not rely on expensive raw materials and an organic linker, ZIF-67 is an exceptional candidate for energy storage and conversion applications.

4.5 References

[1] S. Dou, C.-L. Dong, Z. Hu, Y.-C. Huang, J. Chen, L. Tao, D. Yan, D. Chen, S. Shen, S. Chou, S. Wang, *Adv. Funct. Mater.* **2017**, *27*, 1702546.

[2] C. Jiao, Z. Wang, X. Zhao, H. Wang, J. Wang, R. Yu, D. Wang, *Angew. Chem. Int. Ed.* **2019**, *58*, 996.

[3] S. Dang, Q.-L. Zhu, Q. Xu, *Nat. Rev. Mater.* **2017**, *3*, 17075.

[4] Z. Cai, Z. Wang, J. Kim, Y. Yamauchi, *Adv. Mater.* **2019**, *31*, 1804903.

[5] B. N. Bhadra, A. Vinu, C. Serre, S. H. Jhung, *Mater. Today* **2018**, *25*, 88.

[6] W. Yang, X. Li, Y. Li, R. Zhu, H. Pang, *Adv. Mater.* **2018**, *31*, 1804740.

[7] H. Zhang, S. Hwang, M. Wang, Z. Feng, S. Karakalos, L. Luo, Z. Qiao, X. Xie, C. Wang, D. Su, Y. Shao, G. Wu, *J. Am. Chem. Soc.* **2017**, *139*, 14143.

[8] S. Gadipelli, W. Travis, W. Zhou, Z. Guo, *Energy Environ. Sci.* **2014**, *7*, 2232.

[9] Y. He, G. Wang, S. Hwang, D. A. Cullen, M. A. Uddin, L. Langhorst, B. Li, S. Karakalos, A. J. Kropf, E. C. Wegener, J. Sokolowski, M. Chen, D. Myers, D. Su, K. L. More, S.

Litster, G. Wu, *Energy Environ. Sci.* **2019**, *12*, 250.

[10] J. Han, X. Meng, L. Lu, J. Bian, Z. Li, C. Sun, *Adv. Funct. Mater.* **2019**, 1808872.

[11] X. Han, X. Ling, Y. Wang, T. Ma, C. Zhong, W. Hu, Y. Deng, *Angew. Chem. Int. Ed.* **2019**, *58*, 5359.

[12] Y. Zhong, Z. Pan, X. Wang, J. Yang, Y. Qiu, S. Xu, Y. Lu, Q. Huang, W. Li, *Adv. Sci.* **2019**, 1802243.

[13] S. Gadipelli, T. Zhao, S. A. Shevlin, Z. Guo, *Energy Environ. Sci.* **2016**, *9*, 1661.

[14] Q. Yang, C.-C. Yang, C.-H. Lin, H.-L. Jiang, *Angew. Chem. Int. Ed.* **2019**, *58*, 3511.

[15] Y. Deng, B. Chi, J. Li, G. Wang, L. Zheng, X. Shi, Z. Cui, L. Du, S. Liao, K. Zang, J. Luo, Y. Hu, X. Sun, *Adv. Energy Mater.* **2019**, *9*, 1802856.

[16] X. Wan, X. Liu, Y. Li, R. Yu, L. Zheng, W. Yan, H. Wang, M. Xu, J. Shui, *Nat. Catal.* **2019**, *2*, 259.

[17] D. Micheroni, G. Lan, W. Lin, *J. Am. Chem. Soc.* **2018**, *140*, 15591.

[18] W. Zhang, X. Yao, S. Zhou, X. Li, L. Li, Z. Yu, L. Gu, *Small* **2018**, *14*, 1800423.

[19] N. Ranjbar Sahraie, J. P. Paraknowitsch, C. Göbel, A. Thomas, P. Strasser, *J. Am. Chem. Soc.* **2014**, *136*, 14486.

[20] S. Dresp, F. Luo, R. Schmack, S. Kühl, M. Gliech, P. Strasser, *Energy Environ. Sci.* **2016**, *9*, 2020.

[21] Q. Liu, Y. Wang, L. Dai, J. Yao, *Adv. Mater.* **2016**, *28*, 3000.

[22] X. Han, G. He, Y. He, J. Zhang, X. Zheng, L. Li, C. Zhong, W. Hu, Y. Deng, T.-Y. Ma, *Adv. Energy Mater.* **2018**, *8*, 1702222.

[23] T. Sun, J. Wang, C. Qiu, X. Ling, B. Tian, W. Chen, C. Su, *Adv. Sci.* **2018**, *5*, 1800036.

[24] W. Hu, Q. Wang, S. Wu, Y. Huang, *J. Mater. Chem. A* **2016**, *4*, 16920.

[25] J. Yin, Y. Li, F. Lv, Q. Fan, Y. Q. Zhao, Q. Zhang, W. Wang, F. Cheng, P. Xi, S. Guo, *ACS Nano* **2017**, *11*, 2275.

[26] Y. Wang, J. Fu, Y. Zhang, M. Li, F. M. Hassan, G. Li, Z. Chen, *Nanoscale* **2017**, *9*, 15865.

[27] P. Chen, T. Zhou, L. Xing, K. Xu, Y. Tong, H. Xie, L. Zhang, W. Yan, W. Chu, C. Wu, Y. Xie, *Angew. Chem. Int. Ed.* **2017**, *56*, 610.

[28] Y. Liu, H. Jiang, Y. Zhu, X. Yang, C. Li, *J. Mater. Chem. A* **2016**, *4*, 1694.

[29] G. Fu, Y. Chen, Z. Cui, Y. Li, W. Zhou, S. Xin, Y. Tang, J. B. Goodenough, *Nano Lett.* **2016**, *16*, 6516.

[30] S. Dou, L. Tao, J. Huo, S. Wang, L. Dai, *Energy Environ. Sci.* **2016**, *9*, 1320.

[31] Y. Li, H. Dai, *Chem. Soc. Rev.* **2014**, *43*, 5257.

[32] D. Ji, L. Fan, L. Li, S. Peng, D. Yu, J. Song, S. Ramakrishna, S. Guo, *Adv. Mater.* **2019**, *31*, 1808267.

[33] Q. Hu, G. Li, G. Li, X. Liu, B. Zhu, X. Chai, Q. Zhang, J. Liu, C. He, *Adv. Energy Mater.* **2019**, *9*, 1803867.

[34] Y. Cheng, Y. Wang, Q. Wang, Z. Liao, Ni. Zhang, Y. Guo, Z. Xiang, *J. Mater. Chem. A* **2019**, *7*, 9831.

[35] J. Zhu, Y. Huang, W. Mei, C. Zhao, C. Zhang, J. Zhang, I. S. Amiinu, S. Mu, *Angew. Chem. Int. Ed.* **2019**, *58*, 3859.

[36] J. Gao, J. Wang, L. Zhou, X. Cai, D. Zhan, M. Hou, L. Lai, *ACS Appl. Mater. Interfaces* **2019**, *11*, 10364.

[37] X. Zhao, P. Pachfule, S. Li, T. Langenhahn, M. Ye, G. Tian, J. Schmidt, A. Thomas, *Chem. Mater.* **2019**, *31*, 3274.

[38] L. Chen, Y. Zhang, X. Liu, L. Long, S. Wang, W. Yang, J. Jia, *Chem. Commun.* **2019**, *55*, 5651.

[39] D. Wang, L. Xiao, P. Yang, Z. Xu, X. Lu, L. Du, O. Levin, L. Ge, X. Pan, J. Zhang, M. An, *J. Mater. Chem. A* **2019**, *7*, 11007.

[40] G. Li, L. Pei, Y. Wu, B. Zhu, Q. Hu, H. Yang, Q. Zhang, J. Liu, C. He, *J. Mater. Chem. A*

2019, *7*, 11223.

[41] X. Han, X. Ling, Y. Wang, T. Ma, C. Zhong, W. Hu, Y. Deng, *Angew. Chem* **2019**, *131*, 5413.

[42] L. Wei, H. E. Karahan, S. Zhai, H. Liu, X. Chen, Z. Zhou, Y. Lei, Z. Liu, Y. Chen, *Adv. Mater.* **2017**, *29*, 1701410.

[43] Q. Wang, Y. Ji, Y. Lei, Y. Wang, Y. Wang, Y. Li, S. Wang, *ACS Energy Lett.* **2018**, *3*, 1183.

[44] Q. Qin, H. Jang, L. Chen, G. Nam, X. Liu, J. Cho, *Adv. Energy Mater.* **2018**, *8*, 1801478.

[45] P. Pei, K. Wang, Z. Ma, *Appl. Energy* **2014**, *128*, 315.

[46] Y. Li, M. Gong, Y. Liang, J. Feng, J.-E. Kim, H. Wang, G. Hong, B. Zhang, H. Dai, *Nat. Commun.* **2013**, *4*, 1805.

[47] P. Kanninen, B. Eriksson, F. Davodi, M. E. M. Buan, O. Sorsa, T. Kallio, R. W. Lindström, *Electrochim. Acta* **2020**, *332*, 135384.

[48] H. Tang, Z. Qi, M. Ramani, J. F. Elter, *J. Power Sources* **2006**, *158*, 1306.

[49] W. Wang, J. Luo, S. Chen, *Chem. Commun.* **2017**, *53*, 11556.

[50] B. H. R. Suryanto, C. Zhao, *Chem. Commun.* **2016**, *52*, 6439.

[51] H. Guo, Q. Feng, J. Zhu, J. Xu, Q. Li, S. Liu, K. Xu, C. Zhang, T. Liu, *J. Mater. Chem. A* **2019**, *7*, 3664.

[52] J.-C. Li, X.-T. Wu, L.-J. Chen, N. Li, Z.-Q. Liu, *Energy* **2018**, *156*, 95.

[53] C.-Y. Su, H. Cheng, W. Li, Z.-Q. Liu, N. Li, Z. Hou, F.-Q. Bai, H.-X. Zhang, T.-Y. Ma, *Adv. Energy Mater.* **2017**, *7*, 1602420.

[54] L. Yang, S. Feng, G. Xu, B. Wei, L. Zhang, *ACS Sustain. Chem. Eng.* **2019**, *7*, 5462.

[55] Y.-N. Hou, Z. Zhao, H. Zhang, C. Zhao, X. Liu, Y. Tang, Z. Gao, X. Wang, J. Qiu, *Carbon.* **2019**, *144*, 492.

[56] L. Ma, R. Wang, Y.-H. Li, X.-F. Liu, Q.-Q. Zhang, X.-Y. Dong, S.-Q. Zang, *J. Mater.*

Chem. A **2018**, *6*, 24071.

[57] S. Dou, X. Li, L. Tao, J. Huo, S. Wang, *Chem. Commun.* **2016**, *52*, 9727.

[58] Z. Pei, H. Li, Y. Huang, Q. Xue, Y. Huang, M. Zhu, Z. Wang, C. Zhi, *Energy Environ. Sci.* **2017**, *10*, 742.

[59] G. Chen, J. Zhang, F. Wang, L. Wang, Z. Liao, E. Zschech, K. Müllen, X. Feng, *Chem. – A Eur. J.* **2018**, *24*, 18413.

[60] C. Hang, J. Zhang, J. Zhu, W. Li, Z. Kou, Y. Huang, *Adv. Energy Mater.* **2018**, *8*, 1703539.

[61] Z. Bai, S. Li, J. Fu, Q. Zhang, F. Chang, L. Yang, J. Lu, Z. Chen, *Nano Energy* **2019**, *58*, 680.

[62] C. Deng, K. H. Wu, J. Scott, S. Zhu, X. Zheng, R. Amal, D. W. Wang, *ACS Appl. Mater. Interfaces* **2019**, *11*, 9925.

[63] M. Zhang, Q. Dai, H. Zheng, M. Chen, L. Dai, *Adv. Mater.* **2018**, *30*, 1705431.

[64] Y. Guo, P. Yuan, J. Zhang, Y. Hu, I. S. Amiinu, X. Wang, J. Zhou, H. Xia, Z. Song, Q. Xu, S. Mu, *ACS Nano* **2018**, *12*, 1894.

[65] P. Liu, D. Gao, W. Xiao, L. Ma, K. Sun, P. Xi, D. Xue, J. Wang, *Adv. Funct. Mater.* **2018**, *28*, 1706928.

[66] S. Peng, X. Han, L. Li, S. Chou, D. Ji, H. Huang, Y. Du, J. Liu, S. Ramakrishna, *Adv. Energy Mater.* **2018**, *8*, 1800612.

[67] Y. Jiang, Y.-P. Deng, J. Fu, D. U. Lee, R. Liang, Z. P. Cano, Y. Liu, Z. Bai, S. Hwang, L. Yang, D. Su, W. Chu, Z. Chen, *Adv. Energy Mater.* **2018**, *8*, 1702900.

[68] L. An, Y. Li, M. Luo, J. Yin, Y.-Q. Zhao, C. Xu, F. Cheng, Y. Yang, P. Xi, S. Guo, *Adv. Funct. Mater.* **2017**, *27*, 1703779.

[69] F. Meng, H. Zhong, D. Bao, J. Yan, X. Zhang, *J. Am. Chem. Soc.* **2016**, *138*, 10226.

[70] D. Liu, B. Wang, H. Li, S. Huang, M. Liu, J. Wang, Q. Wang, J. Zhang, Y. Zhao, *Nano Energy* **2019**, *58*, 277.

[71] S. S. Shinde, C. H. Lee, J.-Y. Jung, N. K. Wagh, S.-H. Kim, D.-H. Kim, C. Lin, S. U. Lee, J.-H. Lee, *Energy Environ. Sci.* **2019**, *12*, 727.

[72] S. S. Shinde, J. Y. Yu, J. W. Song, Y. H. Nam, D. H. Kim, J. H. Lee, *Nanoscale Horizons* **2017**, *2*, 333.

[73] H. Mei, M. Yang, Y. Shen, F. He, Z. Zhou, X. Chen, Y. Yang, S. Liu, Y. Zhang, *Carbon.* **2019**, *144*, 312.

[74] Y. Xu, P. Deng, G. Chen, J. Chen, Y. Yan, K. Qi, H. Liu, B. Y. Xia, *Adv. Funct. Mater.* **2020**, *30*, 1906081.

[75] D. Ren, J. Ying, M. Xiao, Y. Deng, J. Ou, J. Zhu, G. Liu, Y. Pei, S. Li, A. M. Jauhar, H. Jin, S. Wang, D. Su, A. Yu, Z. Chen, *Adv. Funct. Mater.* **2020**, *30*, 1908167.

[76] Z. Wang, H. Jin, T. Meng, K. Liao, W. Meng, J. Yang, D. He, Y. Xiong, S. Mu, *Adv. Funct. Mater.* **2018**, *28*, 1802596.

[77] D. Chen, X. Chen, Z. Cui, G. Li, B. Han, Q. Zhang, J. Sui, H. Dong, J. Yu, L. Yu, L. Dong, *Chem. Eng. J.* **2020**, *399*, 125718.

[78] Q. Qian, Y. Li, Y. Liu, L. Yu, G. Zhang, *Adv. Mater.* **2019**, *31*, 1901139.

[79] T. Wen, Y. Zheng, J. Zhang, K. Davey, S. Qiao, *Adv. Sci.* **2019**, *6*, 1801920.

[80] N. Y. Huang, J. Q. Shen, Z. M. Ye, W. X. Zhang, P. Q. Liao, X. M. Chen, *Chem. Sci.* **2019**, *10*, 9859.

[81] W. Zheng, M. Liu, L. Y. S. Lee, *ACS Catal.* **2020**, *10*, 81.

[82] D. Zhang, H. Shi, R. Zhang, Z. Zhang, N. Wang, J. Li, B. Yuan, H. Bai, J. Zhang, *RSC Adv.* **2015**, *5*, 58772.

[83] D. Su, X. Zhang, A. Wu, H. Yan, Z. Liu, L. Wang, C. Tian, H. Fu, *NPG Asia Mater.* **2019**, *11*, 78.

[84] A. Bucci, S. S. Mondal, V. Martin-Diaconescu, A. Shafir, J. Lloret-Fillol, *ACS Appl. Energy Mater.* **2019**, *2*, 8930.

[85] Y. Liang, J. Wei, Y. X. Hu, X. F. Chen, J. Zhang, X. Y. Zhang, S. P. Jiang, S. W. Tao, H.

T. Wang, *Nanoscale* **2017**, *9*, 5323.

[86] J. Xu, P. Gao, T. S. Zhao, *Energy Environ. Sci.* **2012**, *5*, 5333.

[87] Z. Xia, J. Fang, X. Zhang, L. Fan, A. J. Barlow, T. Lin, S. Wang, G. G. Wallace, G. Sun, X. Wang, *Appl. Catal. B Environ.* **2019**, *245*, 389.

[88] K. Wang, W. Wu, Z. Tang, L. Li, S. Chen, N. M. Bedford, *ACS Appl. Mater. Interfaces* **2019**, *11*, 4983.

[89] S. Hu, G. Goenaga, C. Melton, T. A. Zawodzinski, D. Mukherjee, *Appl. Catal. B Environ.* **2016**, *182*, 286.

[90] Y. Cheng, X. Zhao, Y. Yu, L. Chen, T. Cheng, J. Huang, Y. Liu, M. Harada, A. Ishihara, Y. Wang, *J. Power Sources* **2020**, *446*, 227332.

[91] J. Li, Q. Guan, H. Wu, W. Liu, Y. Lin, Z. Sun, X. Ye, X. Zheng, H. Pan, J. Zhu, S. Chen, W. Zhang, S. Wei, J. Lu, *J. Am. Chem. Soc.* **2019**, *141*, 14515.

[92] C. Nethravathi, S. Sen, N. Ravishankar, M. Rajamathi, C. Pietzonka, B. Harbrecht, *J. Phys. Chem. B* **2005**, *109*, 11468.

Chapter 5. An in-situ electrochemically generated highly active ZIF-67 based cathode catalyst for zinc-air batteries with remarkable performance

5.1 Introduction

Platinum and other precious metal-based materials, including iridium, ruthenium and their compounds are widely used as bifunctional catalysts for ORR/OER due to favorable surface electronic structures for electrochemical reactions. However, the high cost and poor stability associated with these noble metals inhibited their widespread implementation into the batteries.[1,2] Thus, non-precious metal based electrocatalysts with superb bifunctional performance have attracted increasing attention. Recent studies suggest that during OER a series of metal-stabilized intermediates such as M-OH, M-O, M-OOH are generated, which further improves catalytic performance.[3–5] Simulations also provide evidence that surface hydroxide ligands can lower the energy barrier than an external H_2O/OH^- to couple with the discharged species.[6] Alkaline electrolyte modified MOF to generate metal oxide/hydroxide@MOF with more active sites and stable structure delivered high catalytic activity.[4] In chapter 3 and chapter 4, we discussed the ZIF-67 derived catalysts exhibit excellent OER activity and ZIF-67/Pt-CB composites with great bifunctional catalytic performance that has been demonstrated in RDE setup and zinc air batteries. And during the electrochemical cycling, the pristine ZIF-67 could transform into a mostly amorphous phase. In this chapter, I focused on the different particle size based ZIF-67 samples without mixing with commercial platinum carbon as discussed in chapter 4 and studied their electrocatalytic activity evolution directly by implementing them into zinc-air cells following in-situ activation under continuous charge-discharge cycles.

After the charge-discharge cycling activation process, the round-up efficiency of 1000 nm ZIF-67 improved from ~32% to 61% for 700 h cycling test, the voltage gap and round-up efficiency of 200 nm ZIF-67 is hugely improved from 1.26 V (39.7%) to 0.89V (56.6%) and long lasting stability for over 1100 h, compared to the benchmark commercial platinum carbon with 62%, which is decreased to 43% in the same time range. Power density of zinc-air battery is increased to nearly 4.5 times, with a change from 39.3 mW cm^{-2} initially to 180 mW cm^{-2}.

5.2 Experimental Section

5.2.1 Synthesis

Synthesis of controlled particle size ZIF-67 samples: ZIF-67 with particle size of 200 nm is synthesised as following: 5.9 g cobalt nitrate hexahydrate and 0.5 g polyvinylpyrrolidone (PVP) were dissolved in a 500 ml methanol. Then 6.65 g of 2-methyl imidazole was mixed in another 500 ml methanol. Then the solution was stirring and slowly added to the former solution. After a few minutes the solution changed from the clear to milky white, which was then left for a day to settle. Clear solution was poured out and the precipitate sample was extracted after several washings by methanol. ZIF-67 with particle size of 1000 nm is synthesised similar to above described method except adding 4 ml 1-methylimidazole. All the samples were dried at 80 °C oven. The 200 nm ZIF-67 were prepared with 22.5 μL of TEA (triethylamine). The as-synthesized sample were then used for electrochemical test.

5.2.2 Structure and porosity characterizations

Powder X-ray diffraction patterns (PXRD) were collected by Stoe Stadi-P, Mo–K-alpha. Fourier-transform infrared (FTIR) data was obtained by Bruker ALPHA FTIR Spectrometer (Platinum-ATR) with background correction. X-ray photoemission spectroscopy (XPS, on Al–K-alpha, Thermo Scientific) data and scanning electron microscopy (SEM, on JSM6700, Jeol) measurements were carried out on the samples supported on a carbon tape. The porosity by N_2, and CO_2 adsorption-desorption isotherms were measured at 77 K and 298 K, respectively, on a Quantachrome Autosorb-iQC. All the samples were degassed at 180 ℃ overnight under a dynamic vacuum prior to the actual gas adsorption measurements. The specific surface area was measured from the 77 K N_2 isotherm in a relative pressure range between 0.01 and 0.2, according to the

Brunauer–Emmett–Teller (BET) method. The pore volume was obtained from the adsorption volume at relative pressure of 0.95.

5.2.3 Electrochemical tests

All the electrochemical catalytic activity of the samples were reported using a potentiostation (Autolab, Metrohm PGSTAT302N) with a rotating-disk three-electrode (RDE) cell configuration composed of a glassy carbon rotating disk with active material as working electrode, and (1 × 1) cm^2 Pt and Ag/AgCl/saturated KCl as counter and reference electrode, respectively. All the measurements were carried out in O_2-saturated alkaline (0.1 M KOH and 1.0 M KOH) electrolyte at room temperature. The catalyst loading was fixed at ~0.28 mg cm^{-2} on a 3 mm diameter (or area of 0.0707 cm^2) glassy carbon electrode (GCE). The catalyst was prepared as follows; 2 mg of sample was dispersed in a total 500 µl solution consisting 482 µl of deionized water plus 18 µl of Nafion (5% solution) under sonication. The sonication was carried out for up to an hour to get uniform catalyst dispersion of ink. Of this 5 µl was micropipetted and dropped on to a GCE followed by drying at <60 ℃ in an oven prior to the electrochemical tests. The cyclic voltammetry (CV) and linear sweep voltammetry (LSV) curves were recorded with voltage sweeping at 10 mV s^{-1} in the potential range of +0.2 V to +1.0 V in case of OER and in the range of +0.2 V to −0.8 V in case of ORR. OER durability tests by chronoamperometric (*I vs t*) were carried out at a fixed potential of +1.65 V (vs RHE), and the response current was recorded against time. In chronopotentiometry (*V vs t*), the response potential was recorded against time at a fixed current density of 10 mA cm^{-2}. All of the OER LSV curves were recorded at constant rpm of 1600. ORR LSV curves were recorded at discrete rotation rates between 400 rpm and 2000 rpm. All the reported current densities were estimated by normalizing the actual current response to the electrode area of GCE. The following relation is used for potential representation V (vs RHE) = $E_{Ag/AgCl}$ + 0.197 + 0.059 × pH. The overpotential is reported according to the relation; V = V_{RHE} − 1.23 V.

5.2.4 Fabrication of Zn-air batteries

Two-electrode zinc-air battery liquid cells were fabricated within the commercial battery cell cases. Briefly, air-cathodes were prepared by loading catalysts on carbon paper *via* a drop-casting method,

the material active area is maintained around 0.25 cm^{-2}. As-synthesized catalysts were mixed with the Nafion solution (0.1 % w/w in ethanol) to form the ink with a concentration of 4 mg mL^{-1}. For comparison, Pt/CB and Pt/CB+IrO_2 catalysts were also prepared by mixing commercial Pt/CB (mass loading of 0.5 mg cm^{-2}). Zinc plate with 3 mm thickness, polished by 10% hydrochloric acid and DI water in an ultrasonicator for 3 min each, and used as the anode. 6.0 M KOH with 0.2 M $Zn(CH_3COO)_2.2H_2O$ was prepared as the electrolyte to ensure the reversible redox reaction at the anode.

The power density (P in mW cm^{-2}) is estimated based on the equation: $P = U \times J$, where U is a battery voltage (V), and J is a current density (mA cm^{-2}).

Calculation method for energy density and specific capacity:

Specific capacity= $\frac{Current \times Service\ hours}{Weight\ of\ consumed\ zinc}$

5.3 Results and discussion

ZIF-67 with rhombic dodecahedral structure is synthesized via room temperature stirring route by using cobalt nitrate and 2-methylimidazole.[7] Scanning electron microscopy (SEM) images reveal uniform particles with an average size of 1000 nm (Figure 5.1a). Powder X-ray diffraction (PXRD) and X-ray photoemission spectroscopy (XPS) data confirms that the crystalline nature and element composition of the sample (Figure 5.1b-d). A rechargeable zinc-air battery (ZAB) is assembled by using ZIF-67 coated on hydrophobic carbon paper as an air cathode and polished zinc plate as an anode, and 6 M KOH with 0.2 M zinc acetate as electrolyte.

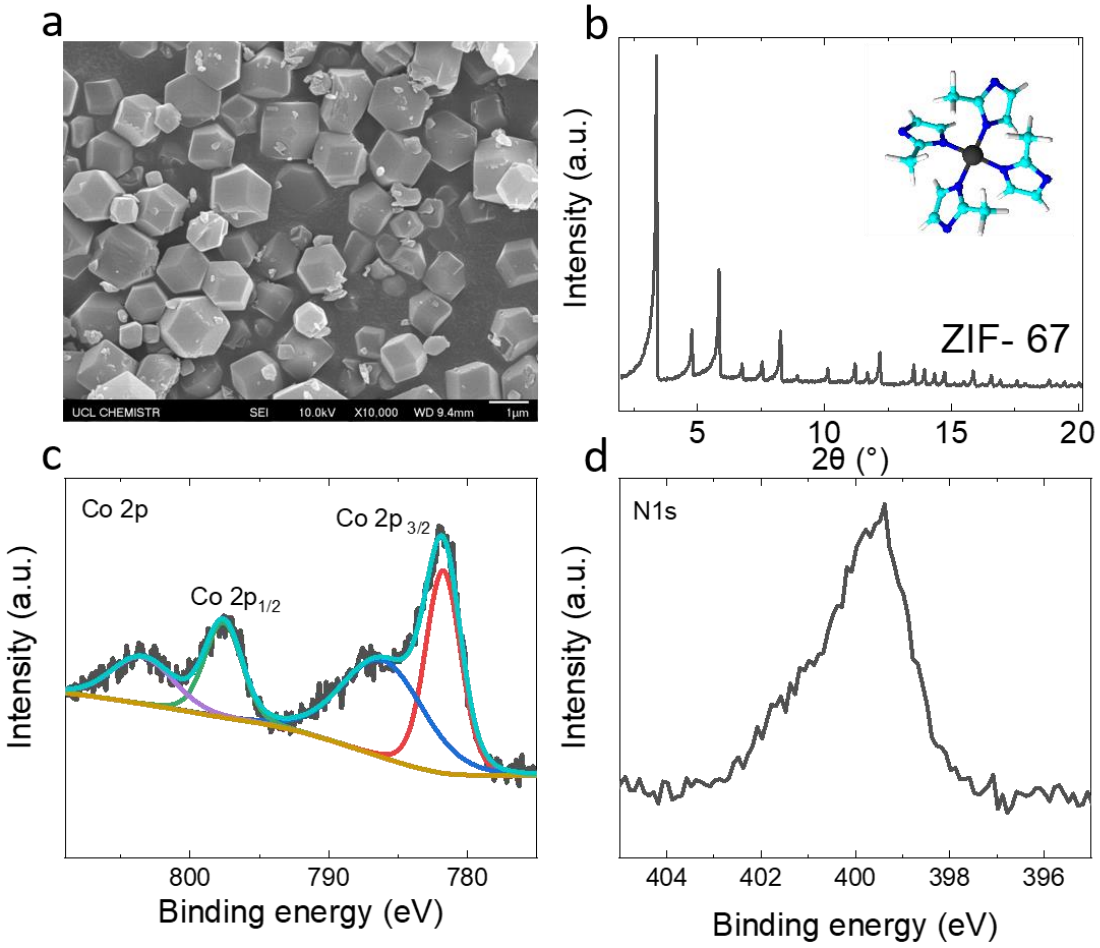

Figure 5.1. (a) SEM image of ZIF-67. **(b)** XRD pattern of ZIF-67. **(c-d)** Co 2p and N1s of XPS spectra.

Firstly, the open circuit voltage of zinc air battery is measured. As presented in Figure 5.2, it is slowly increased from 1.34 V initially to 1.41 V after 30 hours. This improvement in OCV indicates structure evolution under the alkaline electrolyte environment.[4,8] To optimize the activation process, charge-discharge cycling process at varied current densities between 5 and 40 mA cm^{-2} is performed (Figure 5.3 and 5.4). A slow activation process is found both in discharge and charge platform. After the initial voltage slope, the voltage gap between charge and discharge voltage steps starts to narrow from 1.27 V and down to 0.91 V in the first 40 h cycling test and slowly enlarged to achieve 0.77 V for 700 h. Besides, the round up efficiency improves from 32.4% to 53.8%, which is better than benchmark commercial platinum carbon, which indeed decreased from 62% to 43%, and the bifunctional Pt/CB with IrO_2/CB also shows the decreased activity from 61% to 53% (Figure 5.3b-c). Remarkably, the galvanostatic discharge and charge cycling at higher current densities (20 to 40 mA cm^{-2}) exhibits same performance-evolution trend and stable voltage gap for 240 h (Figure 5.4). Though, it is found that under high current density, like 40 mA cm^{-2}, the electrode is hard to survive for a long time during charge-discharge cycling, the activated ZIF-67 survived for about 40 h with around 39% round-up efficiency. When tested at 20 and 30 mA cm^{-2}, the catalyst exhibited a great improvement in the charge-discharge platform and round up efficiency.

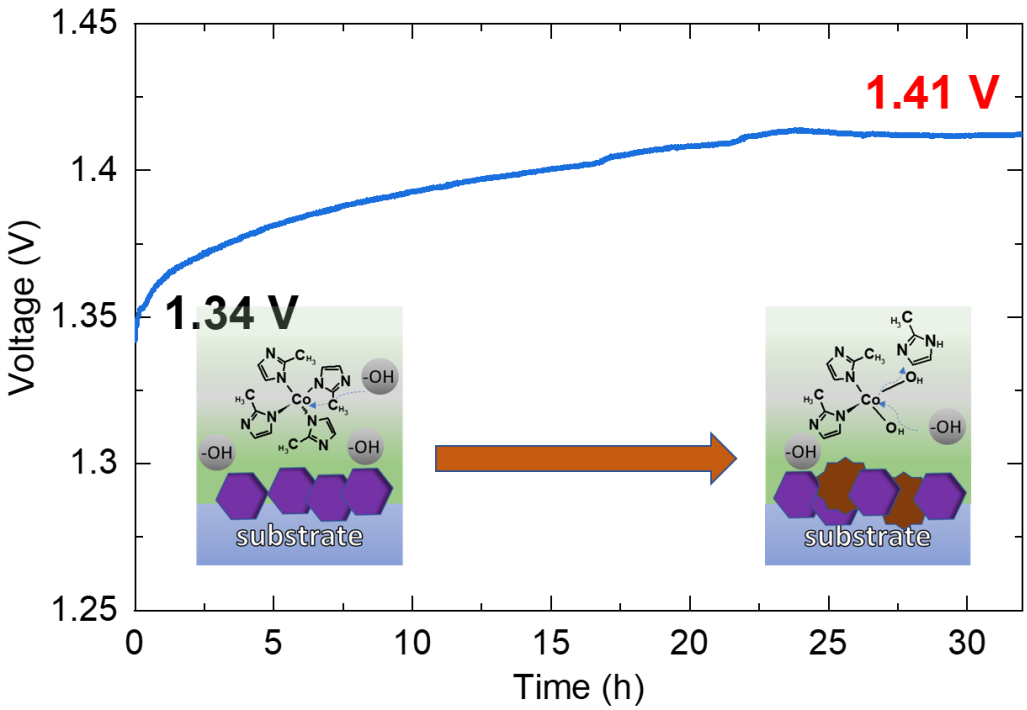

Figure 5.2. OCV of a zinc-air battery with ZIF-67 catalyst deposited on GDLCP cathode, with inset for schematic representation for the electrochemically transformed molecular active catalyst structure.

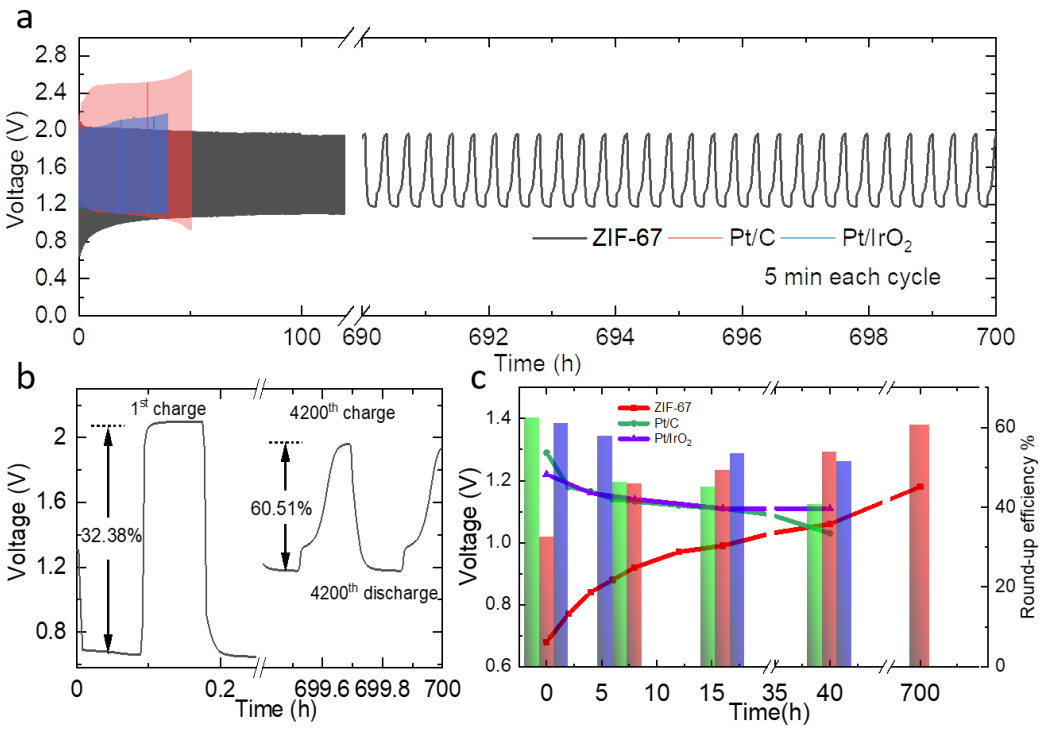

Figure 5.3. (a-b) Long-life charge−discharge cyclic tests, up to 700 h, for the batteries comprising different cathode catalysts (ZIF-67 – black; Pt/CB – red; (Pt+IrO_2)/CB – blue) operated at a fixed current density of 5 mA cm^2 (5 min for each cycle). **(c)** Bar and line symbol graph describe the discharge voltage and round-up efficiency of the catalysts.

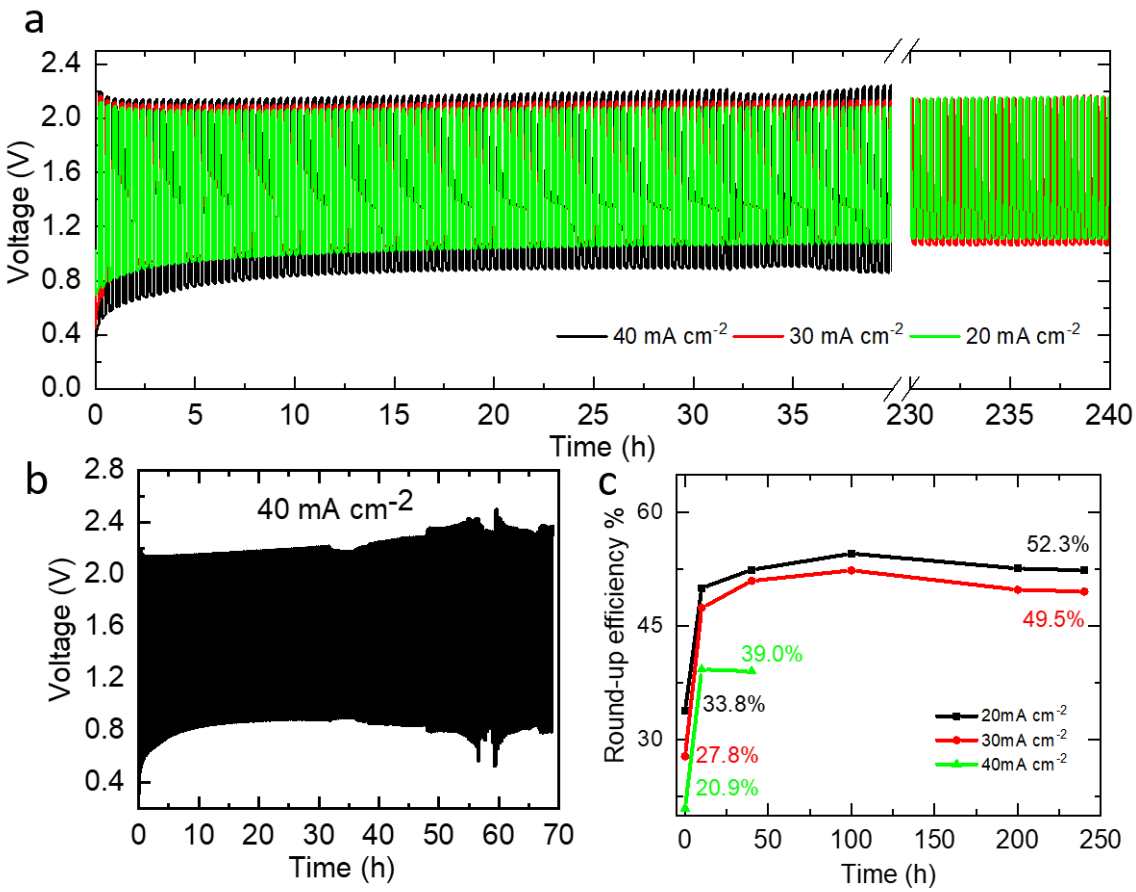

Figure 5.4. (a-b) Long-life charge–discharge cyclic tests of the ZIF-67 based batteries, which are operated at different fixed current densities of 20, 30 and 40 mA cm^2 (10 min for each cycle), measured continuously up to 240 h. **(c)** The corresponding round-up efficiencies of the batteries under different current densities.

As demonstrated in the Chapter 3, the smaller particle size of ZIF-67, in ~50 or 200 nm, offers higher bifunctional performance. Thus, I have focused particularly on the ZIF-67 sample with particle size of ~200 nm to evaluate the performance in practical ZABs. To my expectation, the 200 nm ZIF-67 displayed a better discharge-charge platform compared with 1000 nm ZIF-67 (Figure 5.5). The electrochemically activated ZIF-67 (EZIF-67) sample then used as cathode catalyst directly to fabricate the rechargeable ZAB cells. Figure 5.6 shows a EZIF-67 based full cell performance profiles, where EZIF-67 is developed with 40 h electrochemical activation. The EZIF-67 based cell shows superior discharge voltage at different current densities of 2, 10, 20, and 40 mA cm^{-2} (Figure 5.6a). The EZIF-67 based cell delivers higher power density up to 180 mW

cm^{-2}, which is 4.5 times higher than the pristine ZIF-67 and also ~100 mW cm^{-2} higher than Pt/CB catalyst based cell (Figure 5.6b). Moreover, the EZIF-67 battery power delivery is competent to many reported cobalt based catalyst materials that were produced under intense chemical/temperature modifications (Figure 5.6c).[9,10,19–23,11–18] The battery with EZIF-67 can deliver a discharge specific capacity of 691 mAh g^{-1} at 10 mA cm^{-2} based on the mass of consumed Zn (Figure 5.6d). The cycling tests were carried out at a current density of 5 mA cm^{-2} for 10 min each cycle. Impressively, as shown in Figure 5.6e, the EZIF-67 shows outstanding cycling stability for 1100 h (>6600 cycles) without significant voltage fading and is a best performance ever reported to date (Figure 5.6e). Moreover, the voltage gap and round-up efficiency is significantly improved from 1.26 V (39.7%) to 0.89V (56.6%).

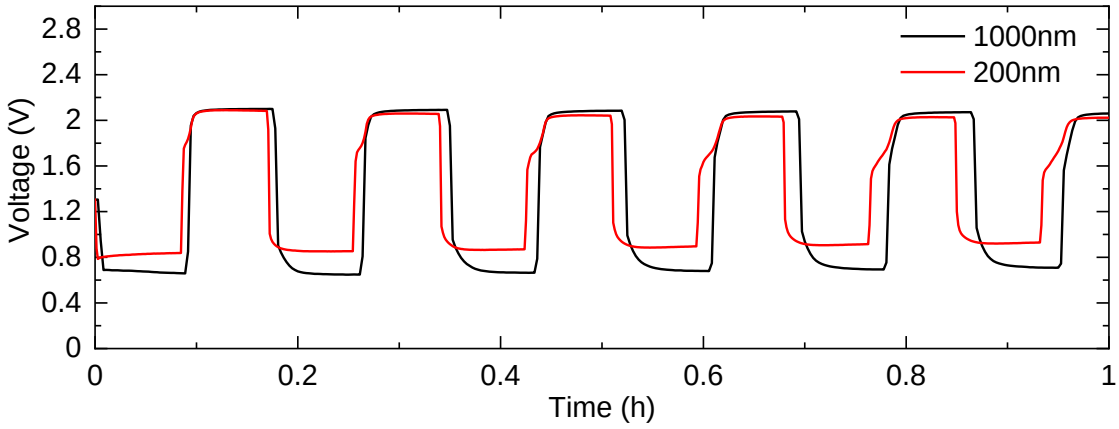

Figure 5.5. Charge−discharge cyclic tests of the ZIF-67 with different particle size, measured at a fixed current density of 5 mA cm^2.

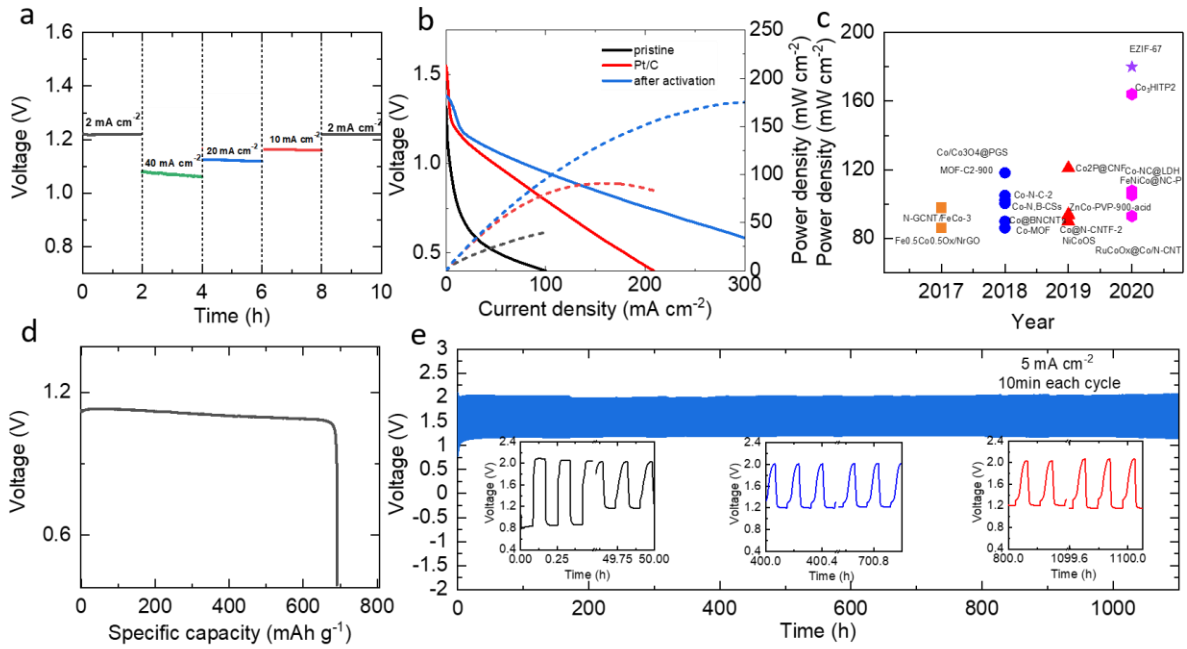

Figure 5.6. The EZIF-67 based battery characteristics: **(a)** Discharge profiles at various current densities from 2 mA cm^{-2} to 40 mA cm^{-2}. **(b)** Discharge polarization curves and corresponding discharge power density curves, for comparison the ZIF-67 (pristine) and Pt/CB based battery performances are also reported under similar fabrication and operating conditions. **(c)** The power density comparison data from the battery in this work and cobalt based materials from the literature. **(d)** Discharge curve measured under continuous discharge until complete consumption of Zn at 10 mA cm^{-2}. Specific capacity was normalized to the mass of consumed Zn. **(e)** Long-life charge−discharge cyclic tests measured at a fixed current density of 5 mA cm^{-2} (10 min for each cycle).

To discover the mechanisms behind the improvement of the electrochemical behaviors, first, the electrodes after running charge-discharge cycling test (5 mA cm^{-2} for 10 min each cycle) at different time scales are further investigated for ORR and OER activity in O_2 saturated 1M KOH under three-electrode configuration. Both the ORR and OER performances are improved for the EZIF-67 sample with increased cyclic test compared to a fresh ZIF-67. Such activity evolution is in agreement with the charge-discharge cycling test data shown in Figure 5.3c, for example, after 24 h cycling test the charge-discharge platform become stable (Figure 5.7). Furthermore, the increasing trend of the current in the cyclic voltammetry (CV) tests suggests the growth of the electrochemical surface area (ECSA) of EZIF-67 against CV cycle numbers (Figure 5.8a-c). The

double layer capacitance (Cdl) of ZIF-67 after 24 hours activation is 33.81 mF cm^{-2}, which is much higher than the pristine ZIF-67 value of 10.48 mF cm^{-2} (Figure 5.8d and 5.9). Electrochemical impedance spectroscopy also indicates better electrolyte diffusion with the activated ZIF-67 sample (Figure 5.10).

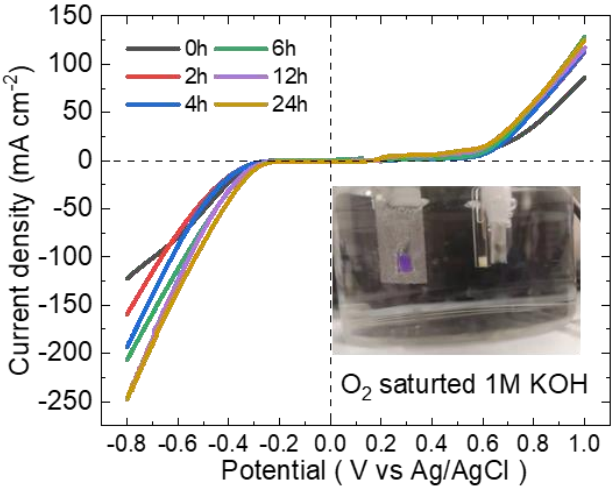

Figure 5.7. Combined ORR-OER LSV curves (measured in O_2 saturated 1M KOH electrolyte) of EZIF-67 samples, obtained after subjecting to different durations of charge-discharge cycling tests.

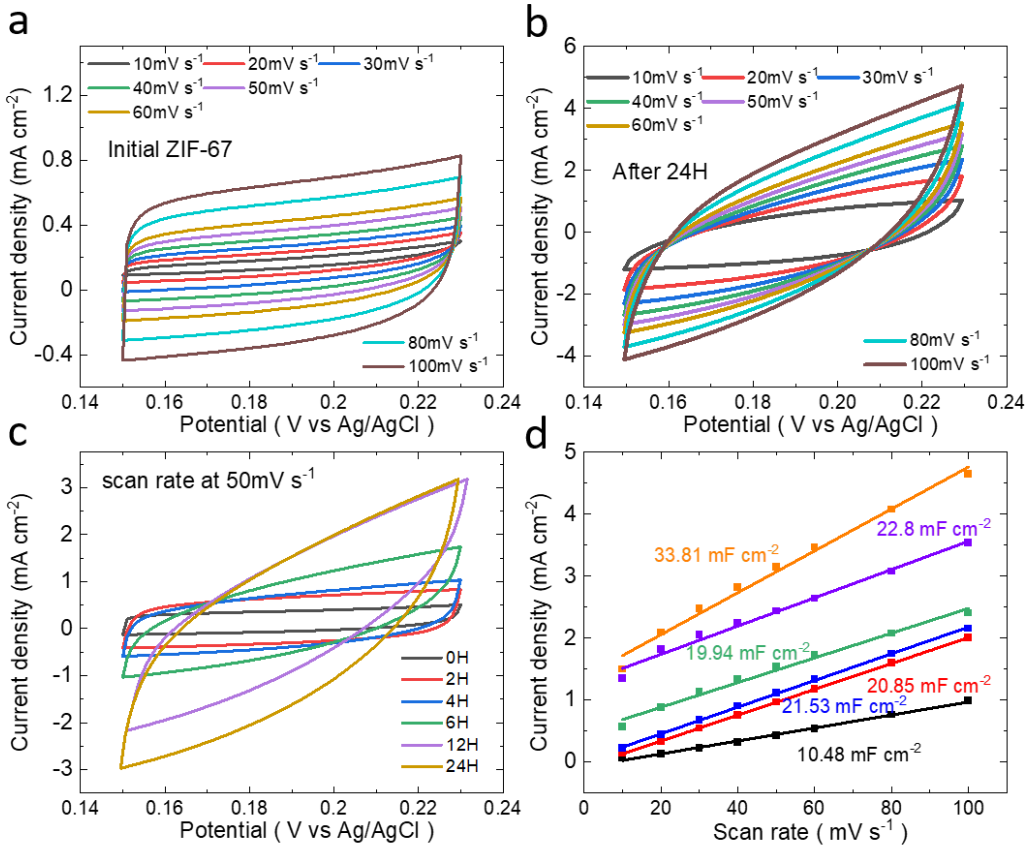

Figure 5.8. (a-b) CV curves of ZIF-67 before and after 24 h cycling test at different scan rates of 10, 20, 30, 40, 50 and 60 mV s^{-1}. **(c)** CV curves of EZIF-67 with different activation duration. **(d)** Corresponding double-layer capacitance (Cdl) calculation, obtained from the slope of linear plot of maximum current density against a scan rate.

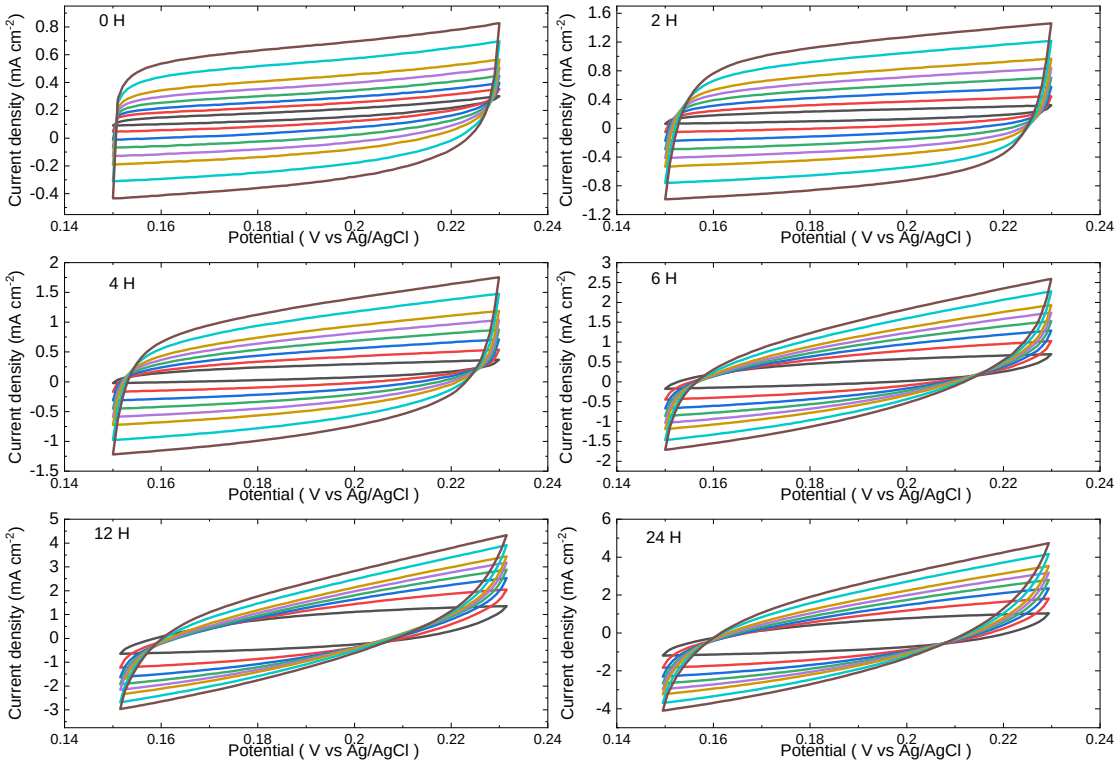

Figure 5.9. (a-b) CV curves of EZIF-67 after 0 to 24 h cycling test at different scan rates of 10, 20, 30, 40, 50 and 60 mV s^{-1}. All the samples are coated on the hydrophobic carbon paper and with same sample loading of 1.0 mg cm^{-2}.

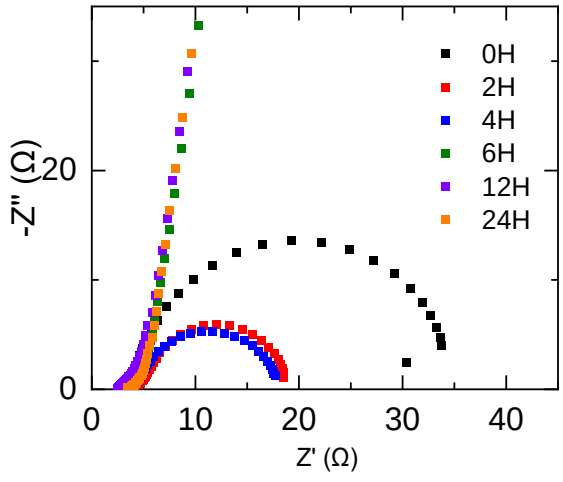

Figure 5.10. Electrochemical impedance spectroscopy (EIS) of EZIF-67 at different durations.

SEM and TEM images represent expanded sheets-like structure in EZIF-67 or ZIF-67 after electrochemical activation process compared to well-defined polyhedron particles (Figure 5.11, 5.12 and 5.13a-c). SEM images reveal that during the cycling test, the ZIF-67 structure collapsed gradually and after 24 hours most part of the structure is transformed to large cobalt oxide cloud like region. Energy-dispersive X-ray spectroscopy mapping images further show the transformation of ZIF-67 to cobalt oxide/hydroxide species. It is worth noting that the main phases of the dispersed nanoparticles are $Co(OH)_2$ and Co_3O_4 (Figure 5.13d-f). The color of the air electrode is also changed gradually from purple to brown upon electrochemical activation progressed, which indicates the phase transformation and about 24 hours later the sample deposited on the carbon paper is completely changed to brown (Figure 5.14). The XRD patterns suggest an amorphous state of the fully activated material (Figure 5.15). The above phenomenon suggests a transformation occurred during the galvanodynamic scans.

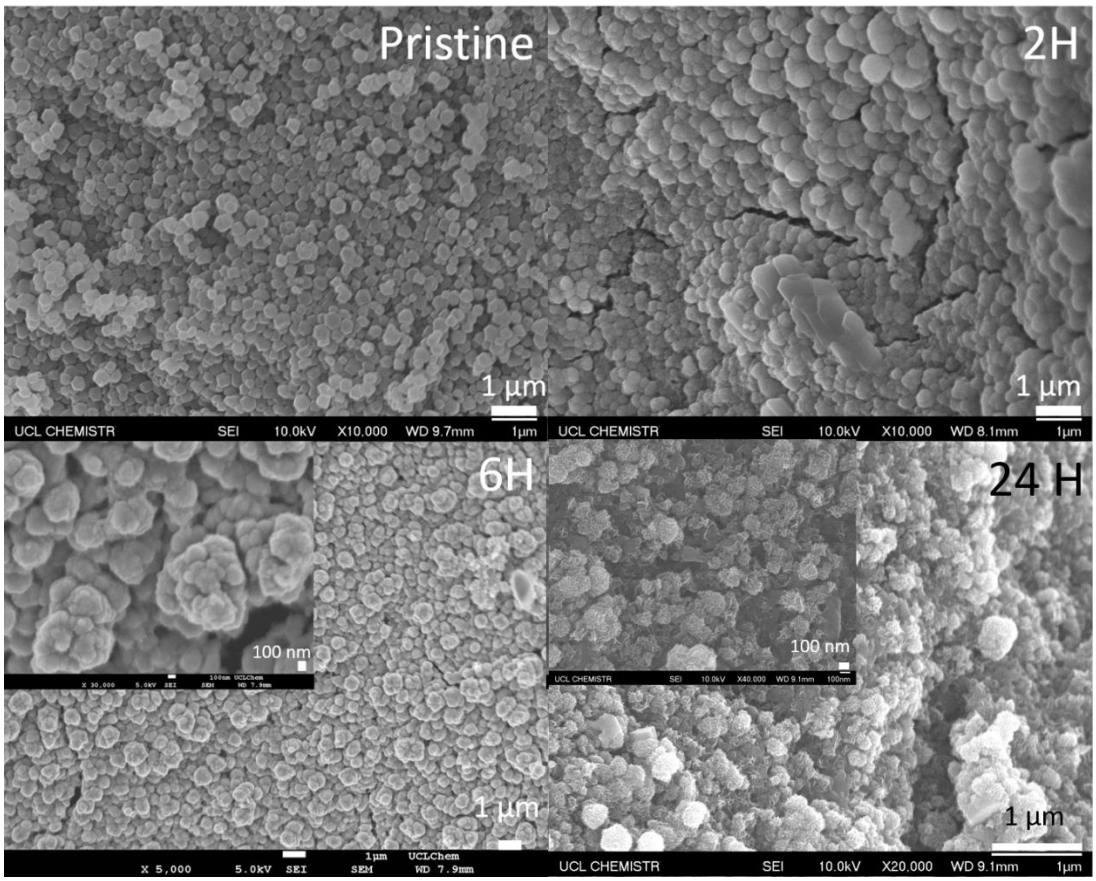

Figure 5.11. SEM images of ZIF-67 after cycling test at different time scale.

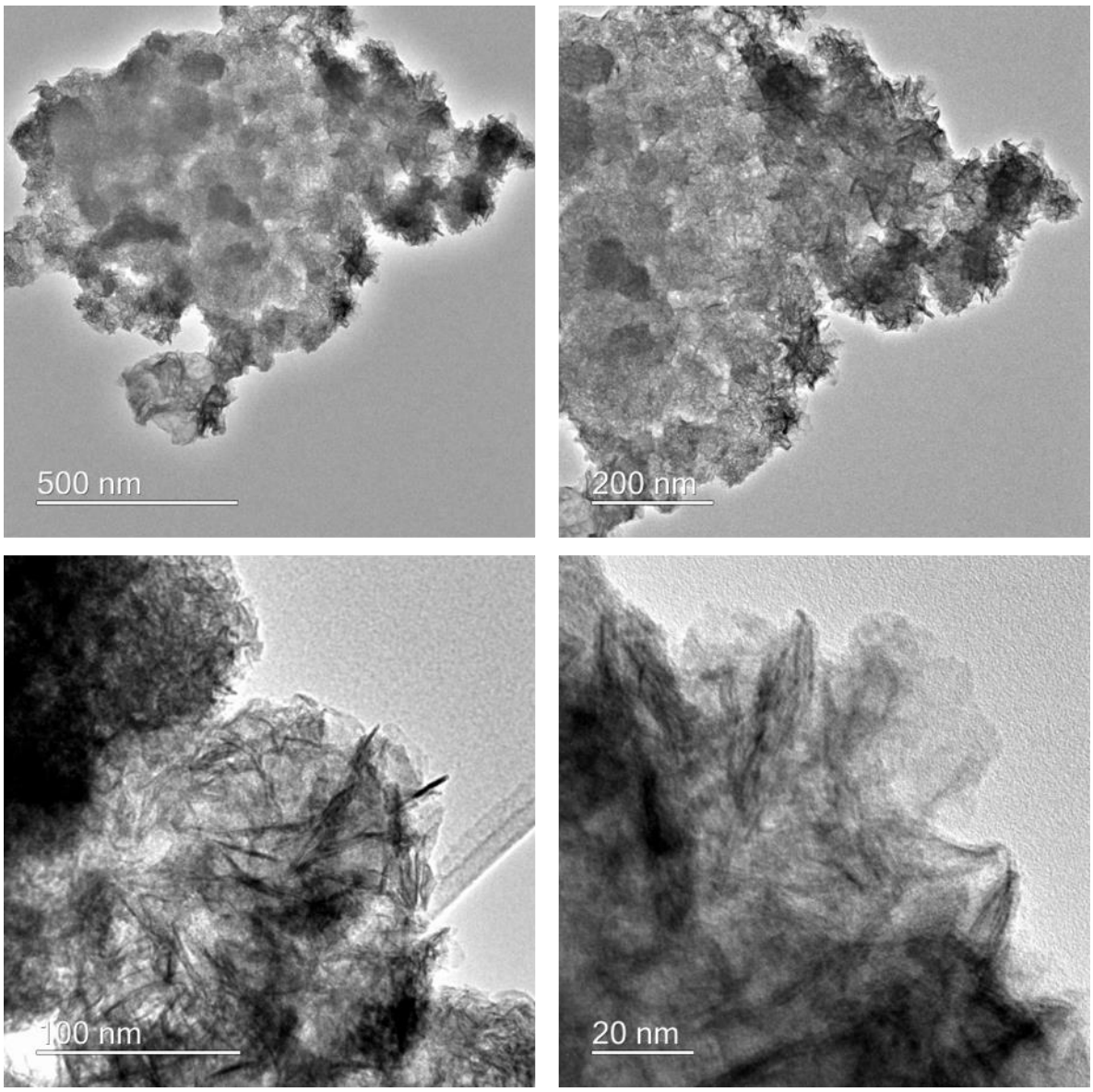

Figure 5.12. TEM images of ZIF-67 after cycling test for 24 h.

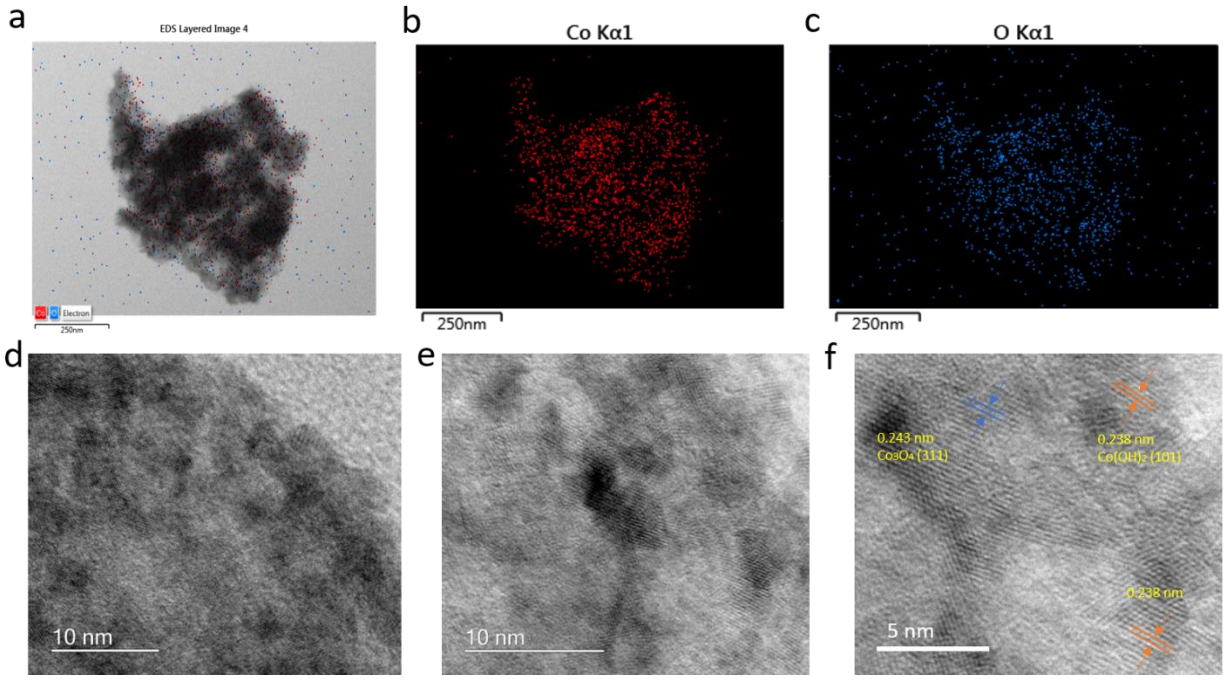

Figure 5.13. (a-c) TEM and corresponding elemental mapping images. **(d-f)** HR-TEM images of the Co_3O_4 and $Co(OH)_2$ phases of ZIF-67 after cycling test for 24 h.

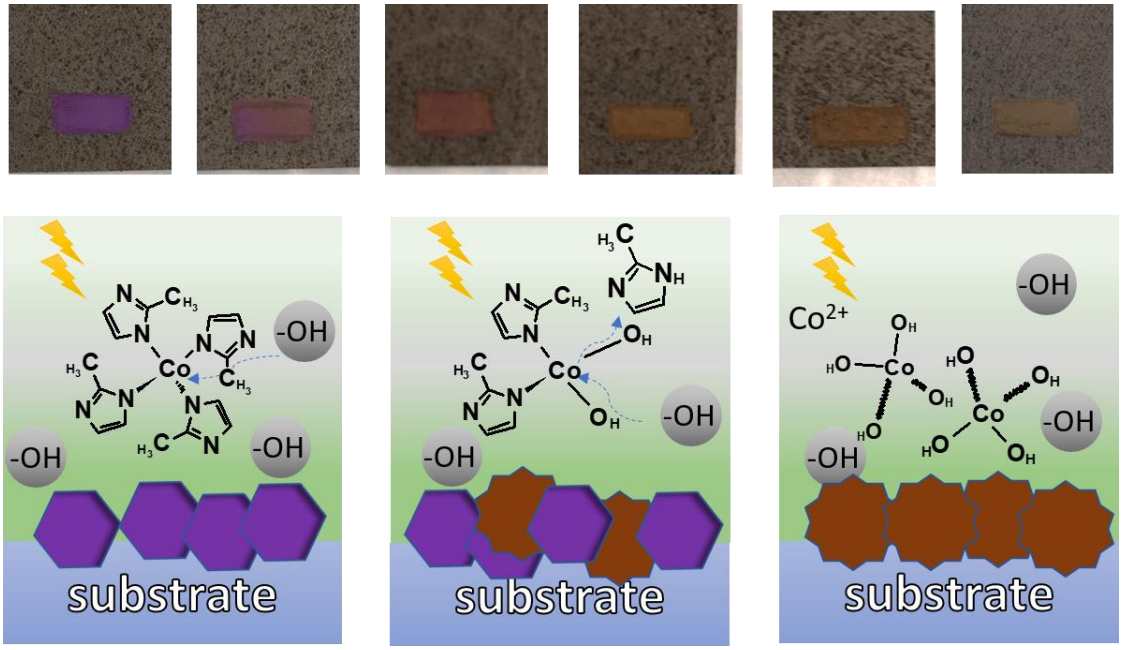

Figure 5.14. Photographs of working electrode gathered after 0, 2, 4, 6, 12, 24 hours of electrochemical activation, and schematic images of ZIF-67 catalyst evolution upon cycling process.

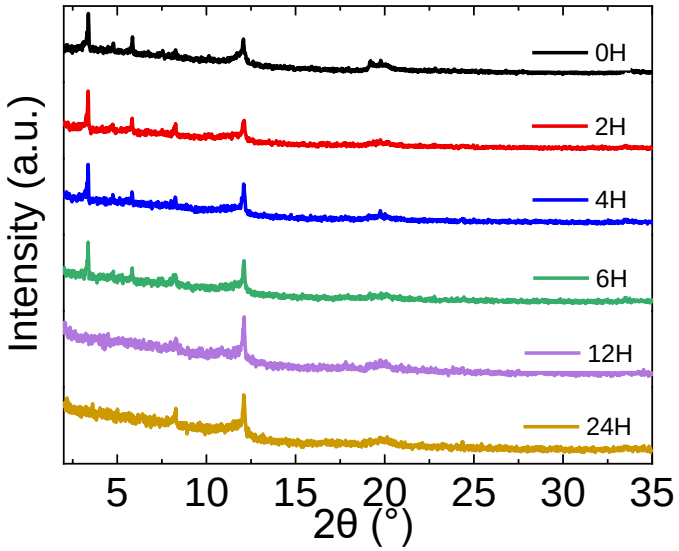

Figure 5.15. XRD patterns of ZIF-67 after cycling test at different time scale.

The presence of Co, O, N species on the surface of the electrode during the activation process is also examined by the XPS (Figure 5.16). Compared with the pristine ZIF-67, the EZIF-67 with increased activation time exhibits the Co $2p_{3/2}$, O 1s and N1s peaks shift to lower binding energy. XPS spectra closely reveal the new structure development under the electrochemical activation process. For instance, the deconvolution of Co $2p_{1/2}$ and Co $2p_{2/3}$ peaks confirmed the existence of Co^{2+} and Co^{3+}, as cycling number increased. This is clearly seen from the spectra that the dominant peak at 780.0 eV (corresponded to Co^{3+}) is decreased with respect to the peak at 781.1 eV (corresponded to Co^{2+}) (Figure 5.16a). The reduced intensity of the satellite peaks at about 786 eV and 803 eV, which are attributed to the Co^{2+} oxidation state in ZIF-67, shows the increased concentration of Co^{3+} by formation of amorphous cobalt-oxide/hydroxide phase at the expense of Co-N coordination during the cycling test.[24–26] Literature indicate that Co^{3+} is an efficient active site with a lower coordination number and larger H_2O sorptive ability, which can improve the OER activity.[27] Meanwhile, $Co(OH)_2$ can serve as active sites to facilitate ORR performance. Under the charge-discharge condition, the Co ions are further oxidized, and are likely in a mixture of several different oxidation states, as indicated by the peak shifts toward higher binding energy. Also, the N1s spectra reveal the peak at 399.6 eV from the imidazolate linker, which is gradually disappeared as the cycling number increased to 24 hours. This indicates the ZIF-67 conversion to cobalt oxide/hydroxide (Figure 5.16b). As observed from Co 2p, the O 1s spectra also show the

same trend, with the peak shift from 531.8 eV to 531.0 eV for the formation oxide/hydroxide phase (Figure 5.16c). FTIR spectra also reveal the structure evolution from the cycling charge-discharge process (Figure 5.17). The vibrational modes appear at ~ 420 cm^{-1}, ~ 992 cm^{-1}, 1141 cm^{-1}, and ~ 1575 cm^{-1} corresponding to Co-N bond and the imidazolate linker (C=C-H, C=N and C-N). Meanwhile, the decreased intensity of peak at ~420 cm^{-1} and the new peak appeared at ~ 556 cm^{-1} from Co-O bond, indicates the phase transformation from ZIF-67 structure to cobalt oxide/hydroxide species. In addition, Raman spectra with (Figure 5.18) peaks ~262, 312, 424 and 686 cm^{-1} are assigned to ZIF-67.[28,29] After long period of charge-discharge cycling activation of ZIF-67 for 120 h, the peaks belongs to ZIF-67 are disappeared and new peaks appear at 471, 512, and 617 cm^{-1}, in good agreement with the vibrational modes of Co_3O_4 and $Co(OH)_2$.[28,30]

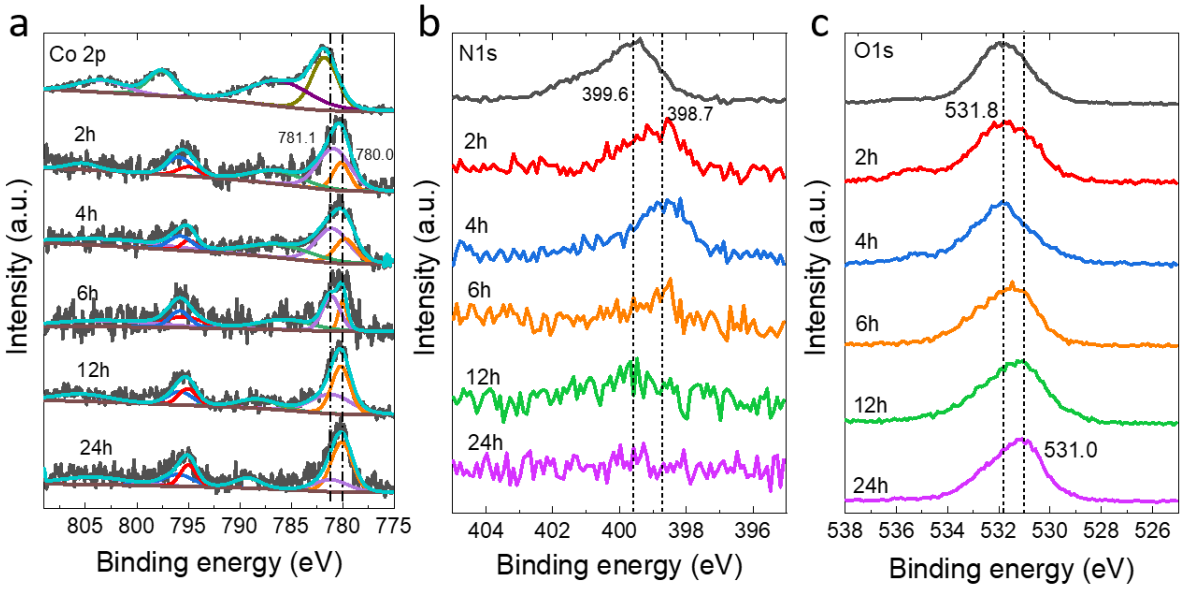

Figure 5.16. XPS spectra of Co 2p, N 1s and O 1s of ZIF-67 after cycling test at different time scale.

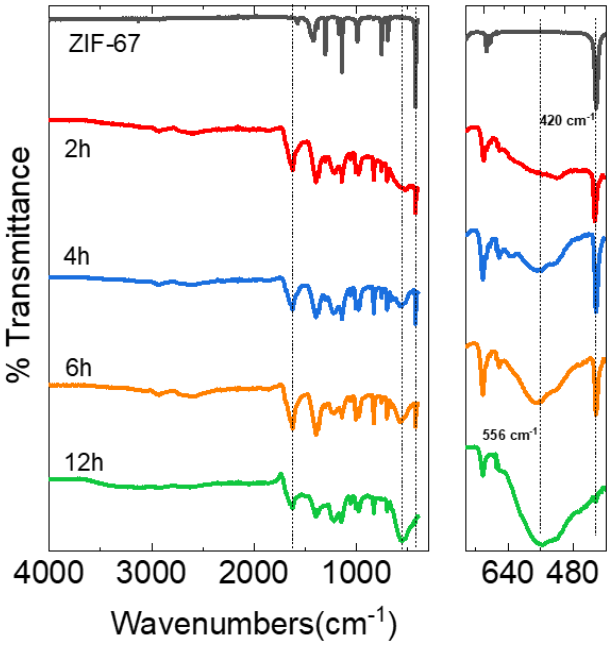

Figure 5.17. FTIR spectra of ZIF-67 after cycling test at different time scale.

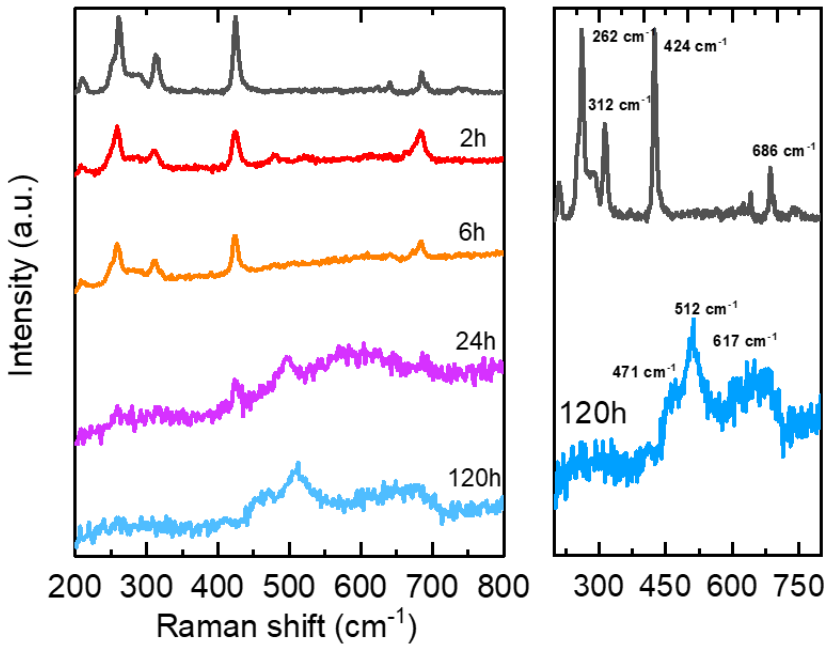

Figure 5.18. Raman spectra of ZIF-67 after cycling test at different time scale.

5.4 Conclusion

In summary, as-synthesized ZIF-67 is being used to serve as a high performance electrocatalyst for zinc-air battery by an in-situ electrochemically-driven activation method. After approximately 24 h charge-discharge cycling process in high concentration alkaline electrolyte, the power density experiences a nearly 4.5 times enlargement; increased from 39.3 mW cm^{-2} to 180 mW cm^{-2}. The voltage gap and round-up efficiency of 200 nm ZIF-67 is significantly improved from 1.26 V (39.7%) to 0.89V (56.6%) and deliver a long-lasting stability for over 1100 h. This method with no further treatment like chemical modification or carbonization at high temperature is highly desirable tool for designing bifunctional catalysts. The amorphous cobalt hydroxide/oxide species generated from the pristine ZIF-67 are the main active species. The present study provides a straightforward and energy-efficient strategy for designing bifunctional electrocatalysts. Focusing on economically viable strategies that do not rely on expensive raw materials or processing, ZIF-67 is an exceptional candidate for energy storage and conversion applications.

5.5 References

[1] S. S. Shinde, C. H. Lee, J.-Y. Jung, N. K. Wagh, S.-H. Kim, D.-H. Kim, C. Lin, S. U. Lee, J.-H. Lee, *Energy Environ. Sci.* **2019**, *12*, 727.

[2] S. Clark, A. R. Mainar, E. Iruin, L. C. Colmenares, J. A. Blázquez, J. R. Tolchard, Z. Jusys, B. Horstmann, *Adv. Energy Mater.* **2020**, *10*, 1903470.

[3] Z.-F. Huang, J. Song, Y. Du, S. Xi, S. Dou, J. M. V. Nsanzimana, C. Wang, Z. J. Xu, X. Wang, *Nat. Energy* **2019**, *4*, 329.

[4] Y.-P. Deng, Y. Jiang, R. Liang, S.-J. Zhang, D. Luo, Y. Hu, X. Wang, J.-T. Li, A. Yu, Z. Chen, *Nat. Commun.* **2020**, *11*, 1952.

[5] C. Stumm, M. Bertram, M. Kastenmeier, F. D. Speck, Z. Sun, J. Rodríguez-Fernández, J. V Lauritsen, K. J. J. Mayrhofer, S. Cherevko, O. Brummel, J. Libuda, *Adv. Funct. Mater.* **2021**, 2009923.

[6] X.-F. Lu, P.-Q. Liao, J.-W. Wang, J.-X. Wu, X.-W. Chen, C.-T. He, J.-P. Zhang, G.-R. Li, X.-M. Chen, *J. Am. Chem. Soc.* **2016**, *138*, 8336.

[7] J. Li, Z. Meng, D. J. L. Brett, P. R. Shearing, N. T. Skipper, I. P. Parkin, S. Gadipelli, *ACS Appl. Mater. Interfaces* **2020**, acsami.0c10151.

[8] J. Zhou, L. Zhang, Y.-C. Huang, C.-L. Dong, H.-J. Lin, C.-T. Chen, L. H. Tjeng, Z. Hu, *Nat. Commun.* **2020**, *11*, 1984.

[9] C.-Y. Su, H. Cheng, W. Li, Z.-Q. Liu, N. Li, Z. Hou, F.-Q. Bai, H.-X. Zhang, T.-Y. Ma, *Adv. Energy Mater.* **2017**, *7*, 1602420.

[10] L. Yang, S. Feng, G. Xu, B. Wei, L. Zhang, *ACS Sustain. Chem. Eng.* **2019**, *7*, 5462.

[11] J.-C. Li, X.-T. Wu, L.-J. Chen, N. Li, Z.-Q. Liu, *Energy* **2018**, *156*, 95.

[12] H. Guo, Q. Feng, J. Zhu, J. Xu, Q. Li, S. Liu, K. Xu, C. Zhang, T. Liu, *J. Mater. Chem. A* **2019**, *7*, 3664.

[13] L. Ma, R. Wang, Y.-H. Li, X.-F. Liu, Q.-Q. Zhang, X.-Y. Dong, S.-Q. Zang, *J. Mater. Chem. A* **2018**, *6*, 24071.

[14] G. Chen, J. Zhang, F. Wang, L. Wang, Z. Liao, E. Zschech, K. Müllen, X. Feng, *Chem. – A Eur. J.* **2018**, *24*, 18413.

[15] L. Wei, H. E. Karahan, S. Zhai, H. Liu, X. Chen, Z. Zhou, Y. Lei, Z. Liu, Y. Chen, *Adv. Mater.* **2017**, *29*, 1701410.

[16] Y. Guo, P. Yuan, J. Zhang, Y. Hu, I. S. Amiinu, X. Wang, J. Zhou, H. Xia, Z. Song, Q. Xu, S. Mu, *ACS Nano* **2018**, *12*, 1894.

[17] C. Deng, K. H. Wu, J. Scott, S. Zhu, X. Zheng, R. Amal, D. W. Wang, *ACS Appl. Mater. Interfaces* **2019**, *11*, 9925.

[18] D. Liu, B. Wang, H. Li, S. Huang, M. Liu, J. Wang, Q. Wang, J. Zhang, Y. Zhao, *Nano Energy* **2019**, *58*, 277.

[19] J. Gao, J. Wang, L. Zhou, X. Cai, D. Zhan, M. Hou, L. Lai, *ACS Appl. Mater. Interfaces* **2019**, *11*, 10364.

[20] H. Mei, M. Yang, Y. Shen, F. He, Z. Zhou, X. Chen, Y. Yang, S. Liu, Y. Zhang, *Carbon.* **2019**, *144*, 312.

[21] Y. Lian, W. Yang, C. Zhang, H. Sun, Z. Deng, W. Xu, L. Song, Z. Ouyang, Z. Wang, J. Guo, Y. Peng, *Angew. Chem. Int. Ed.* **2020**, *59*, 286.

[22] D. Ren, J. Ying, M. Xiao, Y. Deng, J. Ou, J. Zhu, G. Liu, Y. Pei, S. Li, A. M. Jauhar, H. Jin, S. Wang, D. Su, A. Yu, Z. Chen, *Adv. Funct. Mater.* **2020**, *30*, 1908167.

[23] D. Chen, X. Chen, Z. Cui, G. Li, B. Han, Q. Zhang, J. Sui, H. Dong, J. Yu, L. Yu, L. Dong, *Chem. Eng. J.* **2020**, *399*, 125718.

[24] W. Liu, K. Wang, C. Wang, W. Liu, H. Pan, Y. Xiang, D. Qi, J. Jiang, *J. Mater. Chem. A* **2018**, *6*, 22851.

[25] B. Y. Xia, Y. Yan, N. Li, H. Bin Wu, X. W. Lou, X. Wang, *Nat. Energy* **2016**, *1*, 15006.

[26] J. Wei, J. Dong, X. Meng, J. Kong, X. Wang, J. Zhang, H. Zhang, G. Liu, P. An, L. Shi, G. Zhao, J. Ye, *Angew. Chem. Int. Ed.* **2016**, *55*, 14310.

[27] M. Bajdich, M. García-Mota, A. Vojvodic, J. K. Nørskov, A. T. Bell, *J. Am. Chem. Soc.* **2013**, *135*, 13521.

[28] W. Zheng, M. Liu, L. Y. S. Lee, *ACS Catal.* **2020**, *10*, 81.

[29] P. M. Usov, C. Mcdonnell-worth, F. Zhou, D. R. Macfarlane, D. M. D. Alessandro, *Electrochim. Acta* **2015**, *153*, 433.

[30] J. Guo, S. Gadipelli, Y. Yang, Z. Li, Y. Lu, D. J. L. Brett, Z. Guo, *J. Mater. Chem. A* **2019**, *7*, 3544.

Chapter 6. Conclusions and perspectives

The PhD project is focused on designing metal-organic framework-based efficient bifunctional catalysts for the energy storage applications. In the thesis, facile processing strategies have been discovered to deliver inexpensive, durable and high-performance catalysts that have potential to replace current noble metal-based catalysts such as Pt/CB for ORR and Ir/C for OER in the alkaline environment.

In the first work, a new, easy way to replicate synthesis route to highly active electrocatalyst from MOF starting materials without the need for routinely performed carbonisation or other post-synthesis modification is developed. Specifically, ZIF-8 analogues are readily synthesized. The prototype ZIF-8, formed by imidazolate linkers and single-metal-atom (Zn or Co)–N_4 tetrahedra, is reminiscent to the proposed active M-N_4 (M = Co, Fe, etc.) sites in carbonaceous electrocatalysts. Therefore, the first work discovered the interesting electrocatalytic activity of as-synthesized ZIF-67(Co) directly without carbonisation and established OER activity trend with the substitution of cobalt metal centres for zinc in bimetallic ZIFs(Co/Zn). Here worth noting that no further post-synthesis chemical modification such as oxidation or carbonization at high temperature is performed. Co–N, rather than Zn–N, coordination is responsible for the oxygen catalysis reactions, which is identified by screening the ZIF samples from ZIF-8 to ZIF-67 with a progressive cobalt substitution for zinc-metal centres. Such activities are further improved by the addition of conducting carbon black. ZIF-67/CB samples show significantly enhanced OER performance.

In the second work, motivated by the enhanced OER activity by adding conductive carbon black to the ZIF-67, the bifunctional activity of ZIF-67 for OER and ORR is demonstrated by physically combining the ZIF-67 with platinum-carbon black (ZIF-67@Pt/CB). The best bifunctional activity,

with a small overpotential of ≈0.87 V, is observed for the sample with 1:1 mass ratio of ZIF-67 and Pt/CB. Interestingly, ZIF-67@Pt/CB(50wt%) enhanced the ORR durability of Pt/CB, where the sample showed activity retention of ≈85% over 20 h operation compared to the ≈52% for Pt/CB. Such activities are attributed to the synergistic coupling between Pt nanoparticles and Co-metal centres in ZIF-67. Remarkably, a rechargeable Zn-air battery based on ZIF-67@Pt/CB(50wt%) delivered excellent stability and high power density. This work presents a straightforward and energy-efficient strategy for designing bifunctional electrocatalysts. Focusing on economically viable strategies that do not rely on expensive raw materials and an organic linker, ZIF-67 is an exceptional candidate for energy storage and conversion applications.

The third work, a high performing zinc-air battery is developed by discovering highly active electrocatalyst from in-situ electrochemically activated MOF, without carbonisation or other post-synthesis modification externally. The electrochemically transformed ZIF-67 to active cobalt-(oxy)hydroxide nanophase is responsible for delivering a power density of 180 mW cm^{-2} in zinc-air cells. This value is nearly 4.5 times higher compared to the power delivered from a pristine ZIF-67. The voltage gap and round-up efficiency of 200 nm ZIF-67 based battery cell is significantly improved from 1.26 V (39.7%) to 0.89V (56.6%) and offered a long-lasting stability for over 1100 h. Therefore, given the urgent and rapidly growing global interest in energy conversion and storage materials, and the key material and conceptual advances presented, this thesis work will guide for further advancements and enable identification of electrocatalysts from as-produced MOFs alone, without resorting to energy-intensive post-processing methods.

To discover what the mechanisms behind the evolution of the catalysts, additional experiments are expected to check the final active phase of the catalyst. The in-situ XRD test would be preferred for the phase identification. And if possible, XANES spectra (X-ray absorption near edge structure)

can also provide the information of phase transformation during the cycling test. High resolution micro-CT is favoured to probe materials at various stages in their life cycle and perfect to facilitate an understanding of the effect of microscopic structural changes on material degradation. From the literatures, we may expect the evolution of the ZIF structure from Co-N transformed to Co-O and Co-OH which could be Co_3O_4, CoOOH, $Co(OH)_2$ or even zinc cobalt oxide complex. The future research will focus on the in-situ measurements and with some simulation collaborations.

In summary, it is interesting to note in this PhD project, the research is firstly started by investigating the OER catalytic performance of zinc/cobalt based ZIFs. Then, cobalt based ZIF and platinum carbon black composites (ZIF-67@Pt/CB) are designed to satisfy the need of bifunctionality (ORR/OER) that can work in zinc-air batteries. Considering the high cost of the commercial platinum carbon used in the system, the facile activation method of ZIF-67 structure is developed in-situ electrochemical cell, without combining with Pt/CB, which offers marvellous performance and high energy density with excellent safety over Li-ion batteries. Due to the intense and growing global interest in this research area, the works in this PhD project enables identification of electrocatalysts from as-produced MOFs alone, without resorting to energy-intensive post-processing methods.

Publication list

1. **Li, J.**; Meng, Z.; Brett, D. J. L.; Shearing, P. R.; Skipper, N. T.; Parkin, I. P.; Gadipelli, S. High-Performance Zinc–Air Batteries with Scalable Metal–Organic Frameworks and Platinum Carbon Black Bifunctional Catalysts. ***ACS Appl. Mater. Interfaces.*** 2020.

2. **Li, J.**; Gadipelli, S. Synthesis and Optimization of Zeolitic Imidazolate Frameworks for Oxygen Evolution Reaction. ***Chem. – A Eur. J.*** 2020.

3. Gadipelli, S.; Li, Z.; Lu, Y.; **Li, J.**; Guo, J.; Skipper, N. T.; Shearing, P. R.; Brett, D. J. L., Size-related electrochemical activity-performance relationships in active carbon nanostructures: a MOF-derived carbons case study, ***Adv. Sci.***, 2019, 6, 1901517

4. Li, Z.; Gadipelli, S.; Yang, Y.; He, G.; Guo, J.; **Li, J.**; Lu, Y.; Howard, C. A.; Brett, D. J. L.; Parkin, I. P.; Li, F.; Guo, Z., Exceptional supercapacitor performance from optimized oxidation of graphene-oxide, ***Energy Storage Mater.***, 2019, 17, 12-21.

5. Meng, Z.; **Li, J.**; Huo, F.; Huang, Y.; Xiang, Z. Fungi Residue Derived Carbon as Highly Efficient Hydrogen Peroxide Electrocatalyst. **Chem. Eng. Sci.** 2017, 174, 222–228

6. Li, Z.; **Li, J.**; Guo, Z.; Campos, L. C. Investigation of Metaldehyde Removal by Powdered Activated Carbon from Different Water Samples. **Environ. Sci. Water Res. Technol**. 2020, 6, 1432–1444